8-2020

Free Charge Carrier Properties in Two-Dimensional Materials and Monoclinic Oxides Studied by Optical Hall Effect

Sean Knight
University of Nebraska - Lincoln, knightsr1029@gmail.com

FREE CHARGE CARRIER PROPERTIES IN TWO-DIMENSIONAL MATERIALS AND MONOCLINIC OXIDES STUDIED BY OPTICAL HALL EFFECT

by

Sean Knight

A DISSERTATION

Presented to the Faculty of

The Graduate College at the University of Nebraska

In Partial Fulfillment of Requirements

For the Degree of Doctor of Philosophy

Major: Electrical Engineering

Under the Supervision of Professor Mathias Schubert

Lincoln, Nebraska

August, 2020

FREE CHARGE CARRIER PROPERTIES IN TWO-DIMENSIONAL MATERIALS AND MONOCLINIC OXIDES STUDIED BY OPTICAL HALL EFFECT

Sean Knight, Ph.D.

University of Nebraska, 2020

Advisor: Mathias Schubert

In this dissertation, optical Hall effect (OHE) measurements are used to determine the free charge carrier properties of important two-dimensional materials and monoclinic oxides. Two-dimensional material systems have proven useful in high-frequency electronic devices due to their unique properties, such as high mobility, which arise from their two-dimensional nature. Monoclinic oxides exhibit many desirable characteristics, for example low-crystal symmetry which could lead to anisotropic carrier properties. Here, single-crystal monoclinic gallium oxide, an AlInN/GaN-based high-electron-mobility transistor (HEMT) structure, and epitaxial graphene are studied as examples.

To characterize these material systems, the OHE measurement technique is employed. The OHE is a physical phenomenon where a change in a conducting sample's optical response is observed when immersed in an external magnetic field (i.e. the optical analogue of the electrical Hall effect). To quantify this change in a sample's optical response, generalized ellipsometry was employed for our OHE measurements. All necessary data is collected and analyzed with appropriate optical models, providing the free charge carrier properties of interest. To obtain the free charge carrier properties of the material systems studied here, OHE measurements were performed in two different spectral ranges: in

the mid-infrared range for monoclinic gallium oxide, and in the terahertz (THz) range for the HEMT structure and epitaxial graphene. Measurements in the THz spectral range are made possible by exploiting Fabry-Pérot interferences inside THz-transparent substrates, as well as within an additional cavity external to the samples. Results for carrier concentration and mobility determined by OHE are in excellent agreement with previous electrical Hall effect characterizations. Results for effective mass are also in agreement with previous density functional theory calculations. Characterizations of thorium dioxide and uranium dioxide, as well as cupric oxide are also included. Since no free charge carriers were detected in these samples, these reports serve as introductions to infrared ellipsometry, THz ellipsometry, and the Fabry-Pérot enhancement techniques used here.

ACKNOWLEDGMENTS

I would like to first thank my advisors Prof. Mathias Schubert and Prof. Tino Hofmann for their guidance and support throughout my experience as a graduate student. I am very grateful to have been given the opportunity to be part of such an outstanding research group. Working with them and their original optical Hall effect instrumentation was a unique and rewarding experience.

I would also like to thank Prof. Eva Schubert, Prof. Christian Binek, and Prof. Xia Hong for serving as my supervisory committee members and for helping me along my academic career.

I would like to extend an additional thank you to Prof. Tino Hofmann for recruiting and introducing me into the world of ellipsometry. I greatly appreciate the many hours of training and advice given during my first years as a graduate student.

I would like to thank Prof. Vanya Darakchieva from the University of Linköping, Sweden, for providing the laboratory collaboration necessary for the experiments involving epitaxial graphene, as well as her many contributions to other studies included in this dissertation.

I would also like to extend a special thank you to:

- John A. Woollam, James N. Hilfiker, Craig M. Herzinger, and all others at the J. A. Woollam Company for the support, collaboration, and advice provided to aid the research conducted at the University of Nebraska-Lincoln
- Dr. Rafał Korlacki for performing the density functional theory calculations included in this dissertation, managing laboratory equipment, and many helpful discussions to help me understand the physics behind the materials investigated here.
- Charles Rice for helping recruit and introduce me to the field of ellipsometry
- All of my other colleagues at the University of Nebraska-Lincoln: Dr. Alyssa Mock, Ufuk Kilic, Megan Stokey, Chad Briley, Matthew Hilfiker, Alex Ruder, Shawn Wimer, Ryan Bates, Dr. Stefan Schöche, Dr. Darin

Peev, Albert Nguyen, Dr. Derek Sekora, Dr. Alex Boosalis, Dr. Keith Rodenhausen, Jr., Dr. Dan Liang, and Dr. Tadas Kasputis

- All of my other colleagues at the University of Linköping, Sweden: Dr. Philipp Kühne, Dr. Nerijus Armakavicius, Dr. Chamseddine Bouhafs, Dr. Vallery Stanishev, and Dr. Steffen Richter.

Finally, I would like to thank my parents, Douglas and Stacie Knight, and brother, Landon Knight, for the tremendous amount of support and love they have given me. This would not be possible without their help.

GRANT INFORMATION

This work was primarily supported by the National Science Foundation (NSF) through Materials Research Science and Engineering Center (MRSEC) Grant No. DMR-1420645, J. A. Woollam Inc., and the University of Nebraska-Lincoln (Engineering Recruitment Scholarship). Additional funding for the studies included in this dissertation are listed at the end of each chapter.

Table of Contents

List of Tables

List of Figures

Chapter 1

Introduction

In order to meet the growing demand for advanced electronic devices, more sophisticated material systems must be explored and implemented. Some two-dimensional material systems and monoclinic oxides are promising candidates to further improve device performance. For example, high-electron-mobility transistor (HEMT) structures, commonly used in radio communication circuitry, can be enhanced by tuning layer compositions to improve its two-dimensional electron gas (2DEG) mobility.[1] Graphene has a wide range of applications in high-frequency electronics due to unique properties, such as high 2DEG mobility, which are a result of its two-dimensional nature.[2] The monoclinic phase of gallium oxide (β-Ga_2O_3) is useful in power electronics due to its large break down voltage, and also as a transparent electrode material.[3] In order to fabricate more advanced devices, the free charge carrier properties of these materials must be fully characterized. Typically, carrier concentration, mobility, and carrier type are obtained using electrical Hall effect measurements. Although it is a widely used technique, the electrical Hall effect has a disadvantage of requiring electrical contacts to be fabricated onto the sample. To extract the free charge carrier properties, ideal Ohmic behavior of the contacts is assumed, which could yield inaccurate results depending on the sample's surface po-

tential. Additionally, the electrical Hall effect does not provide access to any buried conducting layers. To address these issues, we employ our measurement technique - the optical Hall effect (OHE). The OHE is a physical phenomenon in which the optical response of a conducting sample is altered due to the Lorentz force on free charge carriers from an externally applied magnetic field.[4,5] The OHE is the optical analogue of the electrical Hall effect, and can be described by the classical Drude model with an additional magnetooptic contribution. OHE measurements provide access to the effective mass parameter, as well as carrier concentration, mobility, and carrier type. A major advantage of the OHE technique is its non-contact, non-invasive nature, and ability to detect buried conducting layers. In this dissertation, OHE measurements are used to obtain the free charge carrier properties of single-crystal β-Ga_2O_3, a 2DEG within an AlInN/GaN-based HEMT structure, and epitaxial graphene.

To quantify the optical response of these materials, the measurement method employed here is spectroscopic ellipsometry. Spectroscopic ellipsometry measures the change in polarization of light after reflection off of or transmission through a sample.[6,7] Shown in Fig. 1.1 is the geometry and nomenclature of the reflection-type ellipsometry experiments reported in this dissertation. In standard ellipsometry, the change in polarization ρ can be expressed as

$$\rho = \frac{r_\mathrm{p}}{r_\mathrm{s}} = \frac{E_\mathrm{p,out} E_\mathrm{s,in}}{E_\mathrm{p,in} E_\mathrm{s,out}} = \tan(\Psi) e^{i\Delta}, \tag{1.1}$$

where r_p and r_s are the complex-valued Fresnel reflection coefficients for *p*-polarized and *s*-polarized light, respectively. For every measured frequency, the quantities Ψ and Δ are recorded. Ψ represents the polarization rotation of the light, and Δ represents the relative phase shift between *p* and *s* light com-

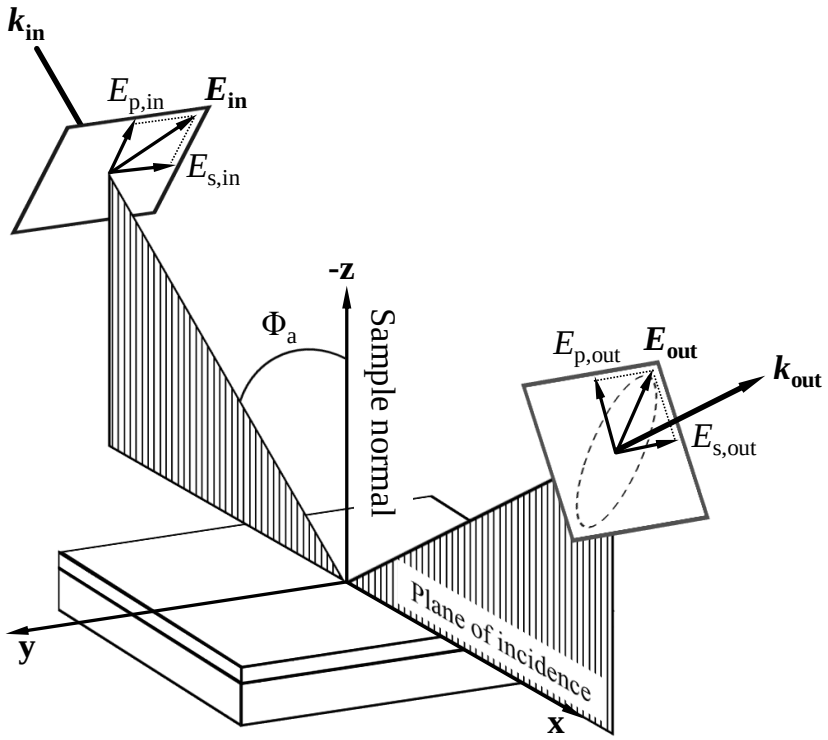

Figure 1.1: An illustration detailing the setup of a reflection-type spectroscopic ellipsometry experiment. Here, $\boldsymbol{k}_{in}$ and $\boldsymbol{k}_{out}$ are the incoming and outgoing electromagnetic plane wavevectors, respectively, with their electric field vectors designated as $\boldsymbol{E}_{in}$ and $\boldsymbol{E}_{out}$. The scalar components of $\boldsymbol{E}_{in}$ and $\boldsymbol{E}_{out}$ are $E_{p,in}$, $E_{p,out}$, $E_{s,in}$, and $E_{s,out}$ where subscripts 'p' and 's' indicate *p*-polarized (parallel to the plane of incidence) and *s*-polarized (perpendicular to the plane of incidence) light. Φ_a is the angle of incidence, and the Cartesian coordinate axes are labeled **x**, **y**, and **-z**.

ponents. Standard ellipsometry is sufficient to measure the optical response of isotropic samples or samples that exhibit no anisotropy within the sample surface plane. However, when the material system under investigation causes mode conversion (i.e. *p*-to-*s* or *s*-to-*p* light conversion) standard ellipsometry is

no longer adequate, and generalized ellipsometry must be employed. In a generalized ellipsometry measurement, many different polarization states of light are directed at the sample, and their change in polarization is determined. In this dissertation, generalized ellipsometric data is experimentally recorded using the Mueller matrix formalism. The Mueller matrix is the 4×4 matrix which relates the input and output light Stokes vectors.[6,7] Obtaining the complete Mueller matrix allows one to fully characterize the optical response of any material system. Therefore, generalized ellipsometry is used to obtain Mueller matrix data in order to measure OHE signatures in the two-dimensional materials and monoclinic oxides investigated here. These Mueller matrix measurements are referred to as 'OHE measurements' throughout the dissertation. When the resulting OHE data is analyzed with an appropriate optical model, the free charge carrier properties can then be determined.

Chapter 2 is an article titled "Infrared-active phonon modes in single-crystal thorium dioxide and uranium dioxide" which was previously published in the *Journal of Applied Physics*.[8] The infrared-active phonon modes in single-crystal samples of thorium dioxide (ThO_2) and uranium dioxide (UO_2) are characterized by standard ellipsometry in the far-infrared (FIR) and mid-infrared (MIR) spectral ranges. The ThO_2 sample was investigated at room temperature and elevated temperatures, whereas UO_2 was only studied at room temperature. The experimental results from ellipsometry are compared with density functional theory (DFT) predictions. Since no free charge carriers were detected in the ThO_2 and UO_2 samples, OHE measurements were not performed. Therefore, this chapter serves as an introduction to infrared ellipsometry (Reproduced from [S. Knight *et al.*, J. Appl. Phys. **127**, 125103 (2020).], with the permission of AIP Publishing).

Chapter 3 is an article titled "Electron effective mass in Sn-doped monoclinic single crystal β-gallium oxide determined by mid-infrared optical Hall effect" which was previously published in *Applied Physics Letters*.[9] A combined analysis of MIR-OHE data from (010) and (-201) surface cut samples were used to experimentally determine the volume carrier concentration, mobility, effective mass, and charge carrier type of Sn-doped single-crystal β-Ga_2O_3. Results for concentration and mobility are in excellent agreement with previous electrical Hall effect measurements. The results for the effective mass fall within the broad range of values predicted by various DFT calculations (Reproduced from [S. Knight *et al.*, Appl. Phys. Lett. **112**, 012103 (2018).], with the permission of AIP Publishing).

Chapter 4 is an article titled "Electromagnon excitation in cupric oxide measured by Fabry-Pérot enhanced terahertz Mueller matrix ellipsometry" which was previously published in *Scientific Reports*.[10] Using terahertz (THz) Mueller matrix ellipsometry, a sample of bulk single-crystal cupric oxide is measured a function of frequency and temperature to detect an electromagnon excitation which manifests as an optical absorption. The ability to detect this subtle excitation relies on enhancement from Fabry-Pérot interferences inside the cupric oxide substrate. Results for the excitation's resonance frequency and broadening parameters are in excellent in agreement with previous THz time domain spectroscopy studies on the same material. Since no free charge carriers were detected in the cupric oxide sample, no OHE measurements were performed. Therefore, this chapter serves an as introduction to THz ellipsometry, and signal enhancement due to Fabry-Pérot interferences inside THz-transparent substrates

Chapter 5 is an article titled "Cavity-enhanced optical Hall effect in two-dimensional free charge carrier gases detected at terahertz frequencies" which was previously published in *Optics Letters*.[11] THz-OHE measurements are used to extract the free charge carrier properties of 2DEG within an AlInN/GaN-based HEMT structure. In this chapter, the magnetic field necessary for the THz-OHE measurements is provided by a permanent magnet, in contrast to a previous THz-OHE characterization which was conducted using a high-field superconducting magnet.[12] To compensate for the reduced magnetic field of the permanent magnet, an additional enhancement effect is exploited, namely the 'cavity-enhancement' effect, which refers to additional Fabry-Pérot interferences inside a cavity external to the sample (i.e. the sample-magnet surface air gap). This enhancement effect allows the free charge carrier properties to be obtained ().

Chapter 6 is an article titled "*In-situ* terahertz optical Hall effect measurements of ambient effects on free charge carrier properties of epitaxial graphene" which was previously published in *Scientific Reports*.[13] THz-OHE measurements are performed on epitaxial graphene as a function of gas exposure to monitor changes in the free charge carrier properties *in-situ*. The measurements are performed using the same cavity enhancment configuration described in Chapter 5. Large changes in the carrier properties are observed throughout the experiment; possible doping mechanisms for which are discussed (

(http://creativecommons.org/licenses/by/4.0/)).

Chapter 7 is a manuscript titled "Tunable cavity-enhanced terahertz frequency-domain optical Hall effect" which has been submitted to *Review of Scientific Instruments*[14]. This chapter expands upon the cavity-enhancement effect described in Chapters 5 and 6. More advanced cavity-tuning techniques were used to measure THz-OHE signatures in the previously mentioned HEMT structure and epitaxial graphene sample. It is demonstrated that the external cavity (i.e. the sample-magnet air gap) spacing can be used as another measurement dimension (in addition to frequency and angle of incidence) to facilitate the extraction of the free charge carrier properties (This submitted manuscript has been reproduced with the permission of AIP Publishing).

Chapter 8 is a summary of all results and important concepts presented in this dissertation.

Chapter 2

Infrared-active phonon modes in single-crystal thorium dioxide and uranium dioxide

2.1 Abstract

The infrared-active phonon modes in single-crystal samples of thorium dioxide (ThO_2) and uranium dioxide (UO_2) were investigated using spectroscopic ellipsometry and compared with density functional theory. Both ThO_2 and UO_2 are found to have one infrared-active phonon mode pair (consisting of one transverse optic (TO) and one associated longitudinal optic (LO) mode), which are responsible for the dominant features in the ellipsometric data. At room temperature, our results for the mode pair's resonant frequencies and broadening parameters are comparable with previous reflectance spectroscopy characterizations and density functional theory predictions. For ThO_2, our ellipsometry and density function theory results both show that the LO mode broadening parameter is larger than the TO mode broadening. This signifies mode anharmonicity, which can be attributed to the intrinsic phonon-phonon interaction. In addition to the main mode pair, a broad low-amplitude impurity-like vibrational mode pair is detected within the reststrahlen band for both ThO_2 and UO_2. Elevated temperature measurements were performed for ThO_2 in order to study

the mechanisms by which the phonon parameters evolve with increased heat. The observed change in the TO resonant frequency is in excellent agreement with previous density functional calculations, which only consider volume expansion of the crystal lattice. This suggests the temperature-dependent change in the TO frequency is primarily due to volume expansion. The change in the main mode pair's broadening parameters are nearly linear within the temperature range of this study, which indicates the intrinsic anharmonic scattering (via cubic anharmonicities) as the main decay mechanism. (Reproduced from [S. Knight *et al.*, J. Appl. Phys. **127**, 125103 (2020).], with the permission of AIP Publishing)

2.2 Introduction

Due to their importance to nuclear fuel rods, thorium dioxide (ThO_2) and uranium dioxide (UO_2) have been the subject of many scientific investigations.[15,16] Heat transfer, fuel expansion, and related physical properties are of particular interest for fuel rods used in nuclear power plants,[17] where heat must be transferred from the core of the fuel rod to the outer surface. Because ThO_2 and UO_2 have low thermal conductivity, a better microscopic understanding of lattice vibrations may help with designing improved thermal conductivity properties. This is all the more important because there are conflicting reports on whether the infrared-active (IR) phonon modes significantly contribute to heat transfer.[18,17] ThO_2 may be blended with UO_2 to improve fuel rod efficiencies.[19] Therefore, accurate measurement of the IR-active phonon modes of ThO_2 and UO_2 is prerequisite for improvement of heat transport properties.

In order to fully characterize the IR-active modes, the complex-valued IR

dielectric function $\epsilon(\omega)$ must be determined from optical measurements. From the spectral behaviors of $\mathrm{Re}\{\epsilon(\omega)\}$ and $\mathrm{Im}\{\epsilon(\omega)\}$, physically meaningful parameters can be extracted, such as phonon mode frequency, amplitude, and broadening parameters.[20] So far, only IR reflectance (intensity) spectroscopy has been used to optically characterize IR-active phonon modes in ThO_2 and UO_2.[21,22,23,24] This approach relies either on Kramers-Kronig transforms to obtain both $\mathrm{Re}\{\epsilon(\omega)\}$ and $\mathrm{Im}\{\epsilon(\omega)\}$, or relies on best-match model calculation using reflectance data as model target with a predetermined parameterized model for $\epsilon(\omega)$. In contrast to reflectance spectroscopy, spectroscopic ellipsometry (SE) measures two quantities (relative amplitude and relative phase shift between *s*- and *p*-polarized light after reflection) instead just one quantity (reflectivity). This additional information allows $\mathrm{Re}\{\epsilon(\omega)\}$ and $\mathrm{Im}\{\epsilon(\omega)\}$ to be extracted independently from each other, or can facilitate more accurate best-match model calculations targeting two independent spectra of the ellipsometric data using a predetermined parameterized model.

In this work, we employed IR spectroscopic ellipsometry (IRSE) to extract the dielectric functions of ThO_2 and UO_2. Our approach allows us to accurately characterize their IR phonon modes. We compare our results with density functional theory (DFT) calculations and previous reflectance spectroscopy. The existence of an IR-active impurity-like vibrational mode pair is discussed, as well as its possible anharmonic coupling to other phonon modes. For ThO_2, variable temperature measurements were performed at elevated temperatures in order to investigate the variation of the phonon mode parameters with the increase in the sample volume at elevated temperatures.

2.3 Theory

2.3.1 Spectroscopic ellipsometry

Spectroscopic ellipsometry is a measurement technique, which quantifies the change in the polarization of light $\tilde{\rho}$ after interaction with a sample.[6,7,20] In the case of reflection, the change in polarization can be written as

$$\tilde{\rho} = \frac{\tilde{r}_{\mathrm{p}}}{\tilde{r}_{\mathrm{s}}} = \tan(\Psi) e^{i\Delta}, \tag{2.1}$$

where $\tilde{r}_{\mathrm{p}}$ and $\tilde{r}_{\mathrm{s}}$ are the complex-valued Fresnel reflection coefficients for light polarized parallel (p) and perpendicular (s) to the plane of incidence. At each frequency, a (Ψ, Δ) pair is measured, where Ψ is rotation of the light's polarization state (about its axis of propagation), and Δ is the relative phase shift between the p and s components.

2.3.2 Optical model approach

To extract physically meaningful quantities from SE data (Ψ, Δ), an appropriate optical model must be implemented. The optical model used here consists of ambient air, a surface roughness layer, and bulk single-crystal ThO_2 or UO_2, where all constituents meet at plane parallel interfaces. The dielectric function for the surface roughness layer ($\epsilon_{\mathrm{rough}}$) is calculated by averaging the ambient air ($\epsilon_{\mathrm{air}} = 1$) and bulk ($\epsilon_{\mathrm{bulk}}$) dielectric functions, via $\epsilon_{\mathrm{rough}} = (1 + \epsilon_{\mathrm{bulk}})/2$. For the ThO_2 sample, a small silver contact (1% surface area coverage) must be included in the optical model to account for the metallic reflectivity of a small electric contact, which was furbished onto the sample.

For the temperature and spectral range investigated here, the dominant con-

tributions to $\epsilon(\omega)$ come from IR-active phonon modes. The optical response of IR-active phonon modes can be modeled using anharmonic broadened Lorentz oscillators,[20] which can be cast into the so-called four-parameter semi-quantum (FPSQ) model.[25] The FPSQ model was motivated by Gervais and Piriou permitting for different phonon decay times of LO and TO modes in crystals with multiple branches of phonon modes. By allowing for independent damping parameters of TO and LO modes, anharmonic effects in multiple (polar) phonon-mode materials can be modelled.[26,27,25,28] We used the following model dielectric function to describe ε:

$$\varepsilon(\omega) = \varepsilon_\infty \prod_{i=1}^{N} \frac{\omega_{\mathrm{LO},i}^2 - \omega^2 - i\omega\gamma_{\mathrm{LO},i}}{\omega_{\mathrm{TO},i}^2 - \omega^2 - i\omega\gamma_{\mathrm{TO},i}}. \tag{2.2}$$

Here, index i specifies the phonon mode pair number, and N is the total number of mode pairs. Corresponding to every phonon mode pair is a lattice resonance with transverse optic (TO) and longitudinal optic (LO) character. To avoid confusion, we refer to each term in Eq. 2.2 as "mode pairs" (i = 1, 2, ...), and their corresponding TO and LO components as just "modes". The parameters ω_{TO}, γ_{TO}, ω_{LO}, γ_{LO}, and ε_∞ are the: resonant frequency and broadening of the TO resonance, resonant frequency and broadening of the LO resonance, and high frequency dielectric constant, respectively. Anharmonic phonon interactions may comprise, for example, optical phonon decays into acoustic phonons (by cubic or quartic anharmonicities).[29]

2.3.3 Density functional theory calculations

Theoretical calculations of long wavelength active Γ-point phonon frequencies were performed by plane wave density functional theory (DFT) using Quan-

tum ESPRESSO (QE).[30] We used the generalized gradient approximation (GGA) exchange correlation functional of Perdew, Burke and Ernzerhof (PBE)[31] and ultrasoft pseudopotentials from the PSLibrary version 1.0.[32] The valence configuration for thorium used here is [Rn] $5f^{0.5}$ $6d^{1.5}$ $7s^2$. The standard fcc fluorite structures were first relaxed to force levels less than 10^{-5} Ry Bohr^{-1}. A regular shifted $8 \times 8 \times 8$ Monkhorst-Pack grid was used for sampling of the Brillouin zone.[33] A convergence threshold of 10^{-12} Ry was used to reach self consistency with large electronic cutoffs of 110 Ry for the wavefunction and 1000 Ry for the charge density. The structural relaxation yielded lattice constants of 5.61 Å for ThO_2 and 5.37 Å for UO_2. The fully relaxed cells were used for subsequent DFT phonon calculations.[34]

According to Born and Huang,[36] the lattice dynamic properties in crystals are categorized under different electric field **E** and dielectric displacement **D** conditions.[37] Specifically, $\mathbf{E} = 0$ and $\mathbf{D} = 0$ define the transverse optical (TO) modes, associated with the dipole moment. $\mathbf{E} \neq 0$ but $\mathbf{D} = 0$ define the longitudinal optical (LO) modes. The latter can be obtained using Born effective charges calculated by the QE's phonon code.[38] Thus, the parameters of the TO modes are obtained as eigenvalues and eigenvectors of the dynamic matrix without the electric field effects. The parameters of the LO modes were obtained by adding so called non-analytical terms to the dynamic matrix in appropriate crystal directions. In cubic crystals, the tensors of Born effective charges are isotropic, which leads to the same eigenvector being the solution for both the TO and LO mode as shown in Figure 2.1. From the point of view of DFT, a low bandgap UO_2 is a semimetal, which makes the calculations of Born effective charges (and any other electric-field-related properties) problematic at this particular level of theory. Therefore, we focused on calculations of phonon

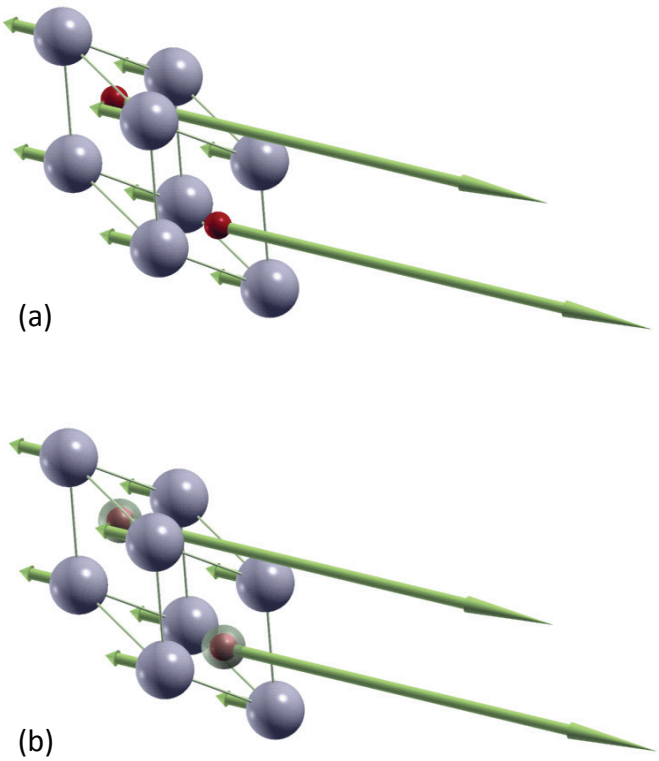

Figure 2.1: Examples of TO (a) and the corresponding LO (b) modes for ThO_2 are shown for the primitive unit cell. Please, note that the modes, i.e. the atomic displacement patterns, are exactly the same for these two modes. As described in the text, the TO mode is an eigenvector of the dynamic matrix of interatomic force constants. The LO mode was obtained by adding the non-analytical terms to the dynamic matrix in the direction of the transition dipole of the TO. Semi-transparent isosurfaces of electron charge density are shown around the oxygen atoms in (b).

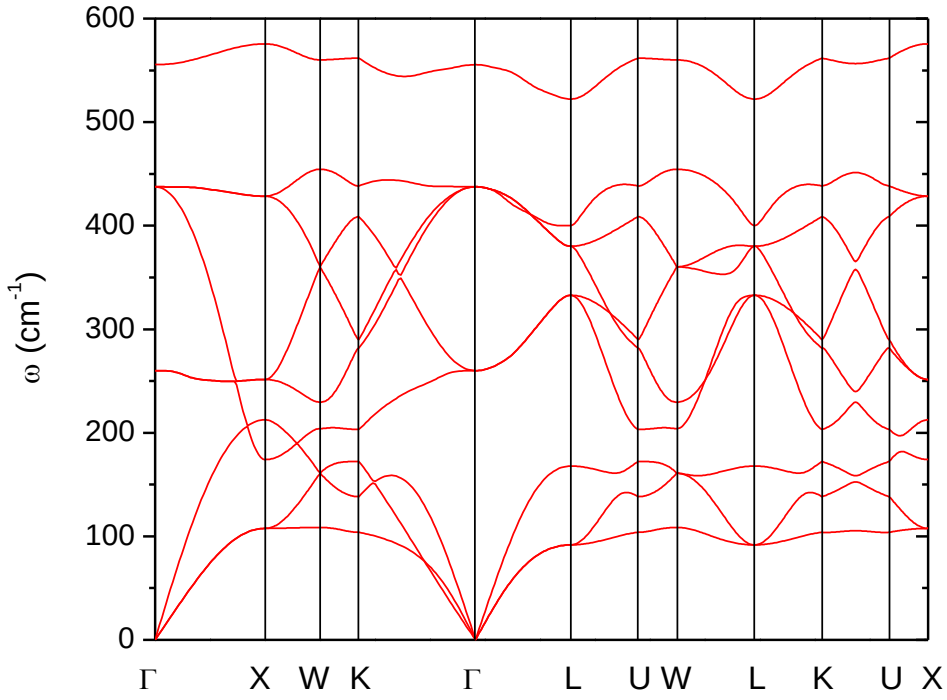

Figure 2.2: The phonon dispersion along a high symmetry path in the Brillouin zone for ThO_2. Labeling of high symmetry points as in Ref. 35.

properties of ThO_2. It is worth noting, however, that due to the similarity of the crystal structure and the atomic mass, the lattice dynamical properties of ThO_2 are expected to be qualitatively valid for UO_2 as well. In addition to the Γ-point phonons, the dynamical matrices were calculated over a regular $8 \times 8 \times 8$ grid in the first Brillouin zone. They were used to produce real-space interatomic force constants, which in turn were used to plot the complete phonon dispersion along a high-symmetry path through the first Brillouin zone, shown in Fig. 2.2.

The fluorite crystal structure with three atoms in the primitive cell possesses nine phonon modes, three acoustic, and six optical modes. The optical phonon modes further divide into three triply degenerated IR-active modes and three triply degenerated Raman-active modes. Partial charges on atoms are quanti-

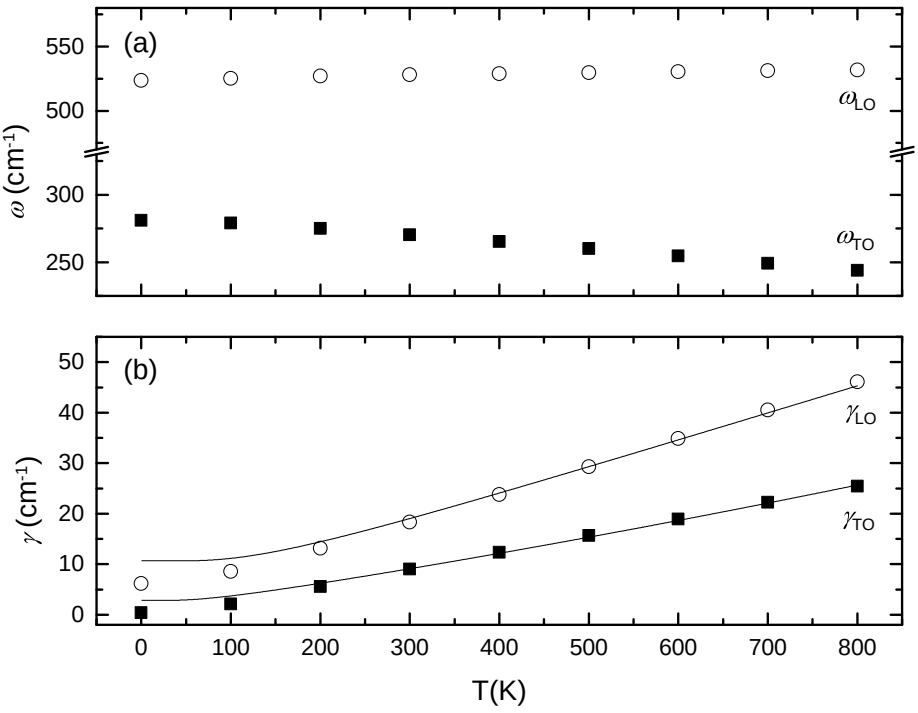

Figure 2.3: Results of the anharmonic DFT calculations for energy (a) and broadening parameters (b) of TO and LO phonon modes as a function of temperature. Solid lines in (b) are fits to Eq. 2.4. The resulting best-match model fit parameters are given in the text.

fied in terms of Born effective-charge tensors, i.e., mixed second-order derivatives with respect to atomic displacement and electric field.[38] For ThO_2 the Born effective-charge tensors are isotropic and the positive charge on thorium equals the sum of negative charges on both oxygen atoms. Thus, the electric field adds to the restoring force of the mode, which results in the higher frequency of the LO mode while the eigenvector direction of the dynamic matrix does not change. The LO mode is the highest frequency branch in the phonon dispersion plot (between 500 and 600 cm^{-1}). Figure 2.1 shows renderings of atomic displacements for TO and LO modes as examples prepared using XCrysDen[39] running under Silicon Graphics Irix 6.5.

In order to verify the general trends of energy and broadening of the TO and

LO phonon modes, we performed anharmonic calculations using D3Q code integrated with the QE distribution.[40,41,42] Due to the limitations of the code (only implemented for norm-conserving pseudopotentials) for these calculations we used Hamann-Schlüter-Chiang-Vanderbilt (HSCV)[43] pseudopotentials and Perdew-Zunger (PZ)[44] local density approximation exchange-correlation functional. The calculations were performed on a regular shifted $6 \times 6 \times 6$ Monkhorst-Pack grid with a large cutoff of 200 Ry for the wavefunction. These parameters were tested to provide convergence of the harmonic phonon frequencies to the level of 0.1 cm^{-1}. The structure was again fully relaxed using the same criteria as for the GGA calculations described above and the subsequent phonon calculations (second order harmonic and third order anharmonic) were performed on a regular $8 \times 8 \times 8$ grid in the first Brillouin zone. The resulting anharmonic dynamical matrices were used to compute the intrinsic phonon-phonon interactions, i.e., widths and energies of phonon modes as a function of temperature in the temperature range of 0 K – 800 K. Calculations were performed at a small displacement (1×10^{-5} of the reciprocal lattice vector) from the Γ point, on a $200 \times 200 \times 200$ regular unshifted grid, and with the Gaussian smearing parameter of 10 cm^{-1}. The results are presented in Figure 2.3.

2.4 Experiment

2.4.1 Crystal growth

Hydrothermal synthesis was used to grow the ThO_2 and UO_2 single-crystals investigated in this work.[45,46] Similar growth procedures were implemented for both ThO_2 and UO_2. The mineralizer solution for both growth reactions

was a 6M cesium fluoride solution (Alfa Aesar, 99.99%). Growth reactions were contained in sealed silver ampoules (99.95% Ag, Refining Systems Inc.).

For the ThO_2 single-crystal, a ThO_2 seed crystal was suspended in the upper end of the silver ampoule on a silver seed rack. A charge of ThO_2 nutrient/feedstock (99.99% thorium oxide, International Bio-analytical Laboratories) was placed into the lower end of the tube, with a porous silver baffle separating the feedstock and the seed crystal. The silver tubes were then placed in a 250 mL Inconel autoclave. Band heaters were installed on the autoclave to form two temperature zones (feedstock and seed crystal zones). The dissolution zone temperature was 650°C and the crystallization zone was 600°C. This generated a pressure of 172 MPa. These conditions were maintained for 90 days.

The UO_2 single-crystal was also grown on a ThO_2 seed crystal. The mineralizer solution, temperatures, and pressures were the same for the UO_2 (99.998% uranium oxide, International Bio-analytical Laboratories) growth procedure. However, the growth was only maintained for 50 days.

Both crystals were ground down to the (100) surface (3000 grit, Ultra Tec V5 faceting machine) and polished (0.10 μm diamond slurry applied to a ceramic lap). The final dimensions of the ThO_2 single-crystal are $(12\times6\times1)$ mm^3. The dimensions of the UO_2 single-crystal are $(5\times5\times1)$ mm^3.

2.4.2 Ellipsometric measurements

Spectroscopic ellipsometry in reflection was the measurement technique employed here. For the room temperature measurements on ThO_2 and UO_2, the ellipsometric parameters Ψ and Δ were measured from 100 cm^{-1} to 7000 cm^{-1} with a resolution of 2 cm^{-1}. Data from 100 cm^{-1} to 400 cm^{-1} was acquired using a home-built Fourier transform-based far-infrared ellipsometer.[5] Data from

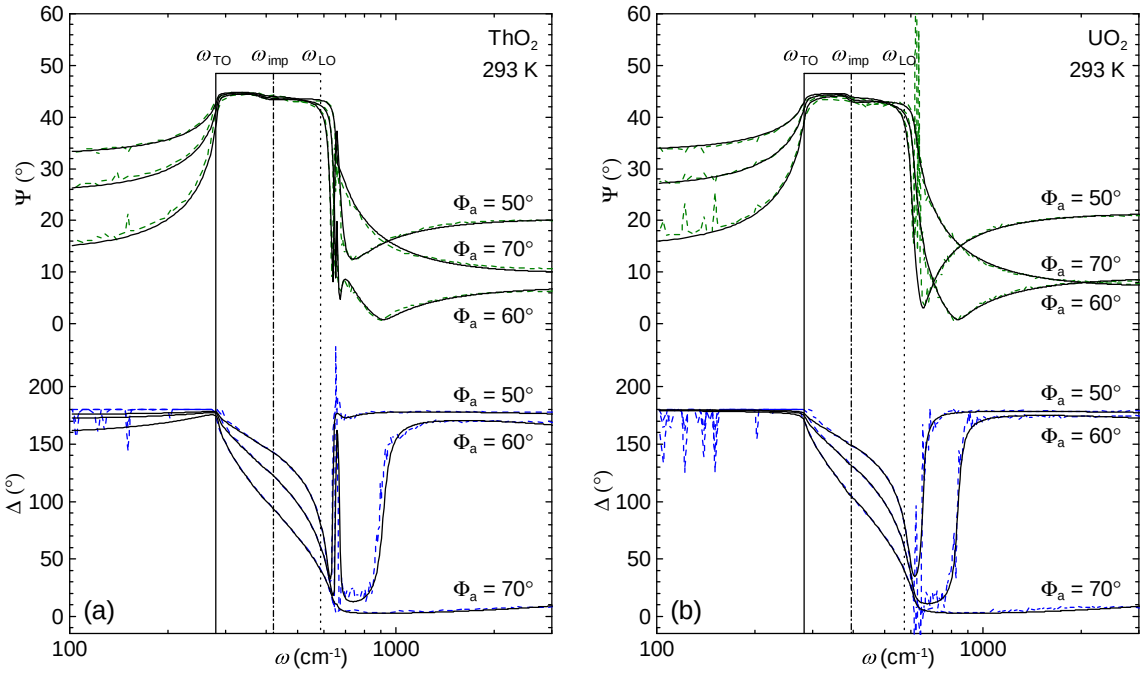

Figure 2.4: Experimental (dashed lines) and best-match model calculated (black solid lines) ellipsometric data (Ψ, Δ) for single-crystal ThO_2 (panel (a)) and UO_2 (panel (b)). The optical model parameters ω_{TO} (solid vertical lines) and ω_{LO} (dashed vertical lines) are the TO and LO frequencies, respectively, that correspond to the main IR-active phonon modes. The parameter ω_{imp} (= $\omega_{TO,imp}$ = $\omega_{LO,imp}$) (dash-dot vertical lines) corresponds to the small-amplitude IR-active impurity-like mode pair within the reststrahlen band. Data are taken at three angles of incidence (Φ_a = 50°, 60°, and 70°), and at room temperature.

400 cm^{-1} to 7000 cm^{-1} was acquired using a commercially available Fourier transform-based mid-infrared ellipsometer (IR-VASE, J.A. Woollam Co. Inc.). These measurements were performed at three angles of incidence (Φ_a = 50°, 60°, and 70°). The WVASE software (J.A. Woollam Co. Inc.) was used to acquire and analyze all data. All measurements were performed in an open air environment.

For ThO_2, additional variable temperature measurements were taken from 293 K to 648 K in increments of 25 K. These were performed using only the far-infrared ellipsometer.[5] Ψ and Δ were measured from 100 cm^{-1} to 650 cm^{-1}

with a resolution of 2 cm^{-1}. These measurements were performed at a single angle of incidence ($\Phi_a = 70^\circ$).

To perform the variable temperature measurements, the ThO_2 crystal was mounted to an aluminum plate via vacuum seal. To elevate the temperature, the aluminum plate was heated by a pyrolytic boron nitride/pyrolytic graphite resistive heater. The temperature was read before and after each ellipsometric measurement by probing the sample surface with a k-type thermocouple. During the measurement, the thermocouple was removed from the surface.

2.5 Results and discussion

2.5.1 ThO_2 and UO_2 room temperature characterization

In order to characterize the IR-active phonon modes in ThO_2 and UO_2, we implemented the following three step approach. (i), we apply our optical model and model dielectric function approach to compare experimental data with best-match model calculated data to obtain the thickness of the surface roughness layer and to identify all IR-active modes. (ii), we extract $\mathrm{Re}\{\epsilon(\omega)\}$ and $\mathrm{Im}\{\epsilon(\omega)\}$ for ThO_2 and UO_2 for each measured wavelength separately by holding all other optical model parameters constant (surface roughness thickness and ThO_2 silver contact diameter). (iii), we perform a best-match model calculation using the FPSQ model and by directly comparing the result of the FPSQ model with the wavelength-by-wavelength obtained dielectric function obtained in the second step. In this best-match model calculation, we included evaluations of the match in $\epsilon(\omega)$ as well as the match in $\epsilon^{-1}(\omega)$ between model and wavelength-by-wavelength obtained dielectric function.

Step (i): shown in Fig. 2.4 is the best-match model calculated ellipsometry

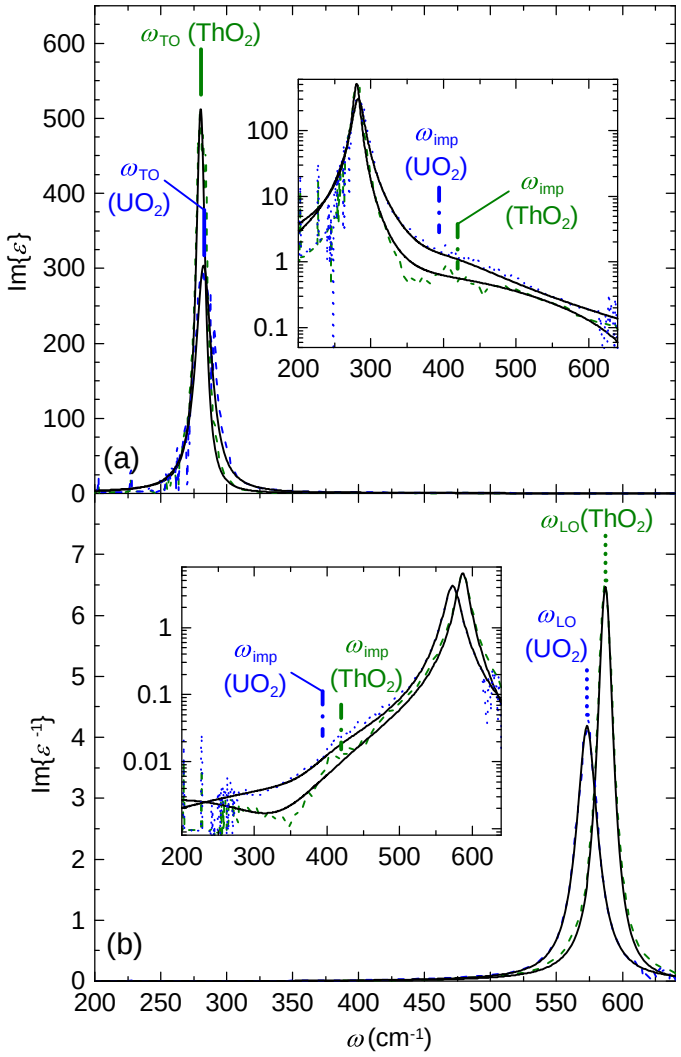

Figure 2.5: Wavelength-by-wavelength extracted (broken lines) and best-match model calculated (solid black lines) $\mathrm{Im}\{\epsilon(\omega)\}$ (panel (a)) and $\mathrm{Im}\{\epsilon^{-1}(\omega)\}$ (panel (b)) for single-crystal ThO_2 (green) and UO_2 (blue). The solid black lines show the best-match model calculation using Eq. 2.2 to the wavelength-by-wavelength extracted $\mathrm{Im}\{\epsilon(\omega)\}$ and $\mathrm{Im}\{\epsilon^{-1}(\omega)\}$. The resulting best-match model parameters are shown in Tabs. 2.1 and 2.2. The TO and LO resonant frequencies are labeled as ω_{TO} and ω_{LO} for the main phonon mode pair, and ω_{imp} (= $\omega_{\mathrm{TO,imp}}$ = $\omega_{\mathrm{LO,imp}}$) for the impurity-like mode pair. To make the impurity mode features visible, $\mathrm{Im}\{\epsilon(\omega)\}$ and $\mathrm{Im}\{\epsilon^{-1}(\omega)\}$ are also shown on a logarithmic scale (inset plots). Note, ω_{imp} does not exactly coincide with the corresponding peak in $\mathrm{Im}\{\epsilon(\omega)\}$, because the impurity mode broadening is comparable to ω_{imp}.

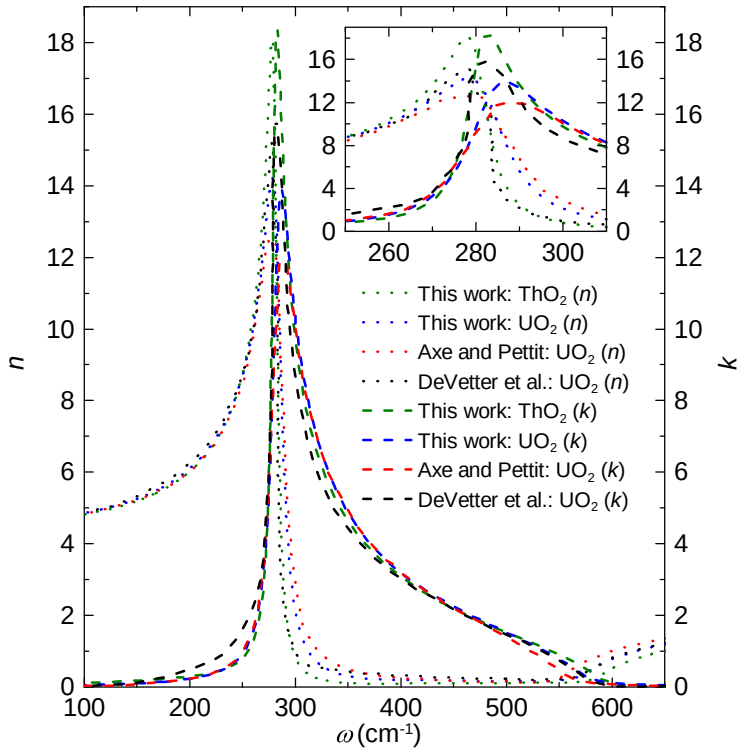

Figure 2.6: Resulting optical constants n and k for the room temperature analysis of ThO_2 and UO_2 compared with other n and k values from previous UO_2 characterizations. Optical constants determined in this work (ThO_2 (green lines) and UO_2 (blue lines)) were converted from the best-match model calculated dielectric function shown in Fig. 2.5. For comparison, dispersion model-calculated optical constants from Axe and Pettit[21] (red lines) were included, as well as values calculated from experimental reflectance spectra by DeVetter *et al.*[24] (black lines). Dotted lines were chosen for n and dashed lines for k.

data (black solid lines) to the experimental data (dashed lines) for ThO_2 (panel (a)) and UO_2 (panel (b)). The analysis yields a surface roughness layer thickness of (34 ± 1) nm for ThO_2, and (22 ± 1) nm for UO_2. In addition to the main mode pair, a small IR-active impurity-like mode pair is detected for both crystals within the reststrahlen band (band of high reflectivity). Because only two mode pairs are observed, we designate the impurity mode pair index as i = "imp", and the main mode pair index as null (i = ""). We find there is limited

sensitivity to the parameters $\omega_{\mathrm{TO,imp}}$ and $\omega_{\mathrm{LO,imp}}$, therefore they were set equal in the model analysis ($\omega_{\mathrm{imp}} = \omega_{\mathrm{TO,imp}} = \omega_{\mathrm{LO,imp}}$), as was done in Ref. 47 for impurity-like modes detected in α-GaN thin films. In Fig. 2.4, the impurity mode resonant frequency is labeled as ω_{imp}, and the main mode as ω_{TO} and ω_{LO}. The occasional spike-like features in Ψ and Δ (Fig. 2.4) are due to noise in low-reflectivity spectral ranges. For the ThO_2, the small silver contact area was found to be approximately 1% surface coverage of the sample. The analysis verifies both crystals are optically isotropic for the given temperature and spectral range. No significant contribution from free charge carriers is detected.

Step (ii): shown in Fig. 2.5 is the wavelength-by-wavelength extracted $\mathrm{Im}\{\epsilon(\omega)\}$ (panel (a)) and $\mathrm{Im}\{\epsilon^{-1}(\omega)\}$ (panel (b)) for ThO_2 (green dashed lines) and UO_2 (blue dotted lines). The resulting best-match calculated ellipsometry data are virtually indistinguishable from the measured data and are therefore not included into Fig. 2.4.

Step (iii): shown in Fig. 2.5 is the best-match model dielectric function obtained using the FPSQ model (black solid lines), obtained by direct comparison with the wavelength-by-wavelength extracted dielectric function. Shown in Tab. 2.1 are the resulting fit parameters for the main mode pair, DFT calculated parameters, and previous results from reflectance spectroscopy. Our results are similar to previous characterizations and our DFT calculations. For the experiments that report values of γ_{TO} and γ_{LO}, it holds true that $\gamma_{\mathrm{TO}} < \gamma_{\mathrm{LO}}$. The anharmonicity indicated by $\gamma_{\mathrm{TO}} \neq \gamma_{\mathrm{LO}}$ is thought to arise from anharmonic coupling between different phonon modes.[48,25,26] The impurity mode pair also exhibits anharmonicity since $\gamma_{\mathrm{TO,imp}} > \gamma_{\mathrm{LO,imp}}$. Best-match model results for the impurity mode parameters in both crystals are given in Table 2.2. The anharmonic DFT calculations on ThO_2 show $\gamma_{\mathrm{TO}} < \gamma_{\mathrm{LO}}$ as well [Fig. 2.3].

Since our DFT calculations do not consider any impurity modes, this establishes the anharmonicity in the main phonon mode pair in ThO_2 is intrinsic to the material, and does not depend on the existence of an impurity like-mode pair. However, the existence of impurities could of course influence the phonon properties.

2.5.2 ThO_2 variable temperature characterization

To further investigate ThO_2, we performed ellipsometric measurements as a function of temperature from 294 K to 648 K. The spectra acquired at each temperature increment are analyzed independently, and using the model approach described at room temperature. To examine the influence of heat on the surface roughness layer, a separate, variable temperature experiment was performed in the visible spectral range (1.0 eV to 6.5 e.V., RC2, J.A. Woollam Co., Inc.). No significant change in the roughness layer's thickness or dielectric function was observed. We further assume that the IR optical properties of the small silver contact area remain temperature independent. Therefore, we held these optical model parameters constant as a function of temperature.

Using the approach described previously, we performed a wavelength-by-wavelength fit to extract $\mathrm{Re}\{\epsilon(\omega)\}$ and $\mathrm{Im}\{\epsilon(\omega)\}$ for each measured temperature. The FPSQ model is then fit to the wavelength-by-wavelength extracted $\epsilon(\omega)$ and $\epsilon^{-1}(\omega)$ [Fig. 2.7]. The resulting main mode pair and impurity mode pair parameters are shown in Fig. 2.7. For the main mode pair, the resonant frequency parameters (ω_{TO} and ω_{LO}) decrease with increasing temperature, whereas the broadening parameters (γ_{TO} and γ_{LO}) increase with increasing temperature, which is a typical behavior for IR-active phonon modes.[51] For the impurity-like mode pair, ω_{imp} decreases with increasing temperature, but

Table 2.1: Best-match model results for the room temperature IR-active phonon mode parameters in single-crystal ThO_2 and UO_2. Error bars shown for this work correspond to the 90% confidence interval within the best-match model data analysis. The low-frequency (static) dielectric constant ε_{DC} is calculated using the Lyddane-Sachs-Teller (LST) relation.[49]

Parameter	DFT (this work)	Ellipsometry (this work)	
	ThO_2	UO_2	ThO_2
ω_{TO} (cm^{-1})	260	(282.8 ± 0.2)	(280.5 ± 0.1)
ω_{LO} (cm^{-1})	554.8	(573.3 ± 0.5)	(587.5 ± 0.2)
γ_{TO} (cm^{-1})	9.0[f]	(14.8 ± 0.5)	(8.2 ± 0.2)
γ_{LO} (cm^{-1})	18.4[f]	(20.1 ± 1.1)	(16.1 ± 0.5)
ε_∞	4.79	(5.2 ± 0.2)	(4.7 ± 0.1)
ε_{DC}	21.9	21.1	20.4

Parameter	Axe and Pettit[a]		Chernia[b]
	UO_2	ThO_2	UO_2
ω_{TO} (cm^{-1})	(278 ± 2)	(279 ± 2)	283.4
ω_{LO} (cm^{-1})	(556 ± 4)	(568 ± 4)	574.0
γ_{TO} (cm^{-1})	18.5	16.2	29.4
γ_{LO} (cm^{-1})	-	-	30.4
ε_∞	5.51	4.86	5.46
ε_{DC}	21.31	19.71	22.36

Parameter	Schoenes[c]	DeVetter *et al.*[d]	Dolling *et al.*[e]
	UO_2	UO_2	UO_2
ω_{TO} (cm^{-1})	(280 ± 2)	(277 ± 3)	(284 ± 4)
ω_{LO} (cm^{-1})	(578 ± 2)	(571 ± 1)	(557 ± 20)
γ_{TO} (cm^{-1})	7.5	-	-
γ_{LO} (cm^{-1})	14	-	-
ε_∞	5.0	-	-
ε_{DC}	21.5	-	-

[a]Ref. 21: ω_{TO} and ω_{LO} from Kramers-Kronig analysis. γ_{TO}, ε_∞, and ε_{DC} from best-match model parameter results using a Lorentz oscillator to render the dielectric function behavior.
[b]Ref. 22.
[c]Ref. 23.
[d]Ref. 24.
[e]Ref. 50.
[f]From the anharmonic calculation at 300K.

Table 2.2: Best-match model results for the room temperature IR-active impurity-like phonon mode parameters in single-crystal ThO_2 and UO_2. Error bars shown correspond to the 90% confidence interval within the best-match model data analysis.

Parameter	Ellipsometry (this work)	
	UO_2	ThO_2
ω_{imp} (cm^{-1})	(394.3 ± 20.3)	(419.6 ± 11.4)
$\gamma_{TO,imp}$ (cm^{-1})	(143.5 ± 85.5)	(511.9 ± 68.6)
$\gamma_{LO,imp}$ (cm^{-1})	(133.8 ± 80.2)	(443.7 ± 59.5)

interestingly $\gamma_{TO,imp}$ and $\gamma_{LO,imp}$ decrease with increasing temperature. This anomalous behavior is discussed in more detail below.

To model the temperature-dependence of the resonant frequencies and broadening parameters, we followed the same approach as in Ref. 28. Similar to Ref. 28, we find the change in our resonant frequencies is directly proportional to the change in volume of the crystal lattice. The change in resonant frequencies for a given change in volume can be quantified by the mode Grüneisen parameter g_j, where the index j specifies the particular lattice resonance (here j = TO, LO, or imp). Assuming a temperature-independent g_j, the change in the j^{th} resonant frequency can be written as $\Delta\omega_j(T) = -\omega_j g_j(\Delta V(T)/V)$, where ω_j is the initial resonant frequency and V is the lattice volume.[28] This form also assumes that the only change in $\omega_j(T)$ is due to the lattice expansion. Other temperature-dependent contributions, such as anharmonicity (i.e. the real part of the phonon self-energy), electron-phonon coupling, spin-phonon coupling, etc., were not considered.[52,25] If this model is unable to fit $\Delta\omega_j(T)$, this is indicative of other contributions to the frequency shift. To express $(\Delta V(T)/V)$ in terms of the linear expansion coefficient α_L and change in temperature ΔT, we write $(\Delta V(T)/V) = 3\alpha_L\Delta T$, where the volume expansion coefficient $\alpha_V = 3\alpha_L$ (assuming small differential changes in an isotropic material). Rear-

ranging the prior equation for $\Delta\omega_j(T)$ to only fit for g_j yields

$$\omega_j(T) = -\omega_{j,init}(g_j 3\alpha_L)(T - T_{init}) + \omega_{j,init}. \quad (2.3)$$

Here, $\omega_{j,init}$ and T_{init} are the initial resonant frequency and temperature ($\omega_{j,init} = \omega_j(T_{init})$, $T_{init} = 293$ K). For ThO_2, we find the average linear expansion coefficient in our temperature range is $\alpha_L = 9.9 \times 10^{-6}$ K^{-1}.[53] Fitting Eq. 2.3 to our results for $\omega_{TO}(T)$, $\omega_{LO}(T)$, and $\omega_{imp}(T)$ gives $g_{TO} = 3.3 \pm 0.1$, $g_{LO} = 0.8 \pm 0.02$, and $g_{imp} = 17.1 \pm 1.0$ [Fig. 2.7(c)]. The results for g_{TO} are in excellent agreement with previous DFT calculations, which predict $g_{TO} \approx 3.2$, only considering volume change effects on the harmonic mode frequency.[19] This suggests the temperature-induced change in ω_{TO} is primarily due to volume expansion of the crystal lattice, and other temperature-dependent contributions are not significant, or perhaps counterbalance each other.[28] However, the g_{LO} parameter calculated in Ref. 19 is larger than our experimentally determined value. This could mean the change in ω_{LO} is due to other temperature-dependent contributions besides a pure volume change. In our anharmonic DFT calculations, performed at a fixed cell volume, i.e., only including the effect of phonon self-energy, the frequency shift of the LO mode has a positive slope [Fig. 2.3], possibly compensating the effect of the lattice expansion. It is worth noting though, that our calculations only include third order anharmonicity, while fourth order contributions, if present, can in principle be of the same order of magnitude as the third order one, and not necessarily with the same sign, further complicating the picture. For $\omega_{imp}(T)$, the trend is not perfectly linear, contrary to what Eq. 2.3 predicts. This also indicates other mechanisms besides volume change.

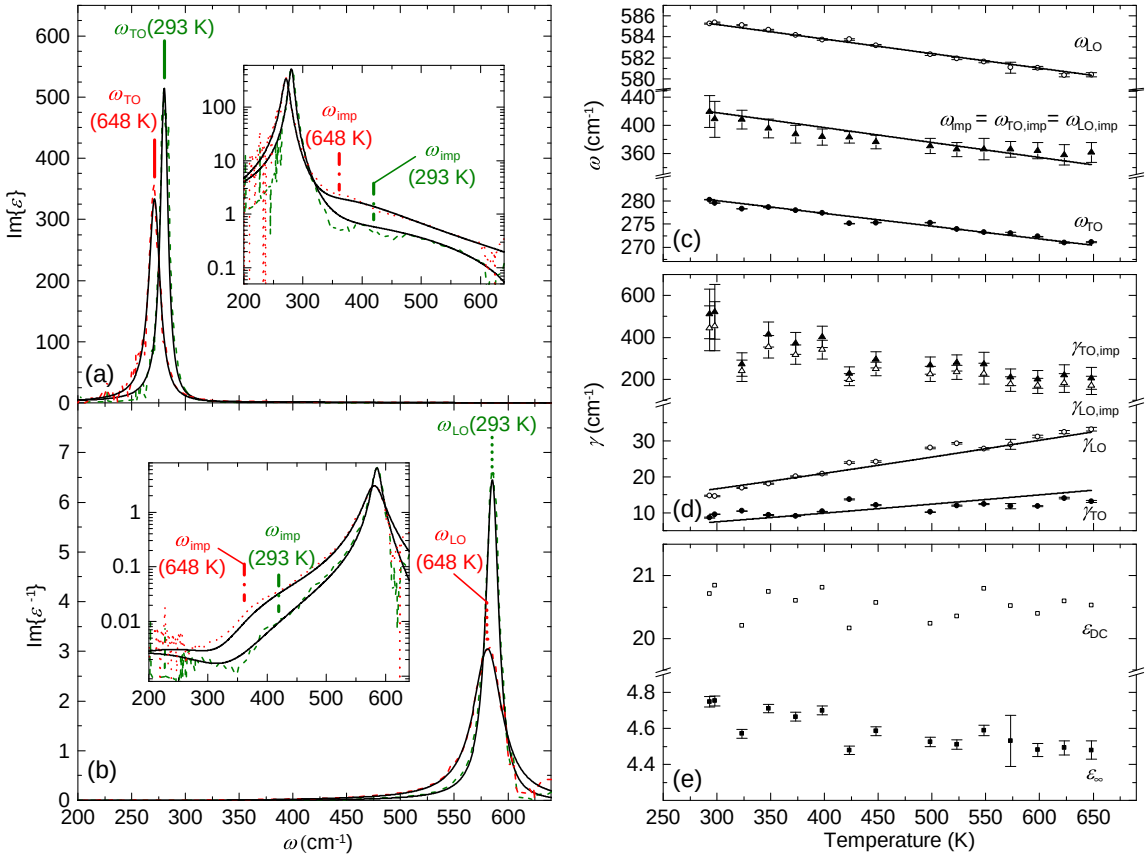

Figure 2.7: Results for ThO_2 variable temperature characterization. Wavelength-by-wavelength extracted (broken lines) and best-match model calculated (solid black lines) Im$\{\epsilon(\omega)\}$ (panel (a)) and Im$\{\epsilon^{-1}(\omega)\}$ (panel (b)) for single-crystal ThO_2 at 293 K (green) and 648 K (red). To make the impurity mode features visible, Im$\{\epsilon(\omega)\}$ and Im$\{\epsilon^{-1}(\omega)\}$ are also shown on a logarithmic scale (inset plots in panels (a) and (b)). The solid black lines in panels (a) and (b) show the best-match model results of Eq. 2.2 to the wavelength-by-wavelength extracted Im$\{\epsilon(\omega)\}$ and Im$\{\epsilon^{-1}(\omega)\}$. The resulting FPSQ model parameters for all measured temperatures are shown in panels (c)-(e). The low-frequency (static) dielectric constant ε_{DC} is calculated using the Lyddane-Sachs-Teller (LST) relation.[49] The solid black lines in panel (c) show the best-match model results using Eq. 2.3 to match $\omega_j(T)$. The solid black lines in panel (d) show the best-match model using Eq. 2.4 for $\gamma_j(T)$.

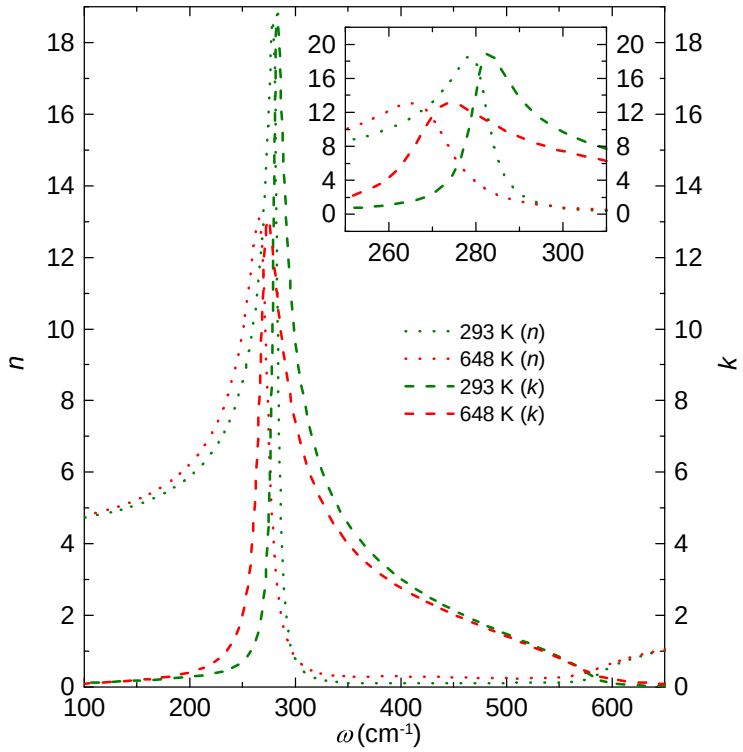

Figure 2.8: Resulting optical constants n and k for the variable temperature charaterization of ThO_2. Optical constants (green for 293 K and red for 648 K) were determined by converting the best-match model calculated dielectric function shown in Fig. 2.7. Dotted lines are chosen for n and dashed lines for k.

To investigate the mechanism of anharmonic phonon-phonon scattering, we implement the Bose-Einstein based model for $\gamma_j(T)$ employed in Ref. 25. Since $\gamma_{TO}(T)$ and $\gamma_{LO}(T)$ are reasonably linear within our temperature range, the only term in the equation needed is the one which corresponds to decay via cubic anharmonicities[28]

$$\gamma_j(T) = a_j\left[n\left(\frac{\omega_j(T)}{2}\right) + \frac{1}{2}\right], \tag{2.4}$$

where $n(\tilde{\omega}) = (e^{\hbar\tilde{\omega}/k_B T} - 1)^{-1}$ is the phonon occupation number evaluated at the average frequency $\tilde{\omega} = (\omega_j(T)/2)$. The parameters $\hbar$, k_B, a_j are the reduced

Planck constant, the Boltzmann constant, and the cubic anharmonic parameter, respectively. Fitting Eq. 2.4 to $\gamma_{\mathrm{TO}}(T)$ and $\gamma_{\mathrm{LO}}(T)$ gives $a_{\mathrm{TO}} = (4.8 \pm 0.2)$ cm^{-1} and $a_{\mathrm{LO}} = (20.2 \pm 0.4)$ cm^{-1}. Our anharmonic DFT calculated results for $\gamma_{\mathrm{TO}}(T)$ and $\gamma_{\mathrm{LO}}(T)$ [Fig. 2.3] give similar fit parameter results of $a_{\mathrm{TO}} = (5.7 \pm 0.1)$ cm^{-1} and $a_{\mathrm{LO}} = (21.3 \pm 0.6)$ cm^{-1}. A larger temperature range is used when fitting the DFT results (0 K to 800 K) than for our ellipsometry results (293 K to 648 K). However, the a_{TO} and a_{LO} for DFT are nearly identical when only including data within the range 293 K to 648 K. We can then conclude that the dominant decay mechanism can be described phonon-phonon interactions via cubic anharmoncities.[29] It is worth noting that the Eq. 2.4 was introduced in Ref. 25 to describe the decay of optical phonons into pairs of acoustic phonons via cubic anharmonicities, while the anharmonic DFT code considers a more complex decay mechanism involving triplets of phonons at arbitrary wavevectors over a fine grid of q-points within the Brillouin zone (in our case on a grid of $200 \times 200 \times 200$ points). The Eq. 2.4 however, describes thermal occupations of phonon states within the Bose-Einstein statistics and hence should be applicable in either case.

Interestingly, $\gamma_{\mathrm{TO,imp}}(T)$ and $\gamma_{\mathrm{LO,imp}}(T)$ decrease with increasing temperature. This dependence cannot be fit by the model in Ref. 25, and is not typical for IR-active phonon modes in pure crystals.[51] However, the temperature-dependence of impurity-like modes is not well understood. While the exact nature of the impurity mode is unclear, it may be a result of subtle anharmonic phonon-phonon interactions, as reported for MgO.[54] This however, falls outside of the scope of our current study.

2.6 Conclusion

In summary, IRSE experiments and DFT calculations were used to study the IR-active phonon modes in ThO_2 and UO_2. Their dielectric functions are extracted from the ellipsometric data in order to determine the phonon mode resonant frequency and broadening parameters. In agreement with previous results, we find $\gamma_{TO} < \gamma_{LO}$ for both crystals, which is indicative of lattice anharmonicity due to anharmonic interaction between phonon modes. For ThO_2, additional ellipsometric measurements were performed at elevated temperatures. For the main TO resonance, our experimentally determined results for the mode Grüneisen parameter are in excellent agreement with previous DFT calculations, which suggests the temperature-induced change in the TO resonant frequency is due to volume expansion of the crystal lattice. However, the mode Grüneisen parameter for the main LO resonance does not exactly match the DFT predictions. This indicates the temperature-dependence of the LO resonant frequency is determined by additional factors besides just volume change. By implementing the Bose-Einstein based model in Ref. 25 to describe the broadening's temperature-dependence, we find the decay mechanism of the main mode's IR-active phonons can be described as cubic anharmonicity. For the detected impurity-like mode pair, the broadening parameters decrease with increasing temperature. This behavior is not predicted by the Bose-Einstein model, and more investigation is need to understand temperature-dependence of the impurity-like modes.

2.7 Acknowledgements

This work was supported in part by the National Science Foundation under award DMR 1420645 (Nebraska Materials Research Science and Engineering Center), and under award DMR 1808715. This work was supported in part by the Air Force Office of Scientific Research under award FA9550-18-1-0360, and by the Defense Threat Reduction Agency (Grant No. HDTRA1-14-1-0041), and the Domestic Nuclear Detection Office of the Department of Homeland Security (Grant No. HSHQDC14X00089). J. M. M. was supported by the Center for Thermal Energy Transport under Irradiation, an Energy Frontier Research Center funded by the U.S. Department of Energy, Office of Science, Office of Basic Energy Sciences. S. K., R. K., A. M. and M. S. acknowledge partial support by the J. A. Woollam Foundation. Density functional theory calculations were performed at the Holland Computing Center at the University of Nebraska, which receives support from the Nebraska Research Initiative. The views expressed in this article are those of the authors and do not necessarily reflect the official policy or position of the United States Air Force, Department of Defense, or the U.S. Government.

Chapter 3

Electron effective mass in Sn-doped monoclinic single crystal β-gallium oxide determined by mid-infrared optical Hall effect

3.1 Abstract

The isotropic average conduction band minimum electron effective mass in Sn-doped monoclinic single crystal β-Ga_2O_3 is experimentally determined by mid-infrared optical Hall effect to be $(0.284 \pm 0.013)m_0$ combining investigations on (010) and ($\bar{2}$01) surface cuts. This result falls within the broad range of values predicted by theoretical calculations for undoped β-Ga_2O_3. The result is also comparable to recent density functional calculations using the Gaussian-attenuation-Perdue-Burke-Ernzerhof hybrid density functional, which predict an average effective mass of $0.267m_0$. Within our uncertainty limits we detect no anisotropy for the electron effective mass, which is consistent with most previous theoretical calculations. We discuss upper limits for possible anisotropy of the electron effective mass parameter from our experimental uncertainty limits, and we compare our findings with recent theoretical results. (Reproduced from [S. Knight *et al.*, Appl. Phys. Lett. **112**, 012103 (2018).], with the permission of AIP Publishing)

3.2 Introduction

Single crystal gallium (III) oxide is a desirable material for optical and electronic applications due to its unique physical properties such as its transparent conducting nature and wide band gap.[3] As a transparent conductor, Ga_2O_3 is useful for various types of transparent electrodes, for example in flat panel displays,[55] smart windows,[56,57] photovoltaic cells,[56] and gas sensors.[58] Due to its wide band gap, Ga_2O_3 has a larger breakdown voltage than SiC and GaN, which makes it an excellent candidate for power devices.[59,60,61,62,63] Among the five phases, the monoclinic β phase is the most stable, and is expected to possess highly anisotropic properties which may prove useful for various applications.[64,65] Tuning of the free charge carrier concentration to enhance the electrical conductivity has been achieved by Sn doping, for example, which is a well established technique.[59]

Precise knowledge of the free charge carrier properties is imperative for electronic and optoelectronic device design and operation. Experimentally determined results for effective mass, free charge carrier concentration, and mobility parameters are currently scarce for β-Ga_2O_3. Numerous theoretical investigations have yielded a wide range of values for the electron effective mass: from $0.12m_0$ to $0.39m_0$, where m_o is the free electron mass.[66,67,68,63,69,70,71,72] Most calculations predict only minimal anisotropy. Although, recent Gaussian-attenuation-Perdue-Burke-Ernzerhof (Gau-PBE) hybrid density functional calculations predict slightly higher anisotropy.[68] Using a combination of optical transmission and electrical Hall effect measurements, the authors in Ref. 73 estimate a range of values for electron effective mass parameter along the **b** and **c** crystal directions to be $m_b^* = 0.5m_0$ to $1.0m_0$ and $m_c^* = 1.0m_0$ to $2.0m_0$,

respectively. Electrical Hall effect measurements on β-Ga_2O_3 allow access to free charge carrier concentration and mobility,[74,75,76,73] but this technique alone cannot resolve the effective mass parameter.

The optical Hall effect is a physical phenomenon exploited in our measurement technique, which employs generalized spectroscopic ellipsometry in combination with external magnetic fields to obtain the free charge carrier properties of semiconducting materials without electrical contacts.[5,77,78,79,4] This technique measures the change in the polarization of light after interaction with a sample due to a Lorentz force acting on the free charge carriers. In contrast with the electrical Hall effect, the optical Hall effect is capable of obtaining the effective mass, carrier concentration, mobility, and charge carrier type parameters simultaneously.

In this work, we experimentally determine the electron effective mass in Sn-doped monoclinic single crystal β-Ga_2O_3 by mid-infrared optical Hall effect (MIR-OHE) measurements. We compare our results to values reported in previous theoretical and experimental work, and we discuss the anisotropy of the effective electron mass parameter. Here we find no discernible anisotropy and assume an isotropic average parameter. We discuss the amount of finite anisotropy that may remain hidden within our present experimental error bars for the effective mass to be potentially discovered by subsequent experiments.

3.3 Experiment

Two surface cuts, (010) and ($\bar{2}$01), of Sn-doped single crystal β-Ga_2O_3 are investigated in this work. The crystals were grown using the edge-defined film-fed growth method by Tamura Corp. (Japan).[80,81,82] The dimensions for the (010)

surface are (0.65×10×10)mm, and (0.65×10×15)mm for the ($\bar{2}$01) surface. The optical response of β-Ga_2O_3 is governed by the monoclinic Cartesian dielectric function tensor.[83] Here the Cartesian direction **x** is contained within the sample surface plane and is oriented along the propagation direction of light incident on the sample. The **z** direction is oriented into the sample surface. The crystal directions in β-Ga_2O_3 are denoted **a**, **b**, and **c**, where the monoclinic angle β = 103.7° lies between **a** and **c**.[84] We choose to align **a** and **b** along **x** and **-z**, respectively, such that **c** lies within the **x-y** plane. For practicality, we introduce the direction $\mathbf{c}^\star$ parallel to **y**, so that **a**, **b**, and $\mathbf{c}^\star$ form a pseudo-orthorhombic system. We define azimuth angle ϕ as a rotation about the **z** axis for a given crystal axes orientation.[83] For the (010) surface, ϕ = 0° corresponds to **a** aligned along **x**. For the ($\bar{2}$01) surface, ϕ = 0° corresponds to **b** aligned along **y**.

Generalized spectroscopic ellipsometry is the measurement technique employed here to determine the free charge carrier properties of β-Ga_2O_3. Ellipsometric data is obtained using the Mueller matrix formalism.[6,85] WVASE (J.A. Woollam Co. Inc.) is used to acquire and analyze the data. The MIR-OHE data is measured using a home-built Fourier transform infrared ellipsometer in the spectral range of 550 cm^{-1} to 1500 cm^{-1} with a resolution of 2 cm^{-1}. The home-built ellipsometer is capable of attaining the upper-left 3 × 3 block of the complete 4 × 4 Mueller matrix.[5] The MIR-OHE data is obtained at +6 T, 0 T, and -6 T, with the magnetic field parallel to the incoming infrared beam. Each surface cut is measured at one in-plane azimuth orientation. These measurements are performed at angle of incidence Φ_a = 45° and at temperature T = 300 K. Additional measurements at zero field were performed at multiple in-plane orientations, and included into the data analysis. Note that the anisotropy of the effective mass parameter is determined by the anisotropy in the plasma

frequency as discussed further below. The anisotropy of the plasma frequency parameter is determined at zero field and multiple azimuth orientations. Hence, OHE data were only measured at one azimuth orientation for each sample.

In addition to the MIR-OHE measurements, zero magnetic field Mueller matrix data is measured at multiple azimuth orientations for each surface cut. The data is obtained using a commercially available MIR ellipsometer (IR-VASE, J.A. Woollam Co. Inc.) and the afore mentioned home-built ellipsometer in the spectral range of 150 cm^{-1} to 1500 cm^{-1} with a resolution of 2 cm^{-1}. The zero magnetic field data is not shown here, but is included in Ref. 83. These measurements are performed at Φ_a = 50°, 60°, and 70° and at room temperature.

3.4 Optical model approach

Ellipsometry is an indirect measurement technique which requires a physical parameterized model be fit to experimental data to determine the desired parameters.[7] The model approach used here is very similar to that of Ref. 83. The two phase optical model consists of ambient air and β-Ga_2O_3 joined at a planar interface. The dielectric function tensor of β-Ga_2O_3 at long wavelengths consists of contributions from optical phonon modes and free charge carriers. These contributions are modeled using the eigendielectric displacement vector summation approach described in Refs.[83,86]. In this approach contributions from individual dielectric resonances, in this case phonon modes and free charge carriers, are added to a high frequency dielectric constant tensor ε_∞. The anharmonically broadened Lorentz oscillator model is used to represent phonon resonance contributions.[86] No substantial Drude contribution was detected in the off-diagonal components of the monoclinic dielectric function tensor.[83] Thus,

we employ an orthorhombic Drude model where three independent Drude contributions are added to the dielectric function response along axes **a** (ε_{xx}), **b** (ε_{zz}), and **c*** (ε_{yy}).

The magnetic field dependent free charge carrier contribution to the dielectric function tensor $\varepsilon^{\mathrm{FC}}(\omega)$ is described using the classical Drude formalism including the change induced by the Lorentz force[4,5]

$$\varepsilon^{\mathrm{FC}}(\omega) = \frac{\boldsymbol{\omega_p}^2}{-\omega^2 \boldsymbol{I} - i\omega\boldsymbol{\gamma} + i\omega \begin{pmatrix} 0 & -b_z & b_y \\ b_z & 0 & -b_x \\ -b_y & b_x & 0 \end{pmatrix} \boldsymbol{\omega_c}}. \tag{3.1}$$

Here, $\boldsymbol{I}$ is the identity matrix, and $\langle b_x, b_y, b_z \rangle$ are the scalar components of magnetic field vector **B**, where each component is the projection along **x**, **y**, and **z**, respectively. At zero magnetic field, the classical Drude model parameters include the screened plasma frequency tensor $\boldsymbol{\omega_p} = \sqrt{Nq^2/\varepsilon_0 \boldsymbol{\varepsilon_\infty} \boldsymbol{m^*}}$, and the plasma broadening tensor $\boldsymbol{\gamma} = q/\boldsymbol{\mu}\boldsymbol{m^*}$. These parameters depend on the free charge carrier properties which include effective mass $\boldsymbol{m^*}$, free charge carrier volume density N, and mobility $\boldsymbol{\mu}$, where $\boldsymbol{m^*}$ and $\boldsymbol{\mu}$ are diagonal second rank tensors. In the isotropic average approximation of a given tensor, its values are replaced by an isotropic scalar and the corresponding unit matrix. The parameter ε_0 is the vacuum dielectric permittivity, and q is the elementary electric charge. At non-zero magnetic field, the cyclotron frequency tensor is $\boldsymbol{\omega_c} = q|\mathbf{B}|/\boldsymbol{m^*}$.

3.5 Results and Discussion

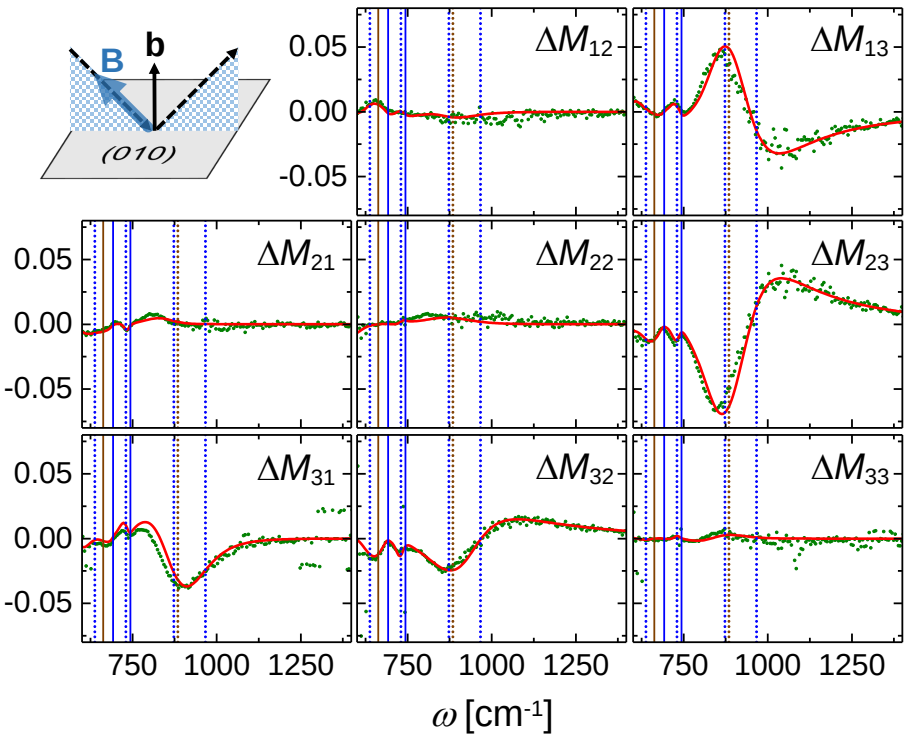

Figure 3.1: MIR-OHE experimental (green dots) and best-match model calculated (solid red lines) Mueller matrix difference spectra ($\Delta M_{ij} = M_{ij}(+6\ \mathrm{T}) - M_{ij}(-6\ \mathrm{T})$) for the (010) cut β-Ga_2O_3 sample at azimuth angle $\phi = 112.5^\circ$. All measurements are performed at temperature $T = 300$ K, and at angle of incidence $\Phi_a = 45^\circ$. The magnetic field **B** is parallel to the incoming infrared beam. Taken from Ref. 83, vertical lines signify the wave numbers of LPP (dotted lines) and transverse optical phonon modes (solid lines) polarized in the **a-c** plane (blue), and along the **b** axis (brown).

Figs. 3.1 and 3.2 show experimental and best-match model calculated MIR-OHE difference spectra for the (010) and ($\bar{2}$01) surface cut of β-Ga_2O_3, respectively. The MIR-OHE signals are strongest in the vicinity of the zero magnetic field reflectance minima for samples with a sufficient free charge carrier contributions.[87] For the samples investigated here, the reflectance minimum and MIR-OHE signal appear at the edge of the reststrahlen band at around 900 cm^{-1}.

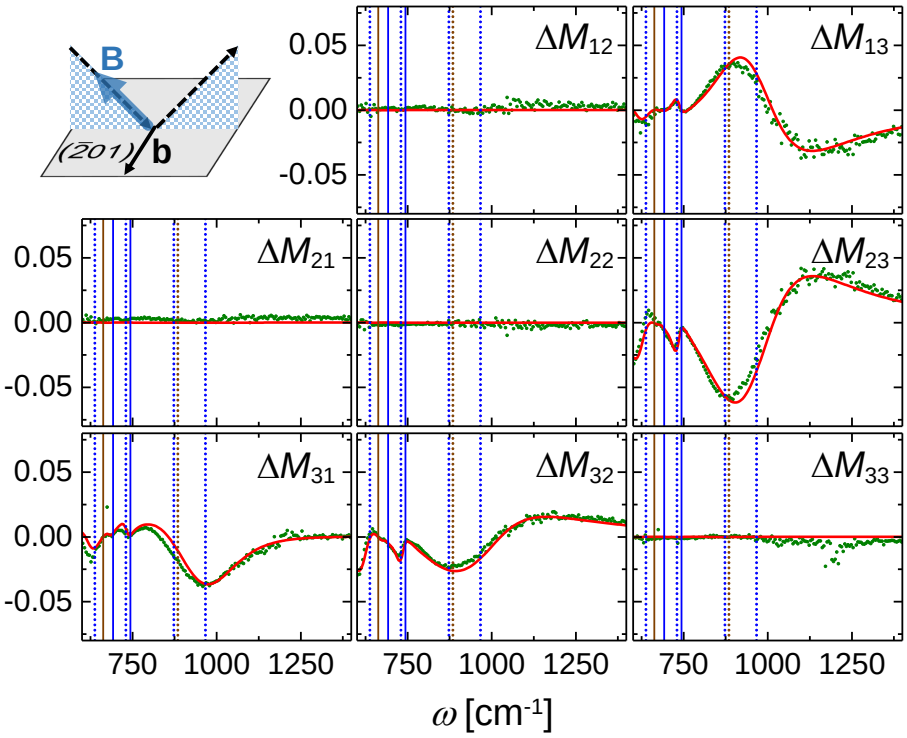

Figure 3.2: Same as Fig. 3.1 for the ($\bar{2}$01) cut β-Ga_2O_3 sample at azimuth angle $\phi = 181.7^{\circ}$.

Due to the coupling of longitudinal optical phonon modes and free charge carriers, the so called longitudinal phonon plasmon (LPP) modes are now experimentally observed. Since the spectral locations of the reflectance minima are governed by the LPP modes, the strongest MIR-OHE signatures occur in the vicinity of the highest frequency LPP modes, which are indicated by the vertical dotted lines in Fig. 3.1 and Fig. 3.2.[83] The unique shape of the signal is governed by changes in the dielectric function tensor due to phonon modes near this spectral range. We note that until this report, MIR-OHE difference data between positive and negative magnetic field were only seen in the off-block-diagonal Mueller matrix elements (i.e. M_{13}, M_{23}, M_{31}, M_{32}).[87] However, for the (010) surface (Fig. 3.1) a small difference is seen in the on-block-diagonal ele-

Table 3.1: Results for isotropic average free charge carrier properties in β-Ga_2O_3. The theoretical Gau-PBE average effective mass parameter is calculated by taking the harmonic mean of the predicted values along the **a**, **b**, and **c** crystal axes, which can be found in Table 3.2. Error bars shown correspond to the 90% confidence interval within the best-match model data analysis.

Method	Parameter	Value
MIR-OHE for (010) surface[a]	m^*	$(0.284 \pm 0.013)m_0$
	N	$(4.2 \pm 0.1) \times 10^{18}$ cm^{-3}
	μ	(44 ± 2) cm^2/Vs
MIR-OHE for ($\bar{2}01$) surface[a]	m^*	$(0.283 \pm 0.011)m_0$
	N	$(5.9 \pm 0.1) \times 10^{18}$ cm^{-3}
	μ	(43 ± 1) cm^2/Vs
Gau-PBE[b]	m^*_{avg}	$0.267m_0$

[a]This work
[b]Theory, Ref. 68

ments (i.e. M_{12}, M_{21}, M_{22}, M_{33}). This is due to the dielectric function tensor for the (010) surface at azimuth angle ϕ = 112.5° possessing non-zero off-diagonal elements at $|\mathbf{B}| = 0$. In contrast, the ($\bar{2}01$) surface at azimuth angle ϕ = 181.7° possesses negligible off-diagonal tensor components at $|\mathbf{B}| = 0$ since the **a**-**c** plane lies within the plane of incidence.

Assuming separate sets of isotropic free charge carrier properties for the (010) and ($\bar{2}01$) surfaces, the model parameters are fit to the MIR-OHE difference data and zero magnetic field data simultaneously. The final best-match model fit is presented in Fig. 3.1 and Fig. 3.2, and the resulting parameters are shown in Table 3.1. The zero magnetic field data alone would allow one to determine the isotropic plasma frequency ω_p and broadening γ, which are functions of m^*, N, and μ. The addition of the MIR-OHE data in the analysis allows m^*, N, and μ to be accurately resolved. In order to improve the best match between model calculated and experimental data, the model for the (010) and

($\bar{2}01$) surfaces must be assigned independent sets of free charge carrier properties to account for a potentially different Sn dopant distribution and activation. However, each surface shares the same phonon mode parameters and ε_∞. Since the phonon mode parameters and ε_∞ in Ref. 83 were derived assuming identical Drude parameters for the (010) and ($\bar{2}01$) surfaces, these quantities were also included in the best-match model fit to properly determine the free charge carrier properties. The analysis confirms the expected n-type conductivity for each surface cut. The azimuth angle ϕ = 112.5° and ϕ = 181.7° for the (010) and ($\bar{2}01$) surface, respectively, are determined by applying the zero magnetic field model to the zero-field MIR-OHE measurement.

The electron effective mass parameters experimentally determined in this work are $m^* = (0.284 \pm 0.013)m_0$ for the (010) surface and $m^* = (0.283 \pm 0.011)m_0$ for the ($\bar{2}01$) surface. These fall within the broad range of values reported for various density functional theory calculations: (0.12 to 0.13)m_0,[66] (0.22 to 0.30)m_0,[68] (0.23 to 0.24)m_0,[67] (0.26 to 0.27)m_0,[63] (0.27 to 0.28)m_0,[69,70] (0.34)m_0,[71] and (0.39)m_0.[72] The best-match model parameter results for the isotropically averaged mobility parameter μ for the two surfaces compare well with values determined previously by electrical Hall effect measurements for samples with similar free electron densities.[74] Our best-match model parameter results for the electron density N are in excellent agreement with the nominal Sn density of 1.7×10^{18} cm^{-3} provided by the crystal manufacturer. The electron density obtained by electrical Hall effect measurements is approximately equal to the doped Sn density.

Ueda *et al.* estimated electron effective mass parameters $m_b^* = 0.5m_0$ to $1.0m_0$ and $m_c^* = 1.0m_0$ to $2.0m_0$ from optical transmission and electrical Hall effect measurements.[73] There is a rather large discrepancy between the effective mass

Table 3.2: Results for anisotropic free charge carrier properties in β-Ga_2O_3. Error bars shown correspond to the 90% confidence interval within the best-match model data analysis.

Method	Parameter	Value
MIR-OHE for (010) surface[a]	m^*_a	$(0.288 \pm 0.044)m_0$
	m^*_b	$(0.283 \pm 0.046)m_0$
	$m^*_{c^\star}$	$(0.286 \pm 0.044)m_0$
	N	$(4.1 \pm 0.3) \times 10^{18}$ cm^{-3}
	μ_a	(45 ± 4) cm^2/Vs
	μ_b	(42 ± 4) cm^2/Vs
	$\mu_{c^\star}$	(42 ± 3) cm^2/Vs
MIR-OHE for ($\bar{2}$01) surface[a]	m^*_a	$(0.295 \pm 0.039)m_0$
	m^*_b	$(0.276 \pm 0.037)m_0$
	$m^*_{c^\star}$	$(0.311 \pm 0.044)m_0$
	N	$(6.0 \pm 0.5) \times 10^{18}$ cm^{-3}
	μ_a	(44 ± 3) cm^2/Vs
	μ_b	(44 ± 3) cm^2/Vs
	$\mu_{c^\star}$	(41 ± 3) cm^2/Vs
Gau-PBE[b]	m^*_a	$0.224m_0$
	m^*_b	$0.301m_0$
	m^*_c	$0.291m_0$

[a]This work.
[b]Theory, Ref. 68.

parameters reported in this work and by Ueda *et al*. A critical discussion of the results by Ueda *et al.* was given by Parisini *et al.* suggesting revision of data analysis in Ref. 73.[88]

The anisotropy of m^* may be defined by considering the ratios (m^*_a/m^*_b) and $(m^*_b/m^*_{c^\star})$. These quantities are comparable to the squares of the ratios of the plasma frequencies determined by the orthogonal Drude model approximation, via $(\omega_{p,b}/\omega_{p,a})^2 = (m^*_a/m^*_b)$ and $(\omega_{p,c^\star}/\omega_{p,b})^2 = (m^*_b/m^*_{c^\star})$. The parameters $\omega_{p,a}$, $\omega_{p,b}$, and $\omega_{p,c^\star}$ are the plasma frequencies corresponding to the **a**, **b**, and **c*** directions, respectively. Information about the plasma

frequencies can be gathered without the use of magnetic fields. Generalized ellipsometry measurements at zero field and at multiple sample azimuth orientations, for both the (010) and ($\bar{2}$01) surfaces, were taken and subsequently analyzed simultaneously with the MIR-OHE data. This approach provided sufficient sensitivity to determine the anisotropy of the free charge carrier parameters. The resulting effective mass parameters are shown in Table 3.2. The ratios are $(m_a^*/m_b^*) = (1.02^{+0.38}_{-0.28})$ and $(m_b^*/m_{c^\star}^*) = (0.99^{+0.37}_{-0.27})$ for the (010) surface, where the upper and lower scripted numbers refer to the upper and lower uncertainty limit of the effective mass parameter ratio. The upper/lower limits come from taking the ratios within the maximum/minimum parameter deviations in the numerator and denominator using the mass parameters and error bars as shown in Table 3.2. For the ($\bar{2}$01) surface, the ratios are $(m_a^*/m_b^*) = (1.07^{+0.33}_{-0.25})$ and $(m_b^*/m_{c^\star}^*) = (0.89^{+0.29}_{-0.22})$. Our findings suggest a small deviation from isotropy, however, which is well within the uncertainty limits for both surfaces investigated. Nonetheless, the possibility of a small anisotropy would be consistent with recent theoretical investigations.[67,66,70,63] Yamaguchi calculated the electron effective mass ratios of $(m_{a'}^*/m_{b'}^*) = 0.96$ and $(m_{b'}^*/m_{c'}^*) = 1.07$ at the Γ point, where $m_{a'}^*$, $m_{b'}^*$, and $m_{c'}^*$ are diagonal Cartesian effective mass tensor components.[67] Furthmüller and Bechstedt predict ratios of $(m_{a'}^*/m_{b'}^*) = 1.01$ and $(m_{b'}^*/m_{c'}^*) = 1.03$.[63] He *et al.* finds ratios of $(m_{a^\star}^*/m_{b^\star}^*) = 0.95$ and $(m_{b^\star}^*/m_{c^\star}^*) = 1.05$.[66] Recent density functional calculations using the Gau-PBE approach predict ratios of $(m_a^*/m_b^*) = 0.74$ and $(m_b^*/m_c^*) = 1.03$ for undoped β-Ga_2O_3.[68] We note that the theoretical results reported so far are inconsistent, however, all theoretical predicted ratios could fall within our experimental error bars and no conclusive statement about a finite anisotropy of the effective electron mass parameter can be made at this

point. Within our uncertainty limits, the mobility parameter is found to be essentially isotropic. This is consistent with previous theoretical investigations for intrinsic mobility,[89] experimental Hall effect measurements using the bar method[90] and using the Van der Pauw method.[91,75] A nearly isotropic mobility is also reported for electron channel mobility in silicon-doped Ga_2O_3 metal-oxide-semiconductor field-effect transistors (MOSFETs).[92]

Electron effective mass values for monoclinic oxides similar to β-Ga_2O_3 have been calculated by density functional methods. Monoclinic θ-Al_2O_3, an isomorph of β-Ga_2O_3, is predicted to possess similar effective mass values and anisotropy. The values are calculated to be $0.41m_0$, $0.41m_0$, and $0.37m_0$ along the [100], [010], and [001] crystallographic directions, respectively.[93] The effective mass is virtually isotropic regardless of the structural complexity of the low symmetry monoclinic structure. In contrast, monoclinic transition metal oxides ZrO_2 and HfO_2 are predicted to have much higher effective masses and stronger anisotropy.[94] The predicted values for ZrO_2 are $3.1m_0$, $3.2m_0$, and $3.7m_0$ along the $\mathbf{x}'$, $\mathbf{y}'$, and $\mathbf{z}'$, respectively, where $\mathbf{z}'$ is analogous to $\mathbf{c}^\star$. The predicted values for HfO_2 are $8.2m_0$, $1.6m_0$, and $1.0m_0$ along the same respective directions.

3.6 Acknowledgements

This work was supported by the Swedish Research Council (VR) under Grant No. 2013-5580 and 2016-00889, the Swedish Governmental Agency for Innovation Systems (VINNOVA) under the VINNMER international qualification program, Grant No. 2011-03486, the Swedish Government Strategic Research Area in Materials Science on Functional Materials at Linköping University, Faculty

Grant SFO Mat LiU No 2009 00971, and the Swedish Foundation for Strategic Research (SSF), under Grant Nos. FL12-0181 and RIF14-055. The authors further acknowledge financial support by the University of Nebraska-Lincoln, the J. A. Woollam Co., Inc., the J. A. Woollam Foundation and the National Science Foundation (awards MRSEC DMR 1420645, CMMI 1337856 and EAR 1521428).

Chapter 4

Electromagnon excitation in cupric oxide measured by Fabry-Pérot enhanced terahertz Mueller matrix ellipsometry

4.1 Abstract

Here we present the use of Fabry-Pérot enhanced terahertz (THz) Mueller matrix ellipsometry to measure an electromagnon excitation in monoclinic cupric oxide (CuO). As a magnetically induced ferroelectric multiferroic, CuO exhibits coupling between electric and magnetic order. This gives rise to special quasiparticle excitations at THz frequencies called electromagnons. In order to measure the electromagnons in CuO, we exploit single-crystal CuO as a THz Fabry-Pérot cavity to resonantly enhance the excitation's signature. This enhancement technique enables the complex index of refraction to be extracted. We observe a peak in the absorption coefficient near 0.705 THz and 215 K, which corresponds to the electromagnon excitation. This absorption peak is observed along only one major polarizability axis in the monoclinic **a**-**c** plane. We show the excitation can be represented using the Lorentz oscillator model, and discuss how these Lorentz parameters evolve with temperature. Our findings are in excellent agreement with previous characterizations by THz time-domain spectroscopy (THz-TDS), which demonstrates the validity of this enhancement

4.2 Introduction

Multiferroic materials are usually defined as materials which exhibit more than one type of ferroic order, for example ferroelectricity and ferromagnetism[95,96,97]. This valuable characteristic allows for the implementation of electrical switching of magnetic order, or magnetic switching of electrical order, and which is of interest for potential device applications. One excellent material candidate is cupric oxide (CuO), where ferroelectricity is induced by antiferromagnetic order, i.e., CuO is an induced-multiferroic material[98]. This characteristic gives rise to a special quasiparticle excitation called the electromagnon. In contrast to a magnon (a spin wave driven by the *magnetic* field of an electromagnetic wave), an electromagnon is a spin wave driven by the *electric* field of an electromagnetic wave[99]. Electromagnons could provide a means to advance the field of magnonics, in which spin waves are used for information processing[100,101,102,103]. Previously, electromagnons have been identified at low temperatures (< 70 K) in multiferroic rare-earth manganites ($RMnO_3$ and RMn_2O_5)[99,104,105,106,107], and $TbFeO_3$[108]. However, in CuO electromagnons are seen at relatively higher temperatures (213 K to 230 K)[109]. To progress towards room temperature multiferroic devices which utilize electromagnons, it is important to investigate materials such as CuO[110].

Electromagnons in CuO have been previously characterized by THz time-domain spectroscopy (THz-TDS)[109,111,112,113]. Reference[109] provides a detailed report of the measurement and analysis of this excitation. In Ref. 109, THz-TDS

is used to measure the optical absorption, α, of CuO as a function of temperature (200 K to room temperature) and frequency (0.2 THz to 2 THz). When the electric field of the THz beam is parallel to [101] crystal direction, the authors observed a distinct peak in the change of the absorption coefficient $\Delta\alpha$ near 0.73 THz and 214 K. This absorption peak corresponds to the electromagnon excitation.

In general, THz-TDS provides information about the electric field amplitude and phase after interaction with the sample, and therefore allows one to determine the complex-valued refractive index, $\tilde{n}$. THz Mueller matrix ellipsometry is an alternative approach to access $\tilde{n}$ in the THz spectral range[5,114,115,116,117]. Ellipsometry is a technique which measures the change in the polarization of light after interaction with a sample[6,7]. An ellipsometric measurement provides information about the relative amplitude and relative phase shift between *s*- and *p*-polarized light, and therefore also grants access to $\tilde{n}$. Since ellipsometry measures relative changes in amplitude and phase, it has the advantage of not depending on the source intensity. The THz ellipsometer system used in this work is described in Ref. 5. This THz source generates a monochromatic THz beam, in contrast to white-light THz pulses used in THz-TDS. Employing monochromatic THz sources has the benefit of a more direct measurement that does not require an additional step of Fourier-type transforms.

When the THz wavelength ($\lambda \approx 1$ mm) is comparable to the substrate thickness, and when the coherence length of the THz light source is exceeding the substrate thickness by at least one order of magnitude, spectrally-sharp, resonant Fabry-Pérot interference features can be present in the spectrum of samples deposited onto THz-transparent substrates. This is due to the interference from multiple reflections off the internal front and back interfaces of

the substrate. When measured by THz Mueller matrix ellipsometry, these features can be used sensitively to determine the properties of two-dimensional electron gases (2DEGs), for example[118,11,119,13]. In this work, we exploit bulk single-crystal CuO itself as a THz Fabry-Pérot cavity to enhance the sensitivity to small changes in $\tilde{n}$ as a function of the substrate temperature. A previous report has also demonstrated the use of THz Mueller matrix ellipsometry to identify an electromagnon in $TbMnO_3$[120]. However, this was accomplished by measuring a single reflection off a bulk single-crystal, and not by exploiting the Fabry-Pérot enhancement technique described here. For our experimental parameters, a single reflection of the CuO surface would only offer very limited sensitivity to $\tilde{n}$. Our enhancement technique allows accurate characterization of CuO as a function of frequency and temperature in order to observe its electromagnon excitation. We also discuss the application of the Lorentz oscillator model to fit the excitation, and report how these model parameters evolve with temperature. We compare our results with previous investigations by THz-TDS and find excellent agreement.

4.3 Results and Discussion

4.3.1 Experimental approach

An illustration of the measurement approach used here is shown in panels (a) and (b) of Fig. 4.1. A thin wafer of single-crystal (010) CuO is exploited as a THz Fabry-Pérot cavity to enhance the electromagnon's optical signature. The enhancement is caused by interferences between multiple reflections off the front and backside interfaces, as seen in Fig. 4.1. To measure these interferences as a function of temperature and frequency, we employ THz Mueller matrix

ellipsometry which provides information about the change in polarization after reflection off the CuO. The measured Mueller matrix data contain very unique features caused by the Fabry-Pérot interferences. These features are very sensitive to changes in $\tilde{n}$, which enables the characterization of the electromagnon.

4.3.2 Optical model approach

The optical model used here consists of a nominally 0.7 mm thick layer of bulk single-crystal CuO with plane parallel interfaces, as shown in Fig. 4.1. The frequency and temperature dependent optical response of CuO is governed by $\tilde{n}(\omega, T)$ which is dependent on the complex permittivity (i.e. dielectric function) $\tilde{\epsilon}(\omega, T)$ and complex permeability $\tilde{\mu}(\omega, T)$ through the equation $\tilde{n}(\omega, T) = \sqrt{\tilde{\epsilon}(\omega, T)\tilde{\mu}(\omega, T)}$. As determined in Ref. 109, we assume $\tilde{\mu}(\omega, T) = 1$ for the temperature and frequency range investigated here. The dominant contributions to $\tilde{n}(\omega, T)$ in this range are due to either electromagnons or phonons, both of which behave as electric dipoles, and therefore are represented by $\tilde{\epsilon}(\omega, T)$. Although CuO is a monoclinic crystal, we find the orthorhombic approximation sufficient to fit the measured THz data. For this approximation, we place the three orthogonal major polarizability axes along the $[10\bar{1}]$, [101], and [010] crystal directions. This approach was also used by the authors in Ref. 109 to analyze their THz-TDS data. Note for monoclinic crystals, the direction of the pseudo-orthorhombic major polarizability axes (or dielectric axes) can vary with frequency in the **a-c** plane[121]. The directions of these major polarizability axes are not related to the **a** and **c** crystallographic directions, but are determined by the sum of all dipole-like resonances polarized in the **a-c** plane that contribute to $\tilde{\epsilon}$ (or in general $\tilde{n}$)[122]. The major polarizability directions can be experimentally determined by placing an (010) surface cut crystal between

two polarizers which are crossed at 90° (such that the **a-c** plane is parallel to the surface of the polarizers), rotating the crystal, and observing the intensity minimums[121,111]. As demonstrated in Ref. 111, these axes in CuO fall near the $[10\bar{1}]$ and [101] crystal directions at THz frequencies. The diagonal Cartesian dielectric tensor used for the orthorhombic approximation is

$$\tilde{\epsilon} = \begin{pmatrix} \tilde{\epsilon}_{xx} & 0 & 0 \\ 0 & \tilde{\epsilon}_{yy} & 0 \\ 0 & 0 & \tilde{\epsilon}_{zz} \end{pmatrix}, \tag{4.1}$$

where the tensor elements $\tilde{\epsilon}_{xx}$, $\tilde{\epsilon}_{yy}$, and $\tilde{\epsilon}_{zz}$, are the permittivities along the major polarizability axes $[10\bar{1}]$, [101], and [010], respectively. The schematics in Fig. 4.1(a) and 4.1(b) include the Cartesian directions **x** and **y**, the major polarizability directions $[10\bar{1}]$ and [101], and the plane of incidence. The [010] and **z** directions are omitted for clarity. The direction **x** is contained within the sample surface plane and oriented along the propagation direction of incident light. The directions **x**, **y**, and **z** are fixed to the THz ellipsometer, while the major polarizability axes (and therefore the CuO crystal) are rotated during the experiment. For the (010) surface cut CuO investigated here, azimuth angle $\phi = 0°$ is defined as **+x** aligned along $[10\bar{1}]$. A positive ϕ corresponds to a rotation of the major polarizability axes in the **a-c** plane in the **+x** to **+y** direction.

4.3.3 Fabry-Pérot enhanced THz Mueller matrix data

Shown in Fig. 4.1 is the change in the acquired Mueller matrix elements as a function of temperature at a single frequency ($\nu = 0.715$ THz). Data is measured at 205 K, 210 K, 212 K, 213 K, 214 K, 215 K, 217 K, 220 K, 225 K, and 230 K. The Fabry-Pérot enhanced experimental data (green open circles with

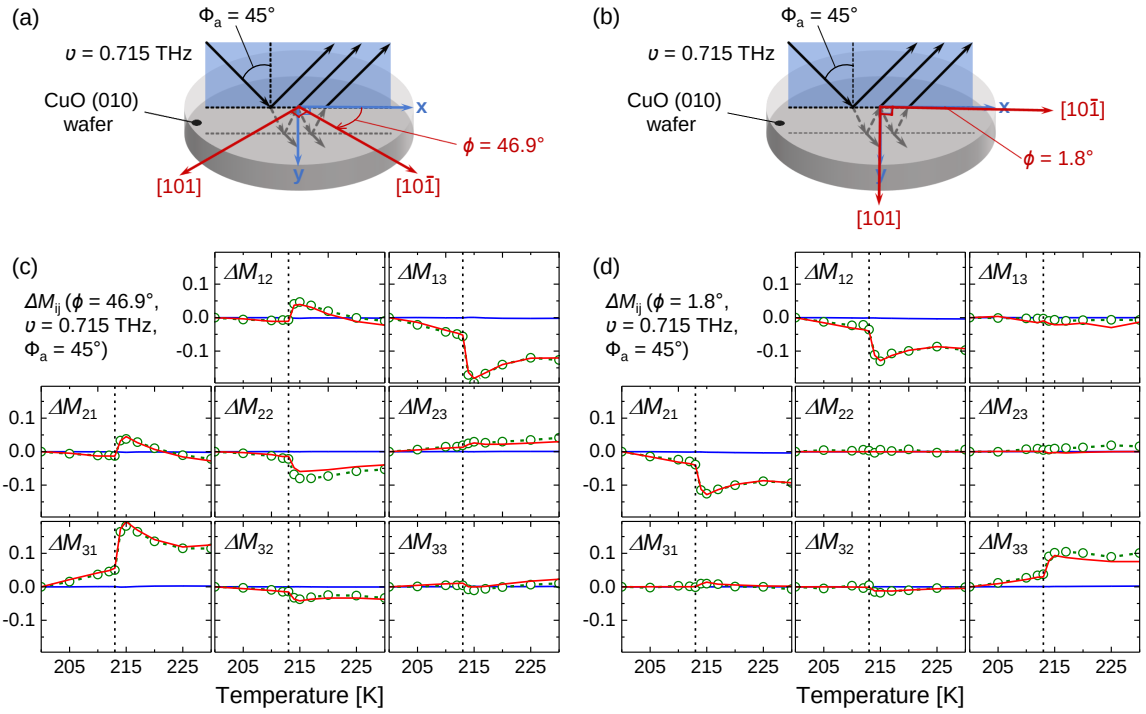

Figure 4.1: Change in the normalized Mueller matrix elements ($\Delta M_{ij} = M_{ij}(T)$ - $M_{ij}(T$=200 K)) for single-crystal CuO as a function of temperature at frequency $\nu = 0.715$ THz and at angle of incidence $\Phi_a = 45°$. Experiment (open green circles with dotted lines) and best-match model calculated data (red solid lines) are for the Fabry-Pérot enhanced case, in which multiple reflections off the backside of the CuO crystal are included. To demonstrate the extent of the enhancement, simulated non-enhanced data are shown (blue solid lines) where only the first reflection off the CuO surface is considered. Panels (c) and (d) show data for two different azimuth orientations ($\phi = 46.9°$ and $\phi = 1.8°$, respectively) of the investigated (010) surface cut. Shown in panels (a) and (b) are illustrations of the THz beam's multiple reflections at the front and backside interfaces for each measured azimuth orientation (not to scale). The vertical dashed lines mark the AF1 ($<$ 213 K) to AF2 (213 K to 230 K) phase transition, where CuO becomes an induced-multiferroic in the AF2 phase. This characteristic of the AF2 phase gives rise to the electromagnon excitation.

dotted lines) and best-match model calculated data (red solid lines) show significant changes as a function of temperature due to the variation in $\tilde{\epsilon}$. The largest change in the data is seen between 213 K and 214 K where the CuO transitions from antiferromagnetic (AF1 phase: $<$ 213 K) to a magnetically induced fer-

roelectric multiferroic (AF2 phase: 213 K to 230 K). This substantial change in the Mueller matrix is caused by a change in $\tilde{\epsilon}$ due to the appearance of the electromagnon absorption in the AF2 phase. To demonstrate the magnitude of the Fabry-Pérot enhancement, simulated data for no enhancement effect (blue solid lines) are included in Fig. 4.1. This non-enhanced data is for the case of an infinitely thick CuO crystal, where no reflections off the backside are considered. The $\tilde{\epsilon}(T)$ used to generate the non-enhanced data is determined from the Fabry-Pérot enhanced data analysis. This analysis will be discussed in detail further below. The non-enhanced data is nearly zero for all temperatures. This shows the Fabry-Pérot enhancement technique is crucial for obtaining $\tilde{\epsilon}$ in our experiment.

Two different azimuth orientations of the (010) CuO are measured in our experiments, as illustrated in Fig. 4.1(a) and 4.1(b). Figure 4.1(c) shows data for azimuth angle $\phi = 46.9^\circ$, and Fig. 4.1(d) shows $\phi = 1.8^\circ$. For $\phi = 46.9^\circ$, the major polarizability axes in the **a-c** plane ($[10\bar{1}]$ and $[101]$) have been rotated to near the midpoint between the **x** and **y** axes (Fig. 4.1(a)). Since the CuO is anisotropic within the **a-c** plane, the $\phi = 46.9^\circ$ orientation exhibits large *p*-to-*s* and *s*-to-*p* light mode conversion. This mode conversion is quantified by the off-block-diagonal Mueller matrix elements (M_{13}, M_{23}, M_{31}, and M_{32}). In contrast, the off-block-diagonal elements for $\phi = 1.8^\circ$ are minimal, because the major polarizability axes are near the **x** and **y** axes (Fig. 4.1(b)).

Shown in Fig. 4.2 is the Fabry-Pérot enhanced Mueller matrix spectra for a single temperature (215 K). Data is measured in increments of 0.005 THz in the available frequency ranges. The minimums in the simulated total reflectivity (M_{11}) are shown in Fig. 4.2 as vertical dotted lines to demonstrate the reflectivity is related to the Mueller matrix. In Fig. 4.2, panels (a) and (b) show data for

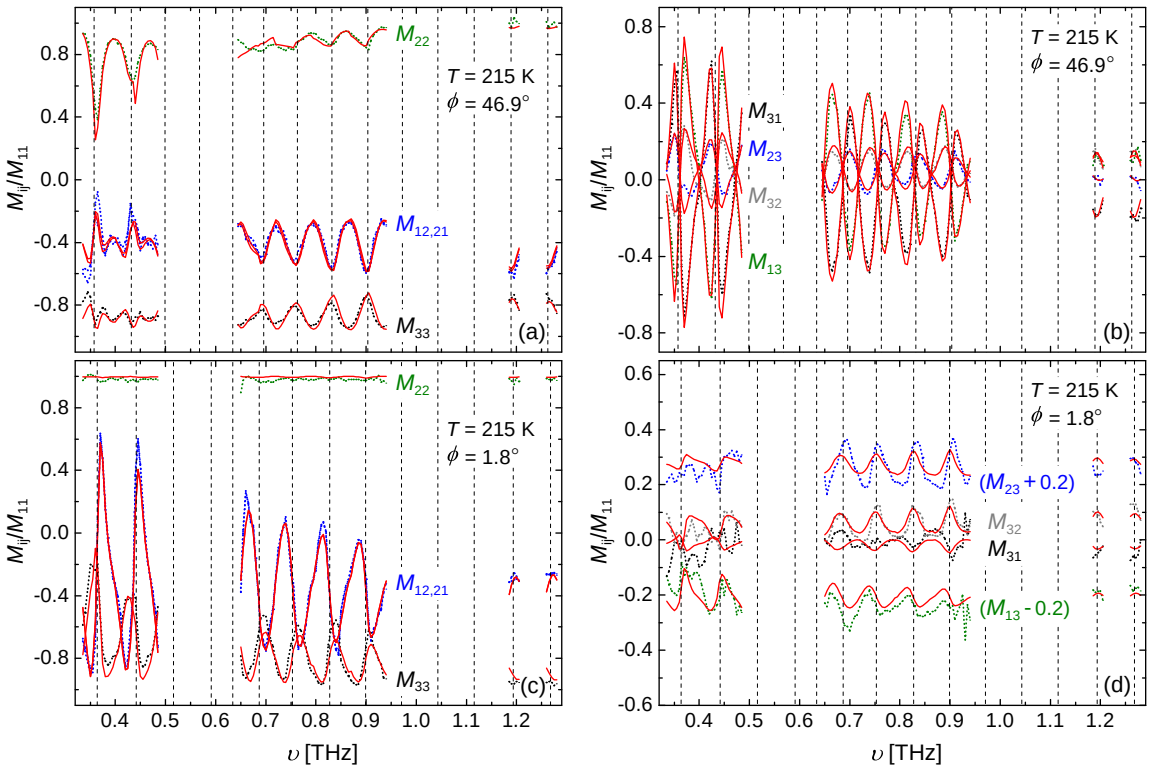

Figure 4.2: Experimental (broken lines) and best-match model calculated (red solid lines) Fabry-Pérot enhanced Mueller matrix spectra for single-crystal CuO at 215 K and angle of incidence $\Phi_a = 45°$. Panels (a) and (b) show data from the azimuth orientation $\phi = 46.9°$ measurement, and panels (c) and (d) show data for the $\phi = 1.8°$ measurement. The acquired on-block-diagonal Mueller matrix elements (M_{12}, M_{21}, M_{22}, and M_{33}) are shown in panels (a) and (c), and the off-block-diagonal elements (M_{13}, M_{23}, M_{31}, and M_{32}) are shown in panels (b) and (d). Vertical dashed lines indicate the total reflectivity (i.e. M_{11}) minima for the respective azimuth orientations.

the $\phi = 46.9°$ orientation, and panels (c) and (d) show data for $\phi = 1.8°$. Here, the Mueller matrix elements are separated into on-block-diagonal (left two panels: (a) and (c)) and off-block-diagonals (right two panels: (b) and (d)). As previously mentioned for Fig. 4.1, due to the orientation of the major polarizability axes in the **a-c** plane the $\phi = 46.9°$ orientation shows sizable off-block-diagonals, whereas $\phi = 1.8°$ are minimal. The sharp oscillating features in Fig. 4.2 are due to Fabry-Pérot interferences, which are highly sensitive to $\tilde{\epsilon}$, ϕ, and CuO thick-

ness. The number of oscillations in the spectrum is dependent on $\tilde{\epsilon}$ and CuO thickness. Increasing the CuO thickness causes the number of oscillations to increase, and decreasing the thickness causes the number to decrease. For the CuO sample investigated here, the maximum sensitivity to $\tilde{\epsilon}$ occurs near the reflection minimum of each oscillation. Therefore, a large number of oscillations is desirable to achieve increased sensitivity at as many points in the spectrum as possible. For our experiment, we find a nominal CuO thickness of 0.7 mm is optimal.

4.3.4 Best-match model analysis results

Shown in Fig. 4.3 are the results of the best-match model analysis of the Fabry-Pérot enhanced data. The analysis is performed by employing the method described in the **Optical model approach** section. To determine $\tilde{\epsilon}$ independently for each point in the (ω, T) array, the Mueller matrix data (M_{ij}) and Mueller matrix difference-data ($\Delta M_{ij} = M_{ij}(T) - M_{ij}(T = 200\ \text{K})$) for all measured temperatures and frequencies are analyzed simultaneously. With respect to frequency, multiple data points are grouped together and assigned the same value for $\tilde{\epsilon}$ in the analysis. The bounds for these sections in units of THz are: 0.360, 0.402, 0.438, 0.600, 0.687, 0.720, 0.755, 0.794, 0.830, 0.866, 0.902, and 1.17. This creates 13 independent piecewise sections for which all frequencies in one section have a constant value. We refer to this analysis as the piecewise constant fit approach. The values chosen for the bounds are the Mueller matrix zero-crossings seen in Fig. 4.2(b). With respect to temperature, all 10 increments are assigned independent values of $\tilde{\epsilon}$. This piecewise constant fit approach creates a two-dimensional array of values for $\tilde{\epsilon}$ (13 piecewise sections with respect to frequency $\times$ 10 points with respect to temperature). The analysis reveals no

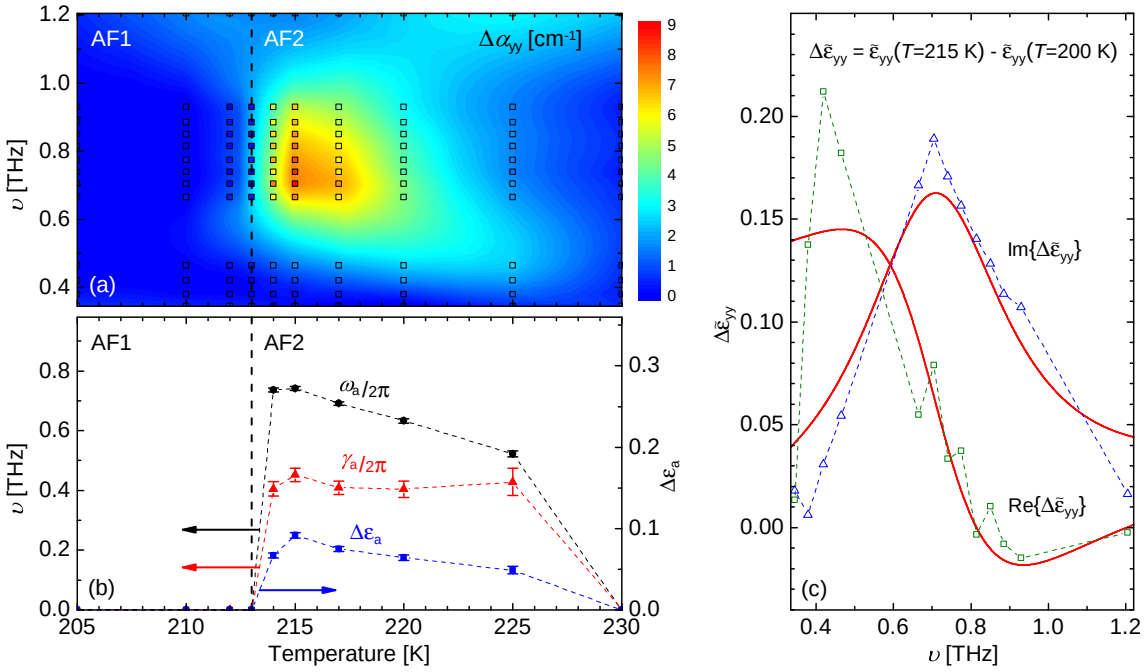

Figure 4.3: Results of the best-match model analysis. Panel (a) shows a false color map of the difference in absorption coefficient ($\Delta\alpha_{yy} = \alpha_{yy}(T)$ - $\alpha_{yy}(T$=200 K)) along the [101] major polarizability direction as a function of temperature and frequency. The peak in $\Delta\alpha_{yy}$ near 0.705 THz and 215 K corresponds to the electromagnon excitation. Colored square symbols indicate all individual data points from the piecewise constant fit. On the same color scale is a smoothed contour plot to guide the reader's eye. The dashed line marks the AF1 to AF2 phase transition. Panel (b) shows parameters from the Lorentz oscillator analysis (solid symbols) as a function of temperature. Panel (c) shows an example Lorentz oscillator fit (red solid lines) to the piecewise constant fit values (open symbols) for $\Delta\tilde{\epsilon}_{yy}$ at 215 K.

features of interest in $\tilde{\epsilon}_{xx}(\omega, T)$. Due to limited sensitivity in the **z** direction, we set $\tilde{\epsilon}_{zz}(\omega, T)$ to a constant value in the analysis (see **Methods** for further details). However, for $\tilde{\epsilon}_{yy}(\omega, T)$, a distinct peak in the absorption coefficient, $\alpha_{yy} = 2\frac{\omega}{c} Im\{\sqrt{\tilde{\epsilon}_{yy}}\}$, is seen, and which corresponds to the electromagnon excitation. Figure 4.3(a) shows a false color map of the difference in the absorption coefficient $\Delta\alpha_{yy}$ along the [101] direction ($\Delta\alpha_{yy} = \alpha_{yy}(T) - \alpha_{yy}(T = 200$ K)). The peak seen near 0.705 THz and 215 K corresponds to the electromagnon exci-

tation. A sharp increase in $\Delta\alpha_{yy}$ is observed from 213 K to 214 K due to the sudden appearance of the electromagnon in the AF2 phase.

Since electromagnons primarily behave as electric dipoles, the Lorentz oscillator has been used to model their optical response[109,120]. The electromagnon excitation in CuO has been previously modeled by using the sum of two Lorentz oscillators[109]

$$\begin{aligned}\Delta\tilde{\epsilon}_{yy}(\omega,T) &= \tilde{\epsilon}_{yy}(\omega,T) - \tilde{\epsilon}_{yy}(\omega,T=200\text{ K}) \\ &= \frac{\Delta\epsilon_a\cdot\omega_a^2}{\omega_a^2-\omega^2-i\omega\gamma_a} + \frac{\Delta\epsilon_b\cdot\omega_b^2}{\omega_b^2-\omega^2-i\omega\gamma_b},\end{aligned} \tag{4.2}$$

where $\Delta\epsilon_{a,b}$, $\omega_{a,b}$, and $\gamma_{a,b}$ are the amplitude, center frequency, and broadening parameters for each mode, respectively. This model is fit to the *change* in the dielectric function $\Delta\tilde{\epsilon}_{yy}$ relative to 200 K in an attempt to isolate the electromagnon and lessen the contributions from phonon modes[109]. Mode *a* is the main electromagnon mode, and mode *b* is a broad low-amplitude shoulder mode to the electromagnon. We fit the mode *a* parameters in Eqn. 4.2 to the values of $\Delta\tilde{\epsilon}_{yy}(\omega,T)$ from the piecewise constant fit to obtain the Lorentz oscillator parameters as a function of temperature. Due to the limits of our available spectral range, the mode *b* parameters were fixed to values determined in Ref. 109 ($\Delta\epsilon_b$ = 0.012, $\omega_b/2\pi$ = 1.23 THz, and $\gamma_b/2\pi$ = 2.2 THz). Although the mode *b* parameters change with temperature, we hold them constant for all temperatures, as an approximation. Our analysis reveals this approximation does not significantly affect the results. Figure 4.3(b) shows the results of the Lorentz oscillator model analysis for the main electromagnon mode *a*. The $\Delta\epsilon_a$ and ω_a parameters show similar trends of a dramatic increase from 213 K to 214 K followed by a gradual decrease to zero. Note, $\omega_a(T)$ does not

exactly coincide with maximum for $\Delta\alpha_{yy}(T)$, because γ_a is comparable to ω_a. The γ_a parameter seems to follow a similar trend until 220 K and 225 K. Since the absorption peak is beginning to move outside the available spectral range at 220 K, it is more difficult to determine γ_a, which is reflected in the larger error bars for the 220 K and 225 K data points. These results are in excellent agreement with the parameters provided in Ref. 109 where the Lorentz model is fit to only $\Delta\alpha_{yy}$, instead both the real and imaginary parts of $\Delta\tilde{\epsilon}_{yy}$ as in this work. Shown in Fig. 4.3(c) is an example of the Lorentz oscillator best-match model fit to the piecewise constant fit values for $\Delta\tilde{\epsilon}_{yy}(\omega, T = 215\text{ K})$. We note electromagnons can also contribute to the magnetoelectric tensors (i.e., gryotropic tensors, or cross tensors), which enable dynamic electric influence of magnetic polarization, and dynamic magnetic influence of electric polarization[120]. For example, Ref. 120 discusses the characterization of an electromagnon in single-crystal $TbMnO_3$ in which a small contribution to one of the magnetoelectric tensors is modeled using a Lorentz oscillator. In general, it is possible to use the Mueller matrix to differentiate contributions in $\tilde{\boldsymbol{\epsilon}}$, $\tilde{\boldsymbol{\mu}}$, and the magnetoelectric tensors[123,120]. However for CuO, a more rigorous analysis is needed considering its complex monoclinic nature.

4.4 Conclusion

A Fabry-Pérot enhanced terahertz (THz) Mueller matrix ellipsometry approach was used to determine the electromagnon excitation in monoclinic cupric oxide (CuO). A single-crystal CuO cut with parallel interfaces was exploited as a THz Fabry-Pérot cavity to resonantly enhance the excitation's signature. This enhancement technique enables the complex index of refraction to be ex-

tracted. We observe a peak in the absorption coefficient near 0.705 THz and 215 K, which corresponds to the electromagnon excitation. Our findings are in excellent agreement with previous characterizations by THz time-domain spectroscopy (THz-TDS). We propose the use of the THz enhancement technique to detect small absorption changes in anisotropic crystals caused by subtle excitations such as electromagnons.

4.5 Methods

4.5.1 Experimental setup and procedure

The THz ellipsometer sub-system described in Ref. 5 is used to measure bulk single-crystal CuO as a function of temperature and frequency. The THz ellipsometer operates in the polarizer-sample-rotating-analyzer configuration which allows access to the upper-left 3×3 block of the complete 4×4 Mueller matrix. All Mueller matrix data shown here has been normalized to the M_{11} element. The THz source is a backward wave oscillator (BWO) equipped with GaAs Schottky diode frequency multipliers. The detector is a liquid helium cooled bolometer. The magneto-cryostat sub-system is used to cool the sample, but no magnetic field is applied at any point during the experiment. Inside the cryostat, the sample was always measured starting from the lowest temperature (200 K) up to the highest temperature (297 K).

4.5.2 Sample growth

One disk-like wafer (nominally 8 mm in diameter and 0.7 mm thick) of single-crystal (010) CuO was grown using the optical float zone method[124]. Polycrystalline cylindrical feed rods were prepared using high purity (99.995%) CuO

starting chemical and sintered at 900° C for three days under oxygen flow. Single-crystal was grown using a four mirror optical floating-zone furnace under 9 bar oxygen pressure[124]. The growth was carried out using a sintered feed rod at a growth rate of 3.5 mm/h with feed and seed rods counter-rotating at 30 rpm. One cylindrical disk of (010) single-crystal was cut from the large as-grown crystal for these experiments.

4.5.3 Room temperature THz analysis

At room temperature outside the cryostat, Fabry-Pérot enhanced THz Mueller matrix data were taken to determine the unknown sample parameters: CuO wafer thickness, and θ (rotation of the major polarizability axes about the $[10\bar{1}]$ direction). Considering only one angle of incidence is available when measuring through the cryostat ($\Phi_a = 45°$), these parameters must be obtained outside the cryostat. These measurements were performed at multiple angles of incidence ($\Phi_a = 40°$, 50°, and 60°), at four azimuth orientations (nominally $\phi = 0°$, 45°, 90°, and 135°), and in the frequency range of 0.65 THz to 0.9 THz in increments of 0.005 THz. All the data is analyzed simultaneously to find the CuO thickness is (0.669 ± 0.003) mm, and $\theta = (5.2 \pm 0.6)°$. Change in the CuO thickness with temperature is set in the optical model according to expansion coefficients reported in Ref. 125. θ is fixed in the analysis for all temperatures as it does not depend on ϕ, temperature, or any other experimental variables. Values of ϕ for each azimuth orientation measured through the cryostat are determined by applying the optical model for outside the cryostat. The values for ϕ when the sample is mounted in the cryostat are found to be $\phi = (46.9 \pm 0.5)°$ and $\phi = (1.8 \pm 0.6)°$.

Analysis of data measured outside the cryostat also allows the room tem-

perature $\tilde{\epsilon}$ to be extracted. At room temperature CuO exhibits minimal dispersion from 0.65 THz to 0.9 THz[109], therefore we assume constant values for $\tilde{\epsilon}$ in this range. We find the tensor elements of $\tilde{\epsilon}$ near 0.775 THz are: $\tilde{\epsilon}_{xx} = (10.56 \pm 0.09) + i(0.31 \pm 0.01)$, $\tilde{\epsilon}_{yy} = (9.64 \pm 0.08) + i(0.17 \pm 0.01)$, and $\tilde{\epsilon}_{zz} = (11.94 \pm 0.12) + i(0.33 \pm 0.09)$. These results are in excellent agreement with values reported in Ref. 109. This analysis confirms the validity of our orthorhombic approximation described in the **Optical model approach** section. Due to limited sensitivity in the **z** direction for data taken through the cryostat, we fix $\tilde{\epsilon}_{zz}$ to $(11.94 + i0.33)$ for all temperature dependent measurements.

4.6 Acknowledgements

This work was supported in part by the National Science Foundation under award DMR 1808715, by Air Force Office of Scientific Research under award FA9550-18-1-0360, and by the Nebraska Materials Research Science and Engineering Center under award DMR 1420645. M. S. acknowledges the University of Nebraska Foundation and the J. A. Woollam Foundation for financial support. The authors would like to thank James Lloyd-Hughes, Connor Mosley, and Tino Hofmann for the helpful suggestions and conversations.

Chapter 5

Cavity-enhanced optical Hall effect in two-dimensional free charge carrier gases detected at terahertz frequencies

5.1 Abstract

The effect of a tunable, externally coupled Fabry-Pérot cavity to resonantly enhance the optical Hall effect signatures at terahertz frequencies produced by a traditional Drude-like two-dimensional electron gas is shown and discussed in this communication. As a result, the detection of optical Hall effect signatures at conveniently obtainable magnetic fields, for example by neodymium permanent magnets, is demonstrated. An AlInN/GaN-based high electron mobility transistor structure grown on a sapphire substrate is used for the experiment. The optical Hall effect signatures and their dispersions, which are governed by the frequency and the reflectance minima and maxima of the externally coupled Fabry-Pérot cavity, are presented and discussed. Tuning the externally coupled Fabry-Pérot cavity strongly modifies the optical Hall effect signatures, which provides a new degree of freedom for optical Hall effect experiments in addition to frequency, angle of incidence and magnetic field direction and strength.

5.2 Introduction

The optical Hall effect (OHE) in semiconductor layer structures is the occurrence of magneto-optic birefringence detected in response to incident electromagnetic radiation, caused by movement of free charge carriers under the magnetic field-induced influence of the Lorentz force[126]. In general, this birefringence leads to polarization mode coupling which is conveniently detected by generalized ellipsometry at oblique angle of incidence and at terahertz (THz) frequencies, for example. THz-OHE has recently been demonstrated as non-contact and therefore valuable tool for the investigation of free charge carrier properties in semiconductor heterostructures[5,127,118,128,129,130,131,132]. The OHE discussed in this work is not to be confused with the "polarization-dependent Hall effect of light", described for example in Refs.[133,134]. Previous instrumental approaches, discussed more detailed in Refs.[132,5], rely on high magnetic fields provided either by conventional, water-cooled or superconducting, liquid He-cooled electromagnets resulting in comparably large and costly experimental setups. In general, OHE configurations capable of detecting signals at low and conveniently obtainable magnetic fields are desirable. The use of small magnetic fields for THz magneto-optic measurements was demonstrated recently by Ino *et al.* for bulk-like InAs[135]. Due to low effective mass and high electron concentration, the low field still yielded large enough signals for detection. The signal-to-noise separations of the OHE signatures depend on many factors, the

most important are low effective mass, high mobility and high carrier density, but also crucial is the thickness of the physical layer that contains the charge carriers. The OHE signals are defined by and presented here as the differences between the off-diagonal Mueller matrix elements determined for opposing magnetic field directions[5]. The amplitude of the OHE signals is proportional to the percentage of cross-polarization at the given frequency[131,136] and is caused only by the Drude-like magneto-optic contribution of the two-dimensional electron gas (2DEG). Note, the off-diagonal Mueller matrix difference spectra are expected to be zero if there is no external magnetic field. These signals, in first approximation, scale linearly with the magnetic field amplitude. Hence, the first approach to detect OHE signatures in samples with very thin layers, or low-mobile, heavy-mass and low-density charge carriers where the OHE signatures are weak is to increase the magnetic field amplitude.

In this communication, we demonstrate and exploit the enhancement of the OHE signal obtained from samples with plane parallel interfaces deposited on THz transparent substrates using an external and tunable optical cavity. We show that an OHE signal enhancement of up to one order of magnitude can be achieved by optimizing the cavity geometry, which is very useful for small magnetic field strengths. This signal enhancement allows the determination of free charge carrier effective mass, mobility, and density parameters using OHE measurements at low magnetic fields. An AlInN/GaN-based high electron mobility transistor structure (HEMT) grown on a sapphire substrate is investigated as an example, while the cavity enhancement phenomenon discussed here is generally applicable to situations when a layered sample is deposited onto a transparent substrate. This cavity enhancement may be exploited in particular for layered samples grown on technologically relevant low-doped or

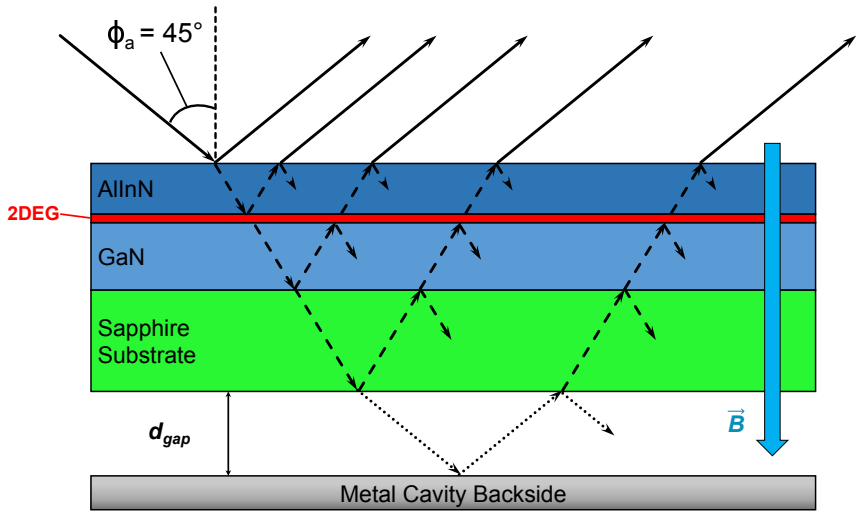

Figure 5.1: Schematic drawing of the beam path through the sample and the external optical cavity, shown for example for an AlInN/GaN/sapphire high electron mobility transistor (HEMT) structure with two-dimensional electron gas (2DEG). The sapphire substrate and metallic cavity surface are parallel and separated by the distance d_{gap}. Here, the magnetic field **B** is perpendicular to the sample surface with the positive magnetic field direction oriented into the sample. The metal cavity backside may be formed by an appropriately surface-coated permanent magnet. Note that HEMT layer structure, substrate and cavity are not to scale.

semi-insulating substrate materials such as SiC, Si, or GaAs, etc.

5.3 Theory

For a thin-film layer stack deposited on a transparent substrate, where the substrate thickness is much larger than the combined layer thickness of all sublayers in the stack, and where the substrate thickness may be multiple orders of the wavelength at which the OHE signatures are detected, the fraction of the incident beam transmitted through the entire sample is coupled back into the substrate using an external cavity. For example, a highly reflective surface placed at a distance d_{gap} behind and parallel to the backside of the substrate,

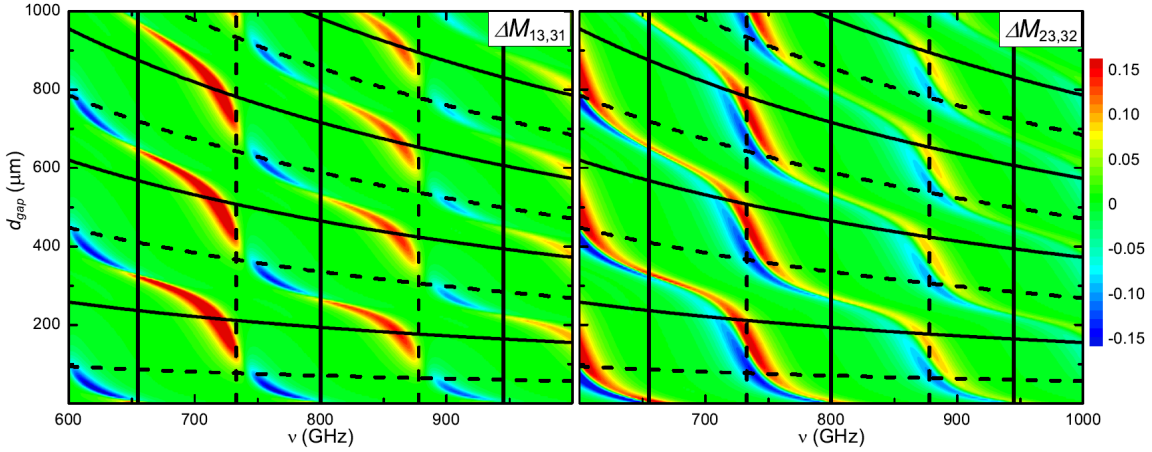

Figure 5.2: Model-calculated contour plots of typical THz-OHE data, here for example $\Delta M_{13,31}$ = $M_{13,31}(+B)$ - $M_{13,31}(-B)$ and $\Delta M_{23,32}$ = $M_{23,32}(+B)$ - $M_{23,32}(-B)$ for the AlInN/GaN HEMT sample are shown as a function of frequency and d_{gap}. The vertical solid and dashed black lines indicate the sample's *s*-polarized reflection maxima and minima, respectively. The *s*-polarized reflectivity maxima and minima of the external cavity and which depend on d_{gap}, are shown as horizontal solid and dashed black lines, respectively. All data was calculated for an angle of incidence Φ_a=45° and a magnetic field magnitude of $|B|$=0.55 T. Note that the *p*-polarized modes occur indistinguishably close to the *s*-polarized modes and are omitted for clarity.

as shown in Fig. 5.1, permits THz radiation to be coupled back into the sample and thereby produce an enhancement of the OHE signal. The enhancement is due to the positive interference of wave components traveling back and forth within the coupled cavity-substrate while undergoing polarization conversion upon passing the magneto-optic birefringent 2DEG multiple times. Thereby, the amount of polarization converted light increases and which gives rise in the measured off-diagonal Mueller matrix elements. In our example discussed below we have achieved up to one order of magnitude enhancement by varying d_{gap}.

Figure 5.2, shows model-calculated contour plots of the THz-OHE signal (difference of the Mueller matrix elements calculated for $B = 0.55$ T and $B =$

-0.55 T) illustrating the enhancement phenomenon. The structure used for the calculation is a AlInN/GaN HEMT structure deposited on a 350 μm thick c-plane Al_2O_3 substrate, similar to the HEMT structure discussed in Ref. 130. The non-trivial off-block Mueller matrix components $\Delta M_{13,31}$ and $\Delta M_{23,32}$ show periodic resonances which depend on the frequency of the THz probe beam ν and d_{gap}. The frequency is varied over the range from 600 to 1000 GHz and the d_{gap} ranges from 0 to 1000 μm to obtain overview over an experimentally feasible parameter range and to gain insight into the multiplicity of the occurrences of coupled-substrate-cavity mode enhancements of the OHE signal.

In order to show that these occurrences are related to the minima in reflectance for the substrate and cavity modes, the maxima (minima) of the s-polarized reflectivity of the sample and the cavity are plotted as solid (dashed), vertical and horizontal lines, respectively. The signatures follow a commonly observed anti-band crossing behavior, where the bands of the substrate reflectance minima couple with the OHE bands and induce strongest changes with frequency and cavity thickness. The resonance frequency of the sample Fabry-Pérot mode is determined by the sample's substrate thickness which is much larger than the total HEMT thickness (see further below). The p-polarized modes which occur indistinguishably close to the s-polarized modes are omitted for clarity in Fig. 5.2.

It is interesting to note, that there are regions in frequency and d_{gap} where the OHE signal is very small or vanishes. Hence, experimental configurations where both frequency and d_{gap} can be varied over sufficiently large regions, that is, to cover at least one period of coupled substrate-cavity modes will be valuable for practical applications.

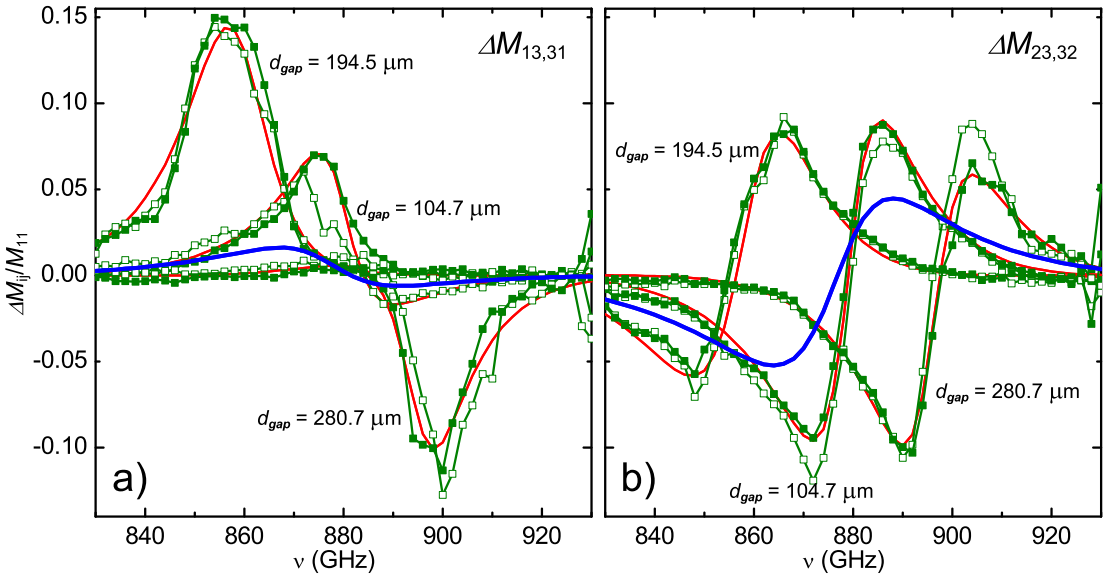

Figure 5.3: The panels a) and b) show the corresponding experimental (green lines) and best-model calculated (red solid lines) data $\Delta M_{13,31}$ and $\Delta M_{23,32}$ at three different d_{gap} values. The $\Delta M_{13}(\Delta M_{23})$ and $\Delta M_{31}(\Delta M_{32})$ spectra are shown as open and closed data points respectively. The panels a) and b) also include best-model calculated data for $d_{\mathrm{gap}} \rightarrow \infty$ as blue solid lines for comparison.

5.4 Experiment

For the experimental verification of this enhancement effect an AlInN/GaN-based HEMT structure was grown using metal-organic vapor phase epitaxy on a single side polished *c*-plane sapphire substrate with a nominal thickness of 350 μm. Subsequent to the growth of a 2 μm thick undoped GaN buffer layer, a 1 nm thick AlN spacer layer was deposited, followed by a 12.3 nm thick $Al_{0.82}In_{0.18}N$ top layer[137]. The THz-OHE data presented here were obtained using a custom-built THz ellipsometer[138,5]. THz-OHE data were measured in the spectral range from 830 to 930 GHz with a resolution of 2 GHz at an angle of incidence $\Phi_a = 45°$ and for three different gap distances d_{gap} of 104.7 μm, 194.5 μm, and 280.7 μm.

The measurements were facilitated by mounting the HEMT structure onto a Ni-coated, high-grade N42 neodymium permanent magnet using adhesive spacers to create a homogeneous air gap between the Ni-coated surface of the magnet which serves as the metallic cavity backside and the HEMT structure. The THz Mueller matrix measurements were carried out with the sample mounted on the north and on the south pole-face of the permanent magnet to obtain THz-OHE data (differences of the Mueller matrix elements M_{13}, M_{23}, M_{31}, and M_{32} measured at opposing magnetic fields). Across the sample area illuminated by the THz probe beam, the magnetic field strength provided by the permanent magnet was $B = (0.55 \pm 0.005)$ T. For values of d_{gap} used here, the change in the magnetic field magnitude at different gap values is negligible at the sample position.

In addition to the THz-OHE measurements, the sample as well as the metal magnet surfaces were investigated using a commercial (J.A. Woollam Co. Inc.) mid-infrared (MIR) ellipsometer in the spectral range from 300 to 1200 cm^{-1} at $\Phi_a = 60^\circ$ and 70° in order to determine the HEMT layer thickness parameters and phonon mode parameters, and the optical constants of the magnet surface metal layer (Ni). All measurements were carried out at room temperature and analyzed simultaneously. The experimental and model calculated data are reported using the Mueller matrix formalism[6].

5.5 Results and Discussion

The experimental MIR-SE and THz-OHE data sets were analyzed simultaneously using an optical model composed of eight phases including a AlInN top layer/2DEG/AlN spacer/GaN buffer/Al_2O_3 substrate/air gap/Ni cavity sur-

face[130]. Nonlinear regression methods where used to match the lineshape of experimental and optical model calculated data as close as possible by varying relevant model parameters using parameterized model dielectric functions[6]. The THz and MIR dielectric function tensors of the optically uniaxial sample constituents GaN, AlInN, AlN and Al_2O_3 are composed of contributions from optically active phonon modes $\varepsilon^{L}(\omega)$ and free-charge carrier excitations $\varepsilon^{FC}(\omega)$. Details on the parametrization approach are omitted here for brevity and we refer to previous publications[126,136,131,139,140]. The optical response of the magnet's Ni mirror surface that forms the external cavity is described using the classical Drude formalism using the static resistivity parameter of $\rho = (1.72 \pm 0.49) \times 10^{-5}$ Ωcm and the average-collision time parameter of $\tau = 6.15 \times 10^{-16}$ s. ρ is obtained as best-match model parameter from MIR-SE data analysis, and is within typical values for Ni[141,142]. The average-collision time parameter is taken from Ref. 141 and not varied in the model analysis.

Fig. 5.3 shows experimental (green lines) and best-model calculated (red solid lines) THz-OHE spectra (differences of the Mueller matrix elements M_{13}, M_{23}, M_{31}, and M_{32}) measured at $B = 0.55$ T and -0.55 T. For this sample structure and the perpendicular magnetic field orientation, the magnetic-field-induced changes in the Mueller matrix elements $M_{13}(M_{23})$ equal those in $M_{31}(M_{32})$. For comparison, best-model calculated data for $d_{gap} \rightarrow \infty$ is shown as blue solid lines. Based on the best-model analysis the low background free charge carrier densities of the AlInN, GaN, and AlN layers were found to have a negligible contribution to the THz-OHE signal. We find a good agreement between experimental and best-model calculated data for the different d_{gap} values.

The maxima and minima depicted in Fig. 5.3 are due to the coupling of the Fabry-Pérot oscillations in the sample structure with those of the external cav-

ity. The experimentally accessed range in frequency and d_{gap} was selected to sufficiently cover the response of the HEMT sample-substrate-cavity mode under the influence of a small magnetic field to detect the enhanced OHE signal. Depending on the distance d_{gap} between sample backside and cavity surface the frequency dependent response of the OHE signal changes where extrema occur in the vicinity of the intersection of the sample and cavity reflection extrema. Comparing $\Delta M_{13,31}$ and $\Delta M_{23,32}$ reveals distinct differences. Whereas $\Delta M_{23,32}$ shows a derivative-like shape with a single pair of maximum and minimum in the range from 830 to 930 GHz, $\Delta M_{13,31}$ exhibits a single maximum or minimum and a strong amplitude variation, depending on d_{gap}. The largest amplitude is observed for $d_{\mathrm{gap}} = 194.5$ μm where $\Delta M_{13,31}$ is approximately 0.15. The smallest change is observed for $d_{\mathrm{gap}} = 104.7$ μm where $\Delta M_{13,31} \approx 0.07$. The best-model calculated data excluding the cavity enhancement shown as solid blue line in Fig. 5.3 a) is almost vanishing and the cavity enhances the OHE signal by one order of magnitude. The largest amplitudes of $\Delta M_{23,32} \approx 0.1$ can be observed for $d_{\mathrm{gap}} = 104.7$ μm and 280.7 μm (Fig. 5.3 b). The largest amplitudes in $\Delta M_{23,32}$ without the cavity effect is approximately 0.05 which is a factor of two smaller than the OHE signal amplitude observed for $d_{\mathrm{gap}} = 104.7$ μm and 280.7 μm.

The best-model sheet density, mobility, and effective mass obtained for the 2DEG are $N = (1.02 \pm 0.15) \times 10^{13}$ cm^{-2}, $\mu = (1417 \pm 97)$ cm^2/Vs, $m^* = (0.244 \pm 0.020) m_0$, respectively. These results are in good agreement with the results of high-field ($B = 7$ T) THz-OHE measurements on the same sample $N = (1.40 \pm 0.07) \times 10^{13}$ cm^{-2}, $\mu = (1230 \pm 36)$ cm^2/Vs, $m^* = (0.258 \pm 0.005)\ m_0$. Excellent agreement between THz-OHE and electrical measurement results were reported previously on similar samples[130]. The OHE response measured

at multiple frequencies and multiple d_{gap} values provides sufficient information to determine the Drude model parameters independently. We find in our numerical data analysis that N, μ, and m^* are uncorrelated parameters. Ideally the polaronic effects on the effective mass need to be considered. However, as discussed in Ref. 143, these corrections have been found negligible for GaN and are not considered in our present analysis. Note, that increasing the number of data sets obtained at different cavity lengths into the numerical data analysis reduces the error bars on the 2DEG parameter set. Our findings demonstrate that the cavity enhancement of the THz-OHE signal allows the investigation of free charge carrier properties of two dimensional free charge carrier gases at low magnetic fields which may be conveniently provided by permanent magnets.

A variation in d_{gap} provides a new degree of freedom to tune the experimental conditions so as to reach a maximum response for a given frequency range. According to Fig. 5.2, other gap lengths, e.g., 150 μm will provide even larger signals in this situation. For a given sample system the experimental configuration can be optimized by calculating the coupled substrate-cavity modes and then selecting frequency range and d_{gap} accordingly. Furthermore, varying the d_{gap} at a fixed frequency may be used to maximize the OHE signal.

5.6 Acknowledgements

J.A. Woollam Foundation; National Science Foundation (DMR-1420645, EPS-1004094); Swedish Agency for Innovation Systems (2011-03486, 2014-04712); Swedish Foundation for Strategic Research (FFL12-0181); Swedish Research Council (2013-5580).

Chapter 6

In-situ terahertz optical Hall effect measurements of ambient effects on free charge carrier properties of epitaxial graphene

6.1 Abstract

Unraveling the doping-related charge carrier scattering mechanisms in two-dimensional materials such as graphene is vital for limiting parasitic electrical conductivity losses in future electronic applications. While electric field doping is well understood, assessment of mobility and density as a function of chemical doping remained a challenge thus far. In this work, we investigate the effects of cyclically exposing epitaxial graphene to controlled inert gases and ambient humidity conditions, while measuring the Lorentz force-induced birefringence in graphene at Terahertz frequencies in magnetic fields. This technique, previously identified as the optical analogue of the electrical Hall effect, permits here measurement of charge carrier type, density, and mobility in epitaxial graphene on silicon-face silicon carbide. We observe a distinct, nearly linear relationship between mobility and electron charge density, similar to field-effect induced changes measured in electrical Hall bar devices previously. The observed doping process is completely reversible and independent of the type of inert gas exposure. (This article is licensed under a Creative Commons Attribu-

6.2 Introduction

Two dimensional materials are a new class of materials that attracted significant interest due to their unique electronic, optical, and mechanical properties. Many properties differ dramatically from the bulk substances. Examples include silicene, molybdenum disulfide, hexagonal boron nitride, and graphene[144,145,146,2]. These materials have wide spread applications such as high-frequency electronics, sensing elements, mechanically durable and lightweight materials, medicine, energy storage, and more. Common to all two dimensional materials is their extremely large surface to volume ratio, which make them very susceptible to substrate and ambient gas adsorption effects. Graphene, one of the most studied two dimensional materials, has been shown to substantially change in its properties as a function of substrate, substrate polarity, and ambient media (gases, liquids)[147,148,149,150,151,152,153]. Ambient induced doping is observed for many types of graphene, for instance epitaxial graphene on SiC[147,148,149], exfoliated graphene on SiO_2[150], and types of chemical vapor deposition (CVD) grown graphene[151]. However, the effect of ambient doping on the free charge carrier mobility is rarely explored, mostly due to the lack of experimental techniques capable of independently assessing carrier density and mobility without further modifying graphene. For instance standard electrical Hall effect measurements require contacts and Hall bar fabrication, which involve multiple processing steps that may modify graphene properties. In this work, ambient effects on the free charge carrier density and mobility of epitaxial graphene grown by Si-sublimation on the Si-face (0001) of 4H-SiC is studied

as an example.[154]

This type of graphene typically exhibits n-type conductivity due to a complex interaction with the Si-face SiC substrates via the buffer layer[155,156]. The intrinsic electron doping of pristine monolayer epitaxial graphene on Si-face SiC was found to be on the order of 10^{13} cm^{-2}.[148] The polarity of the Si-face SiC also gives rise to high hydrophilicity, which is relatively unchanged with addition of a graphene monolayer[157]. Similar to other two dimensional materials, graphene's properties are also extremely sensitive to adsorbed gas molecules[147,148,158,149,159]. Previous studies of the electrical properties of epitaxial graphene on SiC as a function of the ambient conditions employ contact-based techniques or Kelvin probe approaches and typically do not report changes in N_s and μ simultaneously. For example, the authors in Ref. 147 use a 4-point probe device to perform resistance and thermo-electric power measurements during various phases of gas exposure and annealing cycles. Ref. 148 reports on characterization using a Hall bar device and Scanning Kelvin Probe Microscopy (SKPM), and which do not provide changes in N_s and μ simultaneously. In order to fully understand the ambient doping and scattering mechanisms in epitaxial graphene, accurate information on the free charge carrier parameters as a function of the ambient conditions is required. Here we report on the first *in-situ*, contactless determination of the majority free charge carrier type, N_s, and μ using terahertz-frequency optical Hall effect measurements (THz-OHE)[11,119,5]. We expose a monolayer graphene sample to various gases and report the results of the best-match model data analysis from optical Hall effect measurements. Along with N_s and μ, the THz-OHE signal allows us to determine the majority free charge carrier type (electrons). This is important information since the majority carrier type of epitaxial graphene on Si-face SiC

can vary from sample to sample[160,158,129]. We find that exposure to ambient causes significant changes in the free charge carrier properties sheet carrier concentration N_s and mobility μ for epitaxial graphene on SiC.

6.3 Results and Discussion

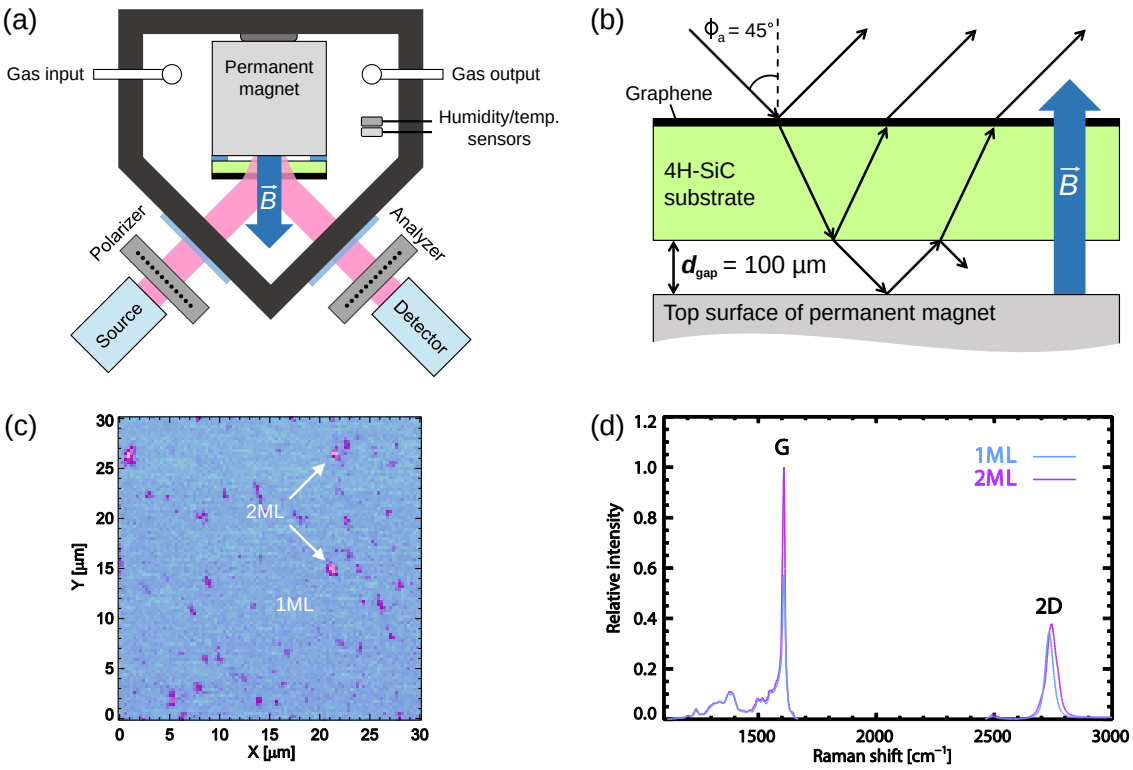

Figure 6.1: (a) Schematic of single-layer epitaxial graphene on SiC substrate located on top of a permanent magnet within a sealed gas chamber with optical ports for polarized THz radiation, and THz ellipsometer setup. (b) Schematic of the cavity-enhancement of the THz optical Hall effect using a resonant cavity between the sample and magnet surface. (c) Representative micro-reflectance map of the graphene surface. (d) Representative micro-Raman spectrum of 1ML and 2ML sample areas.

Figure 6.1a details a conceptual drawing of the sample arrangement within the gas flow cell. Ellipsometric data are measured at oblique incidence as a

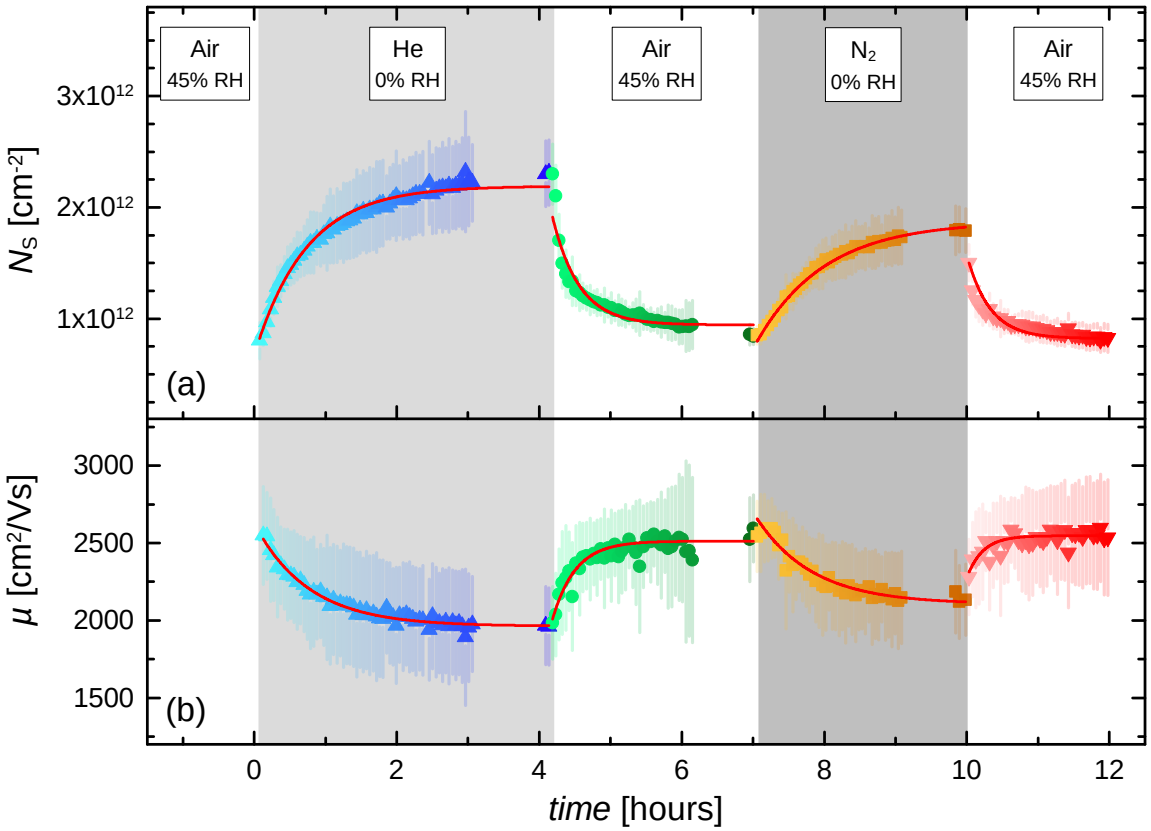

Figure 6.2: Best-match model results for sheet carrier density N_s and mobility μ as a function of time. The shaded regions correspond to exposure to different types of gas at various relative humidities (RH). The flow rate of 0.5 liters/minute at normal pressure is constant for all exposure phases. Error bars for the best-match model parameters are shown here for each data point as vertical lines. Solid lines depict single-process exponential decay functions, for which rate constants and equilibrium parameters are given in the text.

function of time for various gas exposure phases. Figure 6.1b depicts the scheme of the optical Hall effect arrangement, where an external cavity is added. The cavity significantly enhances the optical Hall effect in two-dimensional charge carrier densities[11]. The sample investigated here consists of 99% monolayer (ML) graphene and 1% bilayer (BL) inclusions as illustrated in a representative microscopic reflectance-converted-thickness map in Fig. 6.1c. Reflectivity and low-energy electron microscopy mapping, and scan lines confirm the thickness

homogeniety of the epitaxial graphene sample over the entire surface area of 10 mm$\times$10 mm. A representative micro-Raman spectrum for 1ML and 2ML sample areas is shown in Fig. 6.1d. See the Methods section for further details on the experimental setup.

6.3.1 *In-situ* optical Hall effect gas exposure monitoring

Figure 6.2 shows the *in-situ* optical Hall effect best-match model results for sheet carrier density N_s and mobility μ as a function of gas exposure for the ML graphene sample. After growth, the sample was exposed to normal ambient conditions (air measured with relative humidity (RH) of 45%) for approximately 15 minutes, and then mounted in the gas flow cell. During the experiment, large dynamic changes in N_s and μ are observed when changing the gas type. It can be seen that nitrogen and helium exposure (both 0% RH) increases N_s while ambient exposure (45% RH) decreases N_s. This behavior is consistent with previous results on epitaxial graphene on SiC[148,158]. The change in N_s from air exposure can be explained by a redox reaction at the surface of the graphene involving various environmental gases, which results in electron withdrawal[147]. Exposure to an inert gas, such as nitrogen or helium, is thought to cause the doping agents at the graphene surface to desorb, which reverses the electron withdrawal.

The prolonged exposure of single-layer graphene to inert gases drastically changes N_s and μ. We observe an approximate single process exponential decay with mean life time τ for both quantities, where the exposure to helium results in faster changes ($\tau_{He} \approx 45$ min) than the exposure to nitrogen ($\tau_{N_2} \approx 50$ min). The exposure to air results in electron reduction at a rate ($\tau_{Air} \approx 20$ min) faster than the observed changes during the exposure to the inert gases. We esti-

mate the equilibrium electron density ($N_{s,\infty}$) and mobility ($\mu_{s,\infty}$) parameters for infinite exposure time of helium, nitrogen, and air as 2.2×10^{12} cm^{-2} and 1960 cm^2/Vs, 1.9×10^{12} cm^{-2} and 2100 cm^2/Vs, and 8.8×10^{11} cm^{-2} and 2530 cm^2/Vs, respectively. There is a noticeable difference in $N_{s,\infty}$ and $\mu_{s,\infty}$ for He and N_2 exposure. The cause of this difference is unknown at this point. The difference may be explained by more effective impurity desorption from He compared to N_2, or in different modifications of the graphene-SiC interaction.

One possible scenario for the explanation of the time evolution of the results shown in Fig. 6.2 is an ambient acceptor doping redox reaction at the graphene surface involving O_2, H_2O, and CO_2[147]. To summarize this previously proposed mechanism, first thin films of water form at surfaces when exposed to ambient. These films contain dissolved CO_2, which reacts with water causing an excess of H^+. O_2 dissolved in the water film reacts with H^+ and electrons borrowed from the graphene and forms additional water molecules, thereby chemically acceptor doping the graphene. While this reaction may not be the only possible chemical process, it is described as the most dominant[161]. In principle, it is also possible that the observed changes in N_s and μ may be related to a modification of the Van der Waals interaction between Si-C and C-C at the SiC-graphene interface. However, exposure to ambient and different inert gases of bare SiC substrate and a sample containing only a buffer layer grown at the same conditions as the epitaxial graphene show no change in the THz-OHE signals. We also note that both SiC substrate and the buffer sample do not produce any free charge carrier related response.

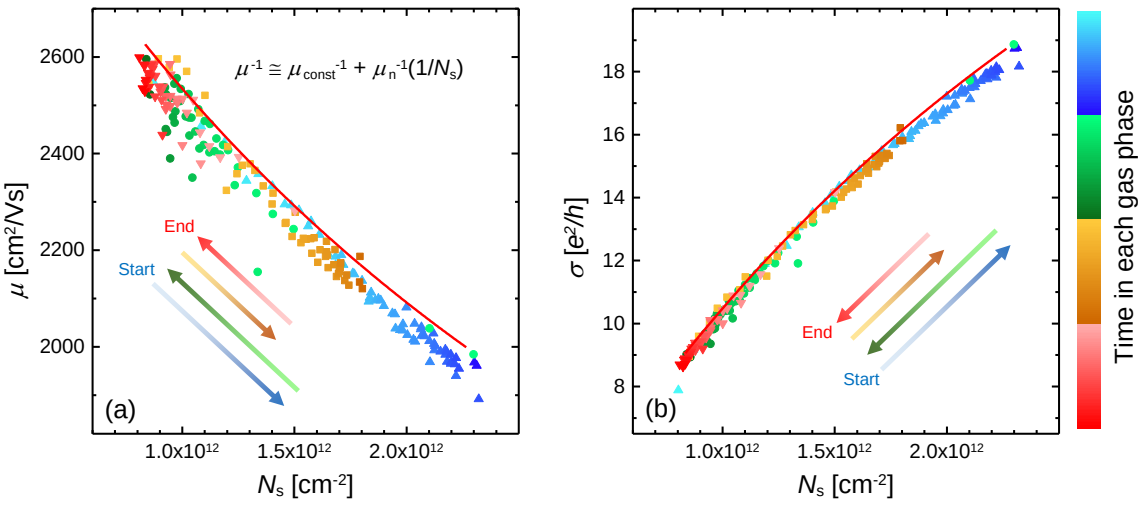

Figure 6.3: Panel (a) shows mobility μ versus sheet density N_s for all data in Fig. 6.2. Panel (b) shows conductivity σ versus N_s, where σ is expressed in quantum units (e^2/h). Red lines show the best-match model fit for $\mu(N_s)$. Arrows indicate directions of time evolution. Colors and symbols identify phases of gas exposure as in Fig. 6.2.

6.3.2 Mobility and conductivity dependence on carrier density

In order to investigate the free charge carrier scattering mechanisms, which are affected by the observed chemical acceptor doping of graphene, μ and conductivity σ are plotted as a function of N_s in Fig. 6.3. Figure 6.3a shows the results in Fig. 6.2 as μ versus N_s. Figure 6.3b depicts the results from Fig. 6.2 now as σ versus N_s, where $\sigma = N_s e\mu$ and e is the electron charge[162]. Interestingly, the same nearly linear dependence of μ versus N_s with time is observed regardless of the type of gas exposure. Since different scattering mechanisms produce different functional dependencies of mobility versus density, one might anticipate that exposure to different gases would result in different traces of μ versus N_s. However, the observed common traces for He and N_2 suggest that the scattering mechanisms which cause variations in μ are similar. The common traces for

inert and ambient gases seem to suggest that inert gases reverse the scattering mechanism influence from air exposure.

In an attempt to apply a model for μ as a function of N_s, Matthiessen's rule is applied to combine a constant mobility contribution μ_{const} and an N_s-dependent contribution $\mu_n \sim 1/N_s$ (Fig. 6.3a)[163,164]. This model approach has been used, in part, by Tanabe *et al.*[165] to describe electrical Hall effect results for μ versus N_s, where N_s is varied by electric field-effect doping. In Tanabe *et al.*, μ_{const} represents a constant contribution from charged impurity (long range) scattering, and μ_n represents the N_s-dependent point (short range) scattering contribution[165]. In contrast with our work, the ambient conditions were not varied in the experiments performed by Tanabe *et al.*. Therefore, our experiment may include different contributions to charge carrier scattering and further experimentation is needed to determine the exact source of mobility limitation. Furthermore, the fabricated Hall bars and electrodes in Tanabe *et al.* may introduce additional contributions to carrier scattering compared to our virgin sample. In Tanabe *et al.*, the number of charged impurities is likely not to vary throughout the experiment, unlike this work in which impurities can be introduced by gases. Our observation suggests that it is possible only the carrier density in the graphene changes as a result of gas exposure and where the observed change in mobility is only given by the $\mu(N_s)$ dependence. This would also provide a possible explanation why both $\mu(N_s)$ and $\sigma(N_s)$ (Fig. 3(a) and 3(b)) show so little dependence on the gas species. A variation in number of charged impurities during our experiment could also explain the change in μ, if number of charged impurities is proportional to N_s[166,167,168,162,169,170,171]. Other possibilities for the observed μ change include acoustic phonon scattering[172], or even gas-induced modifications to interactions between graphene,

buffer layer, or SiC substrate. The best-match model parameters for $\mu(N_s)$ are $\mu_{const} = (3214 \pm 35)$ cm^2/Vs and $a = (1.20 \pm 0.03) \times 10^{16}$ (Vs)$^{-1}$, where a is the proportionality constant in $\mu_n = a/N_s$ clearly describe all observed data points. Note that parameter a does not necessarily correspond to any specific scattering mechanism, but is reported here to describe the observed relationship.

Recent electrical Hall bar experiments on very similar epitaxial graphene also show a linear μ versus N_s dependence[173]. In the report by Yager *et al.*, many Hall bar devices were fabricated and investigated on primarily 1ML graphene. In contrast to our work, the variation in N_s reported by Yager *et al.* is a result of variation of small 2ML coverage inside certain devices. In Ref. 173 it is noted that one would never know why the results are so inconsistent, unless microscopic images of the devices are inspected and variations in 2ML coverage are detected. One advantage of the THz-OHE, and ellipsometry in general, is the ability to acquire an average response over the entire sample. This eliminates parameter variations associated with fabricating devices to obtain consistent values of N_s, μ, and carrier type.

6.4 Conclusions

In summary, we have obtained N_s and μ of epitaxial graphene as a function of gas exposure using the cavity-enhanced *in-situ* THz-OHE, which allows contactless determination of these properties. In addition to the free charge carrier properties, the THz-OHE allows access to the majority carrier type, which is determined to be electrons. The results of the best-match model analysis reveal important information about the ambient doping and scattering mechanisms for epitaxial graphene on Si-face (0001) 4H-SiC. In agreement with previous

works[148,147], it is found that exposure to an inert gas, such as helium or nitrogen, reverses the electron withdrawal caused by ambient. The change in N_s and μ as a function of gas exposure can be approximated by a single process exponential decay function. The results indicate epitaxial graphene on Si-face SiC could take longer than one day to reach its final ambient state. This is important to consider when studying graphene recently exposed to ambient, since its properties may differ from day to day.

The observed μ versus N_s dependence is universal for all phases of gas exposure. This suggests inert gases reverse the scattering mechanism influence caused by air exposure. When a model is applied for μ as function of N_s, we find one constant and one $\sim 1/N_s$ term is needed to describe the dependence. This suggests that it is possible only the carrier density in the graphene changes as a result of gas exposure and where the observed change in mobility is only given by the $\mu(N_s)$ dependence. This scenario also provides explanation for the observed universality of $\mu(N_s)$ and $\sigma(N_s)$ dependencies on the gas species. However, further investigation is needed to distinguish the exact mechanisms which control and limit μ. The experiments performed here demonstrate the ability of the *in-situ* THz-OHE to obtain N_s, μ, and majority carrier type with a high time resolution which is valuable for characterizing two-dimensional materials. Examining the relationship between these properties enables insight into the doping processes and scattering mechanisms as function of environmental variables.

6.5 Methods

6.5.1 Cavity-enhanced terahertz optical Hall effect

The measurement technique implemented here is the cavity-enhanced terahertz optical Hall effect. Recently, this technique has been demonstrated as viable non-contact method to obtain free charge carrier properties using low-field permanent magnets[11,119]. A tunable, externally-coupled cavity is used to enhance the THz-OHE signal, which allows the accurate determination of a sample's free charge carrier properties even at low magnetic fields. Placing the sample near the THz reflective metal surface of the permanent magnet allows the typically unused radiation emitted out the backside of the sample to be reflected back in (Fig. 6.1b), thus enhancing the THz-OHE signal. Model simulations are used to determine the ideal external cavity size, which for this graphene sample is 100 μm.

6.5.2 Gas flow cell

The body of the gas flow cell (Fig. 6.1a) is constructed from Delrin, and the top and bottom lids are acrylic. The gas cell window material is homopolymer polypropylene and each window is 0.27 mm thick. The flow rate used in the cell is approximately 0.5 liters/minute. The background pressure for all gas exposure phases was 1 atm. A vacuum pump (Linicon) is used to flow unaltered ambient gas into the cell, and pressurized purge lines are used to provide nitrogen and helium flow. The permanent magnet mounted inside the cell is high-grade neodymium (N42). The magnetic field near the north surface is 0.55 Tesla, which is determined using a Hall effect sensor (Lake Shore). THz radiation shielding (not shown) is used to suppress edge reflections from side walls,

sample boundaries and magnet surfaces. The THz beam spot covers the entire sample. Any radiation incident on the edges of sample is suppressed by the THz radiation shielding.

6.5.3 Terahertz ellipsometer

Measurements were performed using a custom-built rotating-analyzer THz ellipsometer at the Terahertz Materials Analysis Center in Linköping University[119,154]. The instrument is capable of measuring the upper-left 3×3 block of the Mueller matrix, which fully characterizes the THz-OHE signal.

6.5.4 Sample growth and characterization

Monolayer graphene is grown by high-temperature sublimation in Ar atmosphere on Si-face 4H-SiC[154,174]. The representative 532-nm-wavelength reflectance-converted-thickness map (Fig. 6.1c) is obtained with a 300 nm lateral step resolution and a 100× objective[175]. The sample dimensions are 10 × 10 × 0.35 mm.

6.5.5 Ellipsometry and optical Hall effect model analysis

In this work, ellipsometry is used to determine graphene's free charge carrier properties. This is a technique, which measures polarization changes in electromagnetic radiation upon, in this case, reflection off a sample[7]. Ellipsometry is an indirect measurement technique that requires an optical model be fit to experimental data to obtain desired sample parameters. The fit algorithm used is the Levenberg-Marquardt non-linear regression method[176]. Here, ellipsometric data are reported in the Mueller matrix formalism[6].

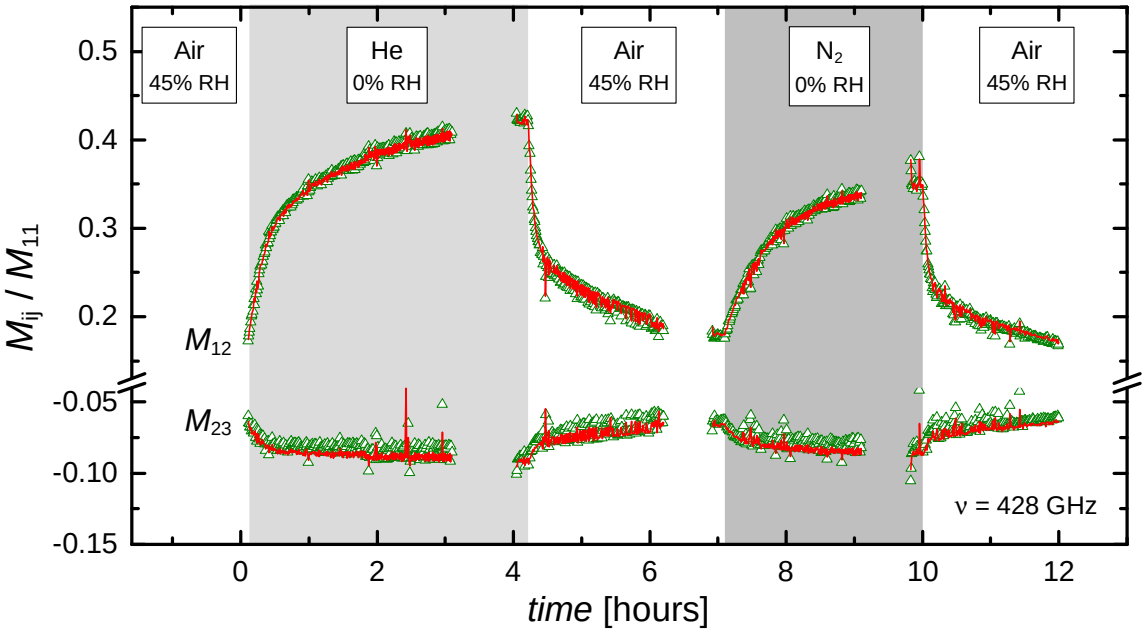

Figure 6.4: *In-situ* experimental (green triangles) and modeled (red lines) Mueller matrix data as a function of time for all gas exposure phases. The shaded regions correspond to different types of gas flow at various relative humidities (RH). Data shown here is acquired at a single frequency ν = 428 GHz. Mueller matrix elements not shown here are either similar or identical to the elements depicted and are excluded for brevity. Data is acquired at an angle of incidence $\Phi_a = 45^\circ$ and at room temperature.

The sample's optical response is governed by the dielectric function. In the THz spectral range, the dielectric function consists of contributions from free charge carriers and a magnetooptic contribution, which is due to the presence of magnetic field, as described in Ref. 4 and 126.

A stratified layer model is used to represent the graphene/SiC substrate/external cavity/metallic magnet surface system (Fig. 6.1b). The millimeter wavelength of the THz beam renders it insensitive to non-electrically conductive thin films of few nm thickness only. Hence, any intricate dielectric variations near the graphene-SiC interface, such as the formation of a buffer layer, is undetectable by our present ellipsometry setup. On the contrary, free charge carriers produce

very large dielectric responses, and are clearly detectable. Here, a 1 nm thick layer containing free charge carriers is used to represent the graphene atop the SiC substrate with no intermediate layers. The SiC substrate is insulating and no free charge carrier contribution is included for this layer. In the same vain, a water film is not included in the THz optical model either since previous experiments for similar samples and for similar environmental conditions have shown water adsorbates on epitaxial graphene on SiC to be approximately 1 nm thick[157]. Using previously determined dielectric constants for water at THz frequencies[177], our simulations show the change in polarization due to such a film can be neglected. This also implies that the inclusion of a water and/or buffer layer would have no effect on the accuracy of the reported N_s and μ values. Furthermore, the response of the bare Si-face SiC substrate as well as a buffer layer sample mounted on the permanent magnet were investigated by exposing to N_2 and unaltered ambient gas. No change in the measured data is observed when switching between the gases.

To obtain the parameters N_s and μ, the optical model was fit to the *in-situ* data acquired at a single frequency ($\nu = 428$ GHz). The parameters were determined by a point-by-point analysis, meaning N_s and μ were determined by a fit process to the experimental data obtained for each point in time separately.

Due to experimental constraints, effective mass m^* is not obtained in the analysis and has been implemented as function of N_s using the equation $m^* = \sqrt{(h^2 N_s)/(4\pi v_f^2)}$, where $v_f = 1.02 \times 10^6$ m/s is the Fermi velocity, according to Ref. 178. The cavity-enhanced THz-OHE is, in fact, capable of attaining m^* in addition to N_s and μ[11]. However to improve the time resolution of the *in-situ* measurement, experimental data was only obtained at one frequency $\nu = 428$ GHz, one angle of incidence $\Phi_a = 45^\circ$, and one sample-magnet air

gap distance d_{gap} = 100 μm. If one or more of these variables were utilized during the *in-situ* measurement the sensitivity to all free charge carrier properties would increase.

During data analysis, to correct for slight misalignment of the THz ellipsometer we employ one frequency- and time-independent correction matrix in the optical model. The correction is made by matrix multiplication of the Mueller matrix representing the sample-magnet system and a correction matrix representing a small constant offset induced by the instrument. To find the correction matrix values used in the analysis, all the elements of that matrix were fit to data obtained at multiple frequencies (385 to 395 GHz) before the gas flow experiment. In this spectral range, there are no changes due to the sample or magnet, but only changes from minor instrument non-idealities.

6.5.6 Experimental data

Figure 6.4 shows changes in the Mueller matrix data acquired at a single frequency ($\nu = 428$ GHz) as a function of time for different gas exposures. The Mueller matrix elements depicted here are M_{12} and M_{23}. For this sample and permanent magnet configuration, the M_{12} element experiences the largest change with variation in the free charge carrier properties. The frequency $\nu = 428$ GHz was chosen because this is where the maximum change in M_{12} occurs. The M_{23}, as well as all other off-block-diagonal Mueller matrix elements, characterize the THz-OHE signal and would be zero if there were no magnetic field present. The negative value of this element indicates the sample is n-type, since the sample is mounted on the north pole-face of the permanent magnet. Note that a sign reversal of this element would indicate a reversal of conductivity from n-type to p-type. Such type of change, for example, can be induced by

use of reactive gases such as NO_2 [158].

Breaks in the experimental data near the end of each gas flow phase are where data was obtained at multiple frequencies to verify the optical model. This is verification was done before the point-by-point analysis was performed. Data recorded prior to those reported here were taken during repeated gas exposure cycles, and were found highly reproducible. Note, certain Mueller matrix elements are excluded for brevity. The M_{21} and M_{32} are omitted due to being essentially equal to M_{12} and M_{23} respectively. M_{13} and M_{31} are essentially equal and are omitted since they resemble M_{23}. M_{22} and M_{33} show very little change and are omitted.

6.6 Acknowledgments

We acknowledge support from the Swedish Research Council (VR Contracts 2013-5580 and 2016-00889), the Swedish Governmental Agency for Innovation Systems (VINNOVA grants No. 2011-03486, 2014-04712), the Swedish Foundation for Strategic Research (SSF, grants No. FFL12-0181, RIF14-055), the Swedish Government Strategic Research Area in Materials Science on Functional Materials at Linköping University (Faculty Grant SFO Mat LiU No 2009 00971), the National Science Foundation through the Center for Nanohybrid Functional Materials (EPS-1004094), the Nebraska Materials Research Science and Engineering Center (DMR-1420645), and awards CMMI 1337856 and EAR 1521428.

Chapter 7

Tunable cavity-enhanced terahertz frequency-domain optical Hall effect

7.1 Abstract

Presented here is the development and demonstration of a tunable cavity-enhanced terahertz frequency-domain optical Hall effect technique. The cavity consists of at least one fixed and one tunable Fabry-Pérot resonator. The approach is suitable for enhancement of the optical signatures produced by the optical Hall effect in semi-transparent conductive layer structures with plane parallel interfaces. The physical principle is the constructive interference of electric field components that undergo multiple optical Hall effect induced polarization rotations upon multiple light passages through the conductive layer stack. Tuning one of the cavity parameters, such as the external cavity thickness, permits shifting of the frequencies of the constructive interference, and enhancement of the optical signatures produced by the optical Hall effect can be obtained over large spectral regions. A cavity-tuning optical stage and gas flow cell are used as examples of instruments that exploit tuning an external cavity to enhance polarization changes in a reflected terahertz beam. Permanent magnets are used to provide the necessary external magnetic field. Con-

veniently, the highly reflective surface of a permanent magnet can be used to create the tunable external cavity. The signal enhancement allows the extraction of the free charge carrier properties of thin films, and can eliminate the need for expensive super-conducting magnets. Furthermore, the thickness of the external cavity establishes an additional independent measurement condition, similar to, for example, the magnetic field strength, terahertz frequency, and angle of incidence. A high electron mobility transistor structure and epitaxial graphene are studied as examples. (This submitted manuscript has been reproduced with the permission of AIP Publishing)

7.2 Introduction

The optical Hall effect (OHE) is a phenomenon in which the optical response of a conductive material is altered by the presence of an externally applied magnetic field.[126] This effect can be measured with generalized ellipsometry at oblique angles of incidence and at terahertz (THz) frequencies. Previously, the THz-OHE has been proven as a viable non-contact method to obtain the free charge carrier properties of semiconductor heterostructures using high-field superconducting magnets.[5,118,128,129,130,179,132] This approach allows the extraction of a sample's carrier concentration, mobility, and effective mass parameters by using a THz-transparent substrate as a Fabry-Pérot cavity to resonantly enhance the THz-OHE signal. Recently, it has been shown these properties can be conveniently obtained with permanent magnets.[11,154,117,119] Using low-field permanent magnets to provide the external field significantly decreases the magnitude of the THz-OHE signal. However, one can compensate for this by exploiting an externally-coupled Fabry-Pérot cavity to further enhance the

signal. In Ref. 11, different external cavity thickness values are achieved by simply stacking multiple layers of adhesive spacers between the sample and magnet. This method is useful because it is straight-forward and low cost, but only large increments of cavity thickness can be produced. The cavity-tuning optical stage described in this work improves on this previous approach and is capable of finely tuning the cavity thickness thus providing a new measurement dimension. As an example of the cavity-tuning stage described here a sample-permanent magnet arrangement is placed inside a gas flow cell to improve sensitivity to small variations of free charge carrier parameters under varying gas flow conditions. This experiment highlights the advantage of the small footprint of this enhancement technique.

In this work, we discuss the concept of THz-OHE signal enhancement due to an externally-coupled cavity. An optical model is used to choose desirable measurement parameters, such as angle of incidence, frequency, and external cavity thickness. Details of the instrument design and data acquisition are explained. Experimental and model-calculated data are presented and compared with data for the case of no cavity-enhancement. It is demonstrated that the cavity-enhancement technique allows extraction of the free charge carrier properties of a two-dimensional electron gas (2DEG) at THz frequencies.

7.3 Method

7.3.1 Optical Hall effect

We refer to the OHE as a physical phenomenon that describes the occurrence of magnetic-field-induced dielectric displacement at optical wavelengths, transverse and longitudinal to the incident electric field, and analogous to the static

electrical Hall effect.[126,4] We have previously described data acquisition and analysis approaches for the method of the OHE in the mid-infrared, far-infrared, and THz spectral regions.[126,132,5,117]

7.3.2 Optical Hall effect model for thin film layer stacks

The OHE can be calculated by use of appropriate physical models. The models contain two portions, one describes a given material's dielectric function under an external magnetic field, the second portion describes the wave propagation within a given layer stack. We have provided a recent review on this topic in Ref. 4. Briefly, in the THz spectral range the dielectric function can be approximated by a static contribution due to phonon excitations and higher energy electronic band-to-band transitions. Contributions due to free charge carriers can be well described by the Drude quasi-free electron model.[180,181] In the presence of a static external magnetic field, an extension of the Drude model predicts magneto-optic anisotropy[182] and which is the cause of the classical OHE in conductive materials. (For quantum effects see, for example, Refs.[127,183,184])

7.3.3 Tunable cavity-enhanced optical Hall effect

The principle of the enhancement of the OHE in a layer stack is the constructive superposition of the magneto-optically polarization converted electromagnetic field components from multiple passages through the layer stack in the presence of an external magnetic field. Each time of passage, the electromagnetic field components undergo an additional polarization rotation caused by the magneto-optic anisotropy created by the response of the free charge carriers under the influence of the Lorentz force and within the conductive layer(s). At an interference maximum, the sensitivity to the portion of reflected light that has

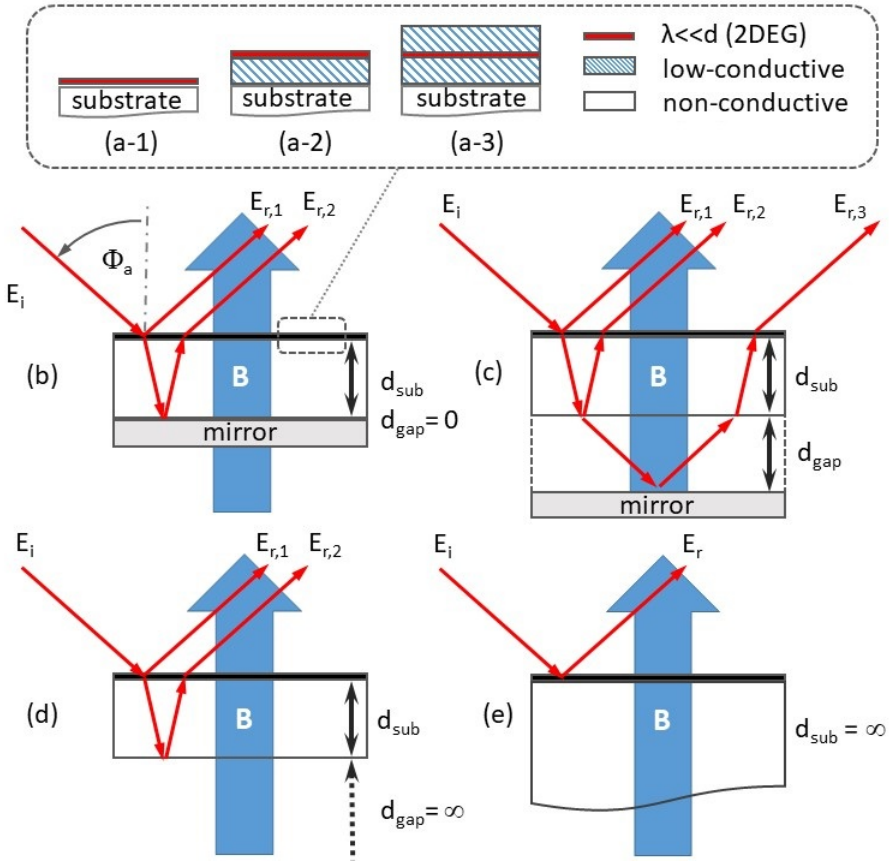

Figure 7.1: Principle of the tunable cavity-enhanced frequency-domain THz-OHE method, here applied to characterize a two-dimensional electron gas (2DEG). The 2DEG of interest may be part of a multiple layer stack with differently, low-conducting constituents, for example, directly at the interface of a substrate (Fig. 7.1(a-1)), or ontop of the layer structure (Fig. 7.1(a-2)), or within (Fig. 7.1(a-3)). The differently, low-conducting constituents (layers) should themselves be sufficiently THz transparent. The principle configuration requires a THz-transparent substrate. If the substrate has a finite thickness (d_{sub}), incident plane wave electric field (E_i) components are retro-reflected and pass the layer structure multiple times, where the first 2 orders are shown here for brevity only ($E_{r,1}, E_{r,2}$). A mirror placed at the opposite side of the substrate (Fig. 7.1b) can be used to control the frequencies of constructive interference maxima by d_{gap}, where fractions of plane wave components reflected off the mirror exit the sample, and only the first order of those are shown ($E_{r,3}$). If the mirror surface is distanced to the backside of the substrate by d_{gap}, the frequencies of constructive interference maxima can be tuned by d_{gap} (Fig. 7.1(c)). The angle of incidence is Φ_a. Fig. 7.1(d) depicts the situation when the mirror is removed ($d_{\mathrm{gap}} \rightarrow \infty$). Fig. 7.1(e) depicts the case when the substrate is optically infinite ($d_{\mathrm{sub}} \rightarrow \infty$), and against which the enhancement of the tunable cavity-enhanced OHE is to be referenced. The magnetic field **B** direction is not relevant for the enhancement. Here, all examples are discussed with direction of **B** perpendicular to the cavity interfaces. Drawing not to scale.

undergone polarization discriminating reflection or transmission optical intensity measurement is greatly enhanced towards the causes of the magneto-optic anisotropy.[11] The magnitude of the enhancement can be significant and which depends on the free charge carrier properties in a given sample configuration. Examples are discussed in this work.

The principle of the tunable cavity-enhanced OHE method is demonstrated in Fig. 7.1. All configurations require the layer stack to be supported by a THz-transparent substrate. The substrate must have a flat and polished backside whose surface is parallel to the front of the substrate carrying the layer stack. The thickness of the substrate d_{sub} should be such that spectrally neighboring Fabry-Pérot interference maxima and minima within the substrate can be sufficiently resolved with a given spectroscopic setup. Plane wave electric field (E_i) components incident under an angle Φ_a then pass the sample layer structure multiple times due to multiple internal reflections within the substrate cavity. The frequencies of such maxima are controlled by the angle of incidence, the substrate thickness and the substrate index of refraction. In principle, the substrate thickness is adjustable by depositing the sample layer stack onto different substrates. This, however, requires multiple fabrication steps. If a second cavity is created by the introduction of a mirror, placed at distance d_{gap}, the portion of electromagnetic waves lost at the backside of the substrate is fed back into the substrate, and introduces additional fractions of plane wave components passing the layer stack. The two Fabry-Pérot cavities (substrate, gap) couple, and produce coupled Fabry-Pérot resonances. The frequencies of the coupled interference maxima can then be tuned by d_{gap}, for any given but fixed d_{sub}. Then, the magneto-optic signal enhancement occuring at interference maxima, limited to certain frequencies for a given d_{sub} without external cavity, can be tuned

spectrally. Thereby, a new magneto-optic spectroscopy method is created where in addition to frequency, the external cavity is tuned by changing its thickness, d_{gap}.

Also shown in Fig. 7.1 are the limiting cases, when the external cavity is zero ($d_{\mathrm{gap}} \rightarrow 0$, Fig. 7.1(b)), infinite ($d_{\mathrm{gap}} \rightarrow \infty$, Fig. 7.1(d)), and when both cavity and substrate are infinite ($d_{\mathrm{sub}} \rightarrow \infty$, Fig. 7.1(e)). The case $d_{\mathrm{gap}} \rightarrow 0$ requires deposition of a metal layer onto the backside of the substrate. The case $d_{\mathrm{gap}} \rightarrow \infty$ occurs when the substrate is THz-transparent and has parallel interfaces. The case $d_{\mathrm{sub}} \rightarrow \infty$ occurs when the layer stack is deposited onto a non-transparent substrate or when the backside of a transparent substrate is not parallel, for example, if the substrate consists of a wedge or a prism.

7.3.4 Mueller matrix spectroscopic ellipsometry

The generalized ellipsometry concept[185], its spectroscopic extension,[186] and the Mueller matrix formalism[187] are employed in this work. The Mueller matrix connects Stokes vector[188] components of electromagnetic waves before and after interaction with the sample upon reflection or transmission. For the use of the Mueller matrix concept in spectroscopic generalized ellipsometry we refer the reader to recent reviews (see, e.g., Refs.[136,6]). For use of the Mueller matrix formalism in the OHE[189], and in particular, for data format definition we refer to Ref. 5.

7.3.5 Data analysis

Non-linear parameter regression analysis methods are used for data analysis. The experimental data are compared with calculated OHE data. The calculated data are obtained with appropriate physical models and model parameters. Pa-

rameters are varied until a best-match is obtained minimizing an appropriately weighted error sum. The error sum takes into account the systematic uncertainties determined during the measurement for each experimental data value. Best-match model parameter uncertainties are obtained from the covariance matrix using the 90% confidence interval.[5]

7.4 Instrument

The tunable cavity and sample must be placed within a THz spectroscopic ellipsometer system, and subjected to an external magnetic field. Ellipsometer, sample stage, and magnetic field designs are discussed in this section.

7.4.1 Terahertz frequency-domain ellipsometer

Two THz frequency-domain ellipsometer instruments are used in this work. Both instruments operate in the rotating-analyzer configuration which enables acquisition of the upper left 3×3 block of the 4×4 Mueller matrix. The frequency-domain source is a backward wave oscillator (BWO) with GaAs Schottky diode frequency multipliers. Technical details are described in Ref. 5 and Ref. 117.

7.4.2 Tunable cavity stage

Use of permanent magnet: A principle design of the sample holder for the tunable cavity-enhanced THz-OHE is shown in Fig. 7.2. In this design, the permanent magnet serves both as mirror as well as for providing the external magnetic field. The mirror properties of the magnet surface must be characterized by THz spectroscopic ellipsometry measurements at multiple angles of inci-

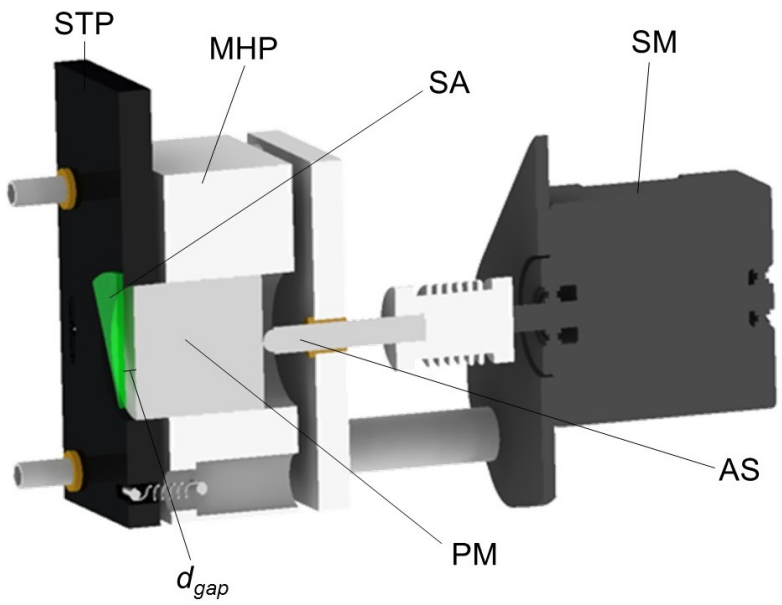

Figure 7.2: Technical schematic of the sample holder with cavity-tuning adjustment controls. The instrument is comprised of the spring-loaded sample tip-tilt plate (STP), the sample (SA), the stepper motor (SM), the mirror housing plate (MHP), the adjustment screw (AS), and the permanent magnet (PM). The external cavity distance (sample-magnet air gap) is labeled d_{gap}. The plate containing the AS is removable which allows the user to flip the permanent magnet to the opposite pole-face and redo experiments with opposite field direction without disturbing the sample alignment.

dence prior to its use in the sample stage. The permanent magnet (PM) sits flush inside a hole in the mirror housing plate (MHP). The micrometer adjustment screw (AS) rests inside a brass bushing in the back plate. The rounded tip of the AS is made of ferromagnetic material which attracts the magnet providing synchronous PM-AS movement. The stepper motor (SM) is attached to the back of the setup and is connected to the AS by a flexible bellows shaft coupler. The flexible coupler allows a d_{gap} range of approximately 0 μm to 600 μm. The stepper motor is operated by a commercially available motor controller (Thor Labs Inc.), which uses LabVIEW programming. The minimum d_{gap} increment

is 1.6 μm, corresponding to one step of the motor. The back plate in Fig. 7.2 is removable and allows the user to flip the magnet to the opposite pole-face and redo experiments without disturbing the sample alignment.

Use of fixed cavity spacer adjustments: For simplifying the tunable cavity-enhanced sample stage, non-magnetic adhesive spacers can be placed between the sample and the mirror surface dispensing with the need for the stepper motor in Fig. 7.2. This option is suitable for *in-situ* measurements when limited space is available. However, no tuning of the cavity after sample mounting can be performed.

Use of external electromagnet: For use of the sample holder with an external electromagnet, the permanent magnet can be replaced by a non-magnetic insert with a THz mirror at the front towards d_{gap} and the sample backside. The normal reflectance properties of the mirror can be evaluated by performing THz spectroscopic ellipsometry measurements at multiple angles of incidence prior to its use. The external magentic field can be provided by electromagnets, for example, by placing the stage within a Helmholtz coil arrangement.

7.5 Data Acquisition and Analysis

7.5.1 Data acquisition

Magnetic field calibration: The permanent magnet mounted in the sample holder is a high-grade neodymium (N42) magnet. With the use of a permanent magnet the change in magnetic field strength at the sample surface upon variation of d_{gap} can be substantial. Hence, it is necessary to implement the magnetic field as a function of distance in the optical model. Using a commercially

available Hall probe (Lakeshore), the magnetic field is measured at multiple d_{gap} values. For our instrument, within approximately 1 mm of the magnet surface the field is approximately linear and can be approximated using by:

$$\pm B = \pm[0.55 - (5.1 \times 10^{-5}) \times (d_{\text{gap}} + d_{\text{sub}})] \text{ [T]}, \tag{7.1}$$

where the plus and minus sign refers to the two respective pole orientations of the magnet. The parameters d_{gap} and d_{sub} are in units of micrometers.

Mirror calibration: Separate ellipsometry experiments are performed in the mid-infrared spectral range to determine the optical properties of the metallic permanent magnet surface as mirror. Data analysis is performed using the classical Drude model parameters for static resistivity of $\rho = (9.53 \pm 0.04) \times 10^{-5}$ Ωcm and the average-collision time $\tau = (1.43 \pm 0.08) \times 10^{-16}$ s. These parameters are used here to model-calculate the optical reflectance of the magnet surface for the model analysis in the THz spectral range for the cavity-enhanced measurements. The magnet surface behaves as an ideal metallic "Drude" mirror characterized by metal electron carrier scattering time and resistivity, and no magneto-optic polarization coupling occurs because the metal electron effective mass is too large and the mean scattering time is too short in order for the free charge carriers to respond to the external magnetic field producing measurable magnetooptic birefringence.

Mirror-to-ellipsometer alignment: The mirror surface is aligned first and then the sample is mounted and aligned. The mirror surface is aligned to the ellipsometer's coordinate system by use of a laser diode mounted such that the laser diode beam is parallel to the plane of incidence, perpendicular to the

sample surface, and coincides with the center of the THz beam at the sample surface. A gap value d_{gap} is selected in the middle of the range of values anticipated for experiments. To align the mirror, the alignment laser diode beam is reflected off the mirror surface and the mirror is adjusted until the beam reflects back into the laser aperture. The adjustment is performed by moving the entire stage relative to the ellipsometer system.

Sample-to-mirror alignment: Once the mirror is aligned, the sample is mounted to the sample tip-tilt plate STP (Fig. 7.2). STP serves as an adjustable frame to mount the sample. The sample can be mounted via adhesive, for example, or mechanical clamps. STP contains three micrometer screws secured against the MHP by springs, creating a tip-tilt ability. This is necessary to ensure that the sample surface is also aligned to the ellipsometer's coordinate system. The sample surface is aligned using the same alignment laser as for the mirror.

Ellipsometry data acquisition: After mounting the sample stage into the ellipsometer system, data are acquired in a selected spectral range, for selected angles of incidence Φ_a, and gap distance d_{gap}. Figure 7.3 depicts a flow chart describing the data acquisition process. First, the sample-mirror air gap distance d_{gap} is set. Next, the frequency-domain source frequency is set. Then the polarizer angle is set and the intensity at the detector is recorded. The process is repeated for all polarizer settings as described in Ref. 5, and a Fourier transform of the signal is performed to determine the Fourier coefficients, which are stored and then subject to a regression analysis. As a result, the elements of the upper 3×3 block of the Mueller matrix are obtained. The procedure is repeated for different settings of gap distance, frequency, or angle of incidence, for exam-

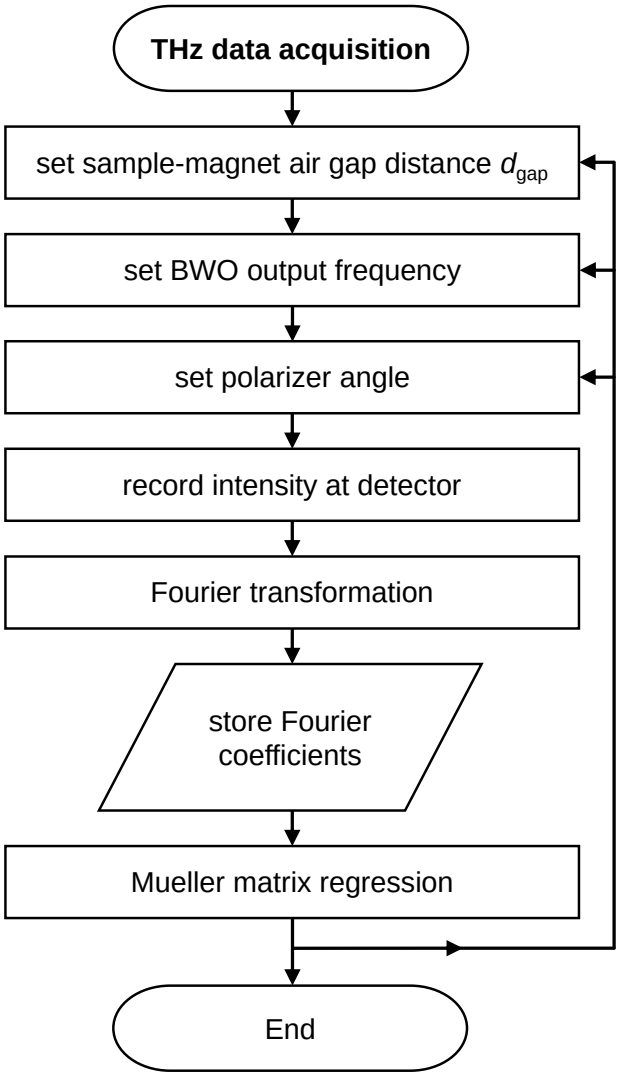

Figure 7.3: Flow chart describing the data acquisition process of the cavity-tuning optical stage and ellipsometer.

ple. The acquisition process can be repeated with the magnetic field direction reversed, for example, by reverting the magnet direction, or by reverting the currents in external electromagnetic coils. The experiment can also be repeated with a mirror without a magnet for acquisition of field-free ellipsometry data.

7.5.2 Data analysis

Data measured by tunable cavity-enhanced THz-OHE are analyzed using model calculations and numerical regression procedures. Multiple data acquisition modes are available, and which will be discussed by examples further below.

Cavity-enhanced data at tunable gap thickness: Data obtained as a function of gap thickness are compared with calculated data.

Cavity-enhanced data at tunable frequency: Data obtained at a fixed gap and/or substrate thickness but as a function of frequency are compared with calculated data.

Cavity-enhanced data at tunable frequency and tunable gap thickness: Data over a 2-dimensional parameter set can be obtained tuning both gap thickness and frequency and are compared with calculated data.

Cavity-enhanced data at magnetic field reversal: Field-reversal OHE data obtained at opposing magnetic field directions, $\Delta M_{ij} = M_{ij}(B) - M_{ij}(-B)$, are taken and the difference data is compared with calculated data.

7.6 Results and Discussion

Here we discuss two sample systems as examples for the application of the tunable cavity-enhanced OHE. Both samples contain 2DEGs. The characterization of their free charge carrier properties is demonstrated. One sample is comprised of a transistor device structure for a high electron mobility transistor (HEMT) based on group-III nitride semiconductor layer structures. The second sample is an epitaxial graphene sample grown on a silicon carbide substrate.

7.6.1 Two-dimensional electron gas characterization in a HEMT device structure

7.6.1.1 Sample structure

Growth: The sample investigated is an AlInN/AlN/GaN HEMT structure grown using an AIXTRON 200/4 RF-S metal-organic vapor phase epitaxy system. The HEMT structure consists of a bottom 2 μm thick undoped GaN buffer layer, a 1 nm thick AlN spacer layer, followed by a 12.3 nm thick $Al_{0.82}In_{0.18}N$ top layer.[137,12] The substrate is single-side polished *c*-plane sapphire with a nominal thickness of 350 μm.

Optical sample structure: All sample constituents are optically uniaxial and the layer interfaces are plane parallel. In a separate experiment, the HEMT structure was investigated using a commercial (J.A. Woollam Co. Inc.) mid-infrared (MIR) ellipsometer from 300-1200 cm^{-1} at Φ_a = 60° and 70° at room temperature in order to determine phonon mode parameters of the AlInN top layer. No distinct phonon features are seen in the THz measurements. However, the MIR analysis is used to help determine the dielectric function of the HEMT

structure constituents in the THz spectral range. Phonon parameters for the substrate, GaN buffer layer, and AlN spacer layer are taken from Ref. 190, 130, and 87, respectively. The thickness of the AlInN and AlN layers are found by growth rate calculations and not varied in the analysis. The best-match model layer thickness for the GaN layer is (2.11 ± 0.01) μm. For the AlInN top layer, the best-match model frequency and broadening parameters for the one-mode type E1- and A1-symmetry are $\omega_{\mathrm{TO},\perp} = (625.4 \pm 0.8)$ cm^{-1}, $\omega_{\mathrm{LO},\perp} = (877.8)$ cm^{-1}, $\gamma_{\perp} = (40.8 \pm 1.5)$ cm^{-1}, $\omega_{\mathrm{TO},\parallel} = (610)$ cm^{-1}, $\omega_{\mathrm{LO},\parallel} = (847.8 \pm 0.4)$ cm^{-1}, $\gamma_{\parallel} = (11.3 \pm 0.4)$ cm^{-1} which are in good agreement with previous works[191]. Note, certain phonon parameters are functionalized according to Ref. 191, and were not varied in the analysis. In order to obtain an excellent match between experimental and model-calculated THz-OHE data, a low-mobility electron channel was included in the AlInN top layer. This same low-mobility channel was also included in our previous model analysis for the same HEMT structure.[12,11] A mobility value of $\mu = 50$ cm^2/Vs for a similar HEMT structure is adopted for this sample, and an effective mass parameter of 0.3 m_0 is taken from density function calculations in Ref. 192. The volume density value for the low-mobility channel was previously determined to be $N = 1.02 \times 10^{20}$ cm^{-3}. This value is not varied in our analysis.

Previous OHE characterization: In Ref. 12 we reported field-reversal high-field OHE measurements on the same HEMT sample without external cavity. The high field measurements were performed in a cryogenic superconducting magnet setup. In Ref. 11 we reported field-reversal cavity-enhanced OHE measurements using a permanent magnet and various adhesive spacers (discrete settings for d_{gap}) on the same sample. The results reported in this work are

in excellent agreement with those reported previously. All THz-OHE results further compare well with Hall effect and C-V measurements done on similar samples.[193,1]

7.6.1.2 Single-frequency tunable-cavity measurements

Figure 7.4 shows experimental and best-match model data for field-reversal cavity-enhanced OHE data as a function of d_{gap} for the HEMT sample. The experiment was performed at two different, fixed frequencies of ν = 860 GHz and 880 GHz for a d_{gap} range of 120 μm to 520 μm in increments of 3 μm. The experimental data for both frequencies are analyzed simultaneously. The layer stack optical model for the best-match model calculation is AlInN/AlN/GaN/sapphire substrate/external cavity/mirror (magnet surface). The external magnetic field is oriented normal to the sample surface. All off-block diagonal Mueller matrix elements are zero for the HEMT sample structure without external magnetic field. To begin with, the solid blue lines in Figs. 7.4(a,b) are model calculated data for the same HEMT structure in the absence of the cavity enhancement (Fig. 7.1(e), $d_{\text{sub}} = \infty$, $d_{\text{gap}} = \infty$), where we assumed that the field at the layer stack is $B = \pm 0.55$ T. Specifically, $\Delta M_{13} = \Delta M_{31} = -0.0004$ and $\Delta M_{23} = \Delta M_{32} = 0.004$. Data are below our current instrumental uncertainty limit for the individual Mueller matrix elements of $\delta M_{ij} \approx \pm 0.01$. Hence, the 2DEG within the HEMT layer structure would not be detectable. In the cavity-enhanced mode, however, large off-diagonal Mueller matrix elements appear, far above the current instrumental uncertainty level, upon variation of the gap thickness d_{gap}. Features in Figs. 7.4(a,b) are due to Fabry-Pérot interference enhanced cross-polarized field components after reflection at the layer stack. Minima and maxima occur as a function of gap thickness. The

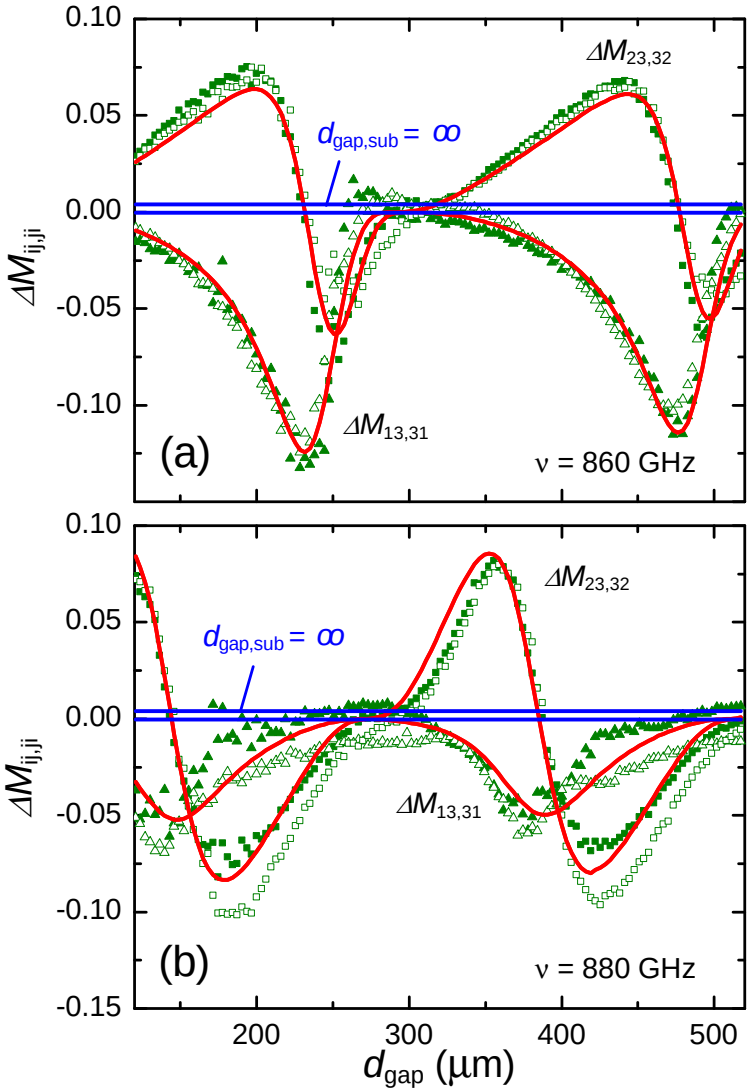

Figure 7.4: Experimental (green symbols) and best-match model calculated data (red solid lines) field-reversal cavity-enhanced OHE data as a function of the external cavity thickness d_{gap}, at two frequencies for a HEMT layer structure on sapphire. Closed and open triangles represent ΔM_{13} and ΔM_{31} respectively. Closed and open squares represent ΔM_{23} and ΔM_{32} respectively. The blue solid lines are model-calculated data for the case of no cavity-enhancement (d_{gap}=∞, d_{sub}=∞). All data is obtained at angle of incidence $\Phi_a = 45^\circ$ and at room temperature.

cross polarization is produced only by the free charge carrier gas within the HEMT structure under the influence of the Lorentz force. The potential to use the variation of gap thickness as a new parameter variation measurement configuration is obvious. In particular, for this sample, and for the scans shown in Figs. 7.4(a,b), compared with the blue lines (no cavity enhancement) cavity thickness parameters can be adjusted where the OHE signal enhancement reaches -0.124 at ν=860 GHz in Fig. 7.4(a) for $\Delta M_{13,31}$ and 0.088 for ν=880 GHz in Fig. 7.4(b) for $\Delta M_{23,32}$. The best-match model 2DEG sheet density, mobility, and effective mass parameters obtained from the OHE data in Figs. 7.4(a,b) are $N_s = (1.23 \pm 0.13) \times 10^{13}$ cm^{-2}, $\mu = (1245 \pm 64)$ cm^2/Vs, $m^* = (0.272 \pm 0.013) m_0$, respectively. The results are in excellent agreement with electrical measurements and with our previous THz-OHE experiments.[11]

7.6.1.3 Tunable-frequency tunable-cavity measurements

False-color rendering of model calculated data of cavity-enhanced field-reversal THz-OHE data versus frequency, gap thickness, and angle of incidence are shown in Fig. 7.5. The color type indicates positive or negative values, the color intensity indicates the magnitude of the OHE data. The three-dimensional rendering is insightful as it indicates distinct regions within which the data rapidly switches signs, and regions within which data takes very large values. All three parameters, frequency, gap thickness, and angle of incidence influence the OHE data, and proper selection may result in strong OHE data, while poor choices may result in disappearance of the OHE data. The horizontal plane indicated at 45° identifies the angle of incidence at which experiments are performed in this work. False-color rendering of experimental and model-calculated data at angle of incidence of 45° are shown in Fig. 7.6(a) as a function of frequency and gap

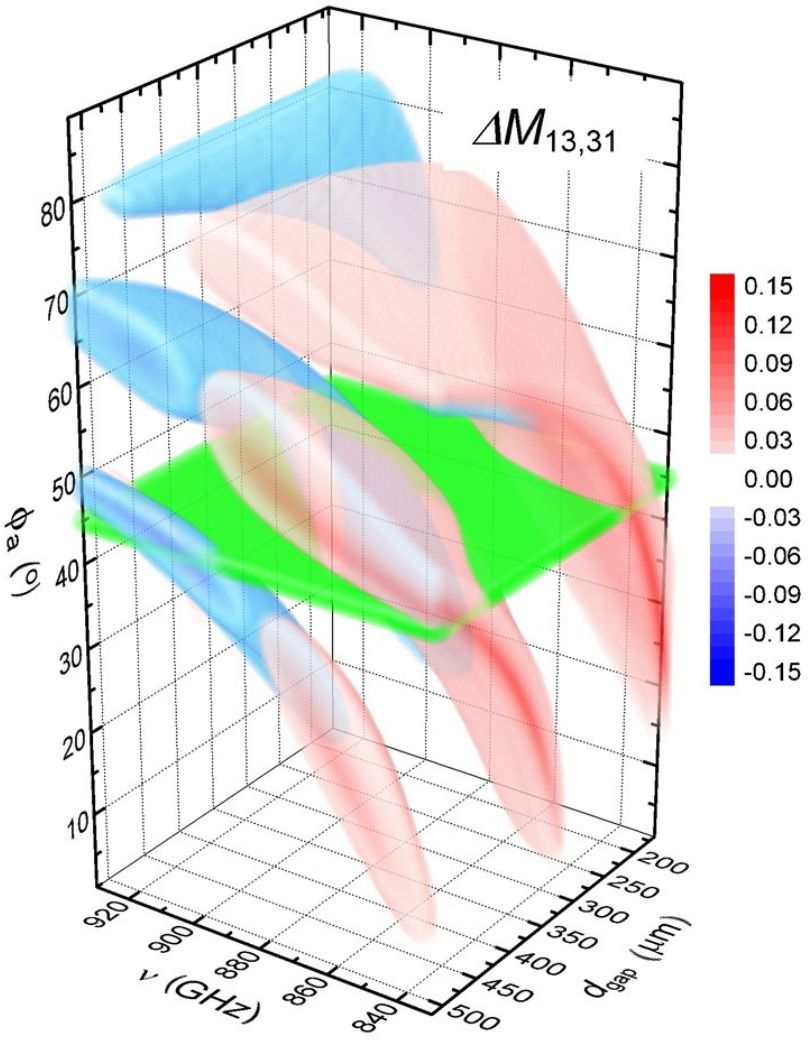

Figure 7.5: False-color three-dimensional surface rendering of model-calculated cavity-enhanced field-reversal THz-OHE data for an AlInN/AlN/GaN HEMT structure grown on a sapphire substrate as functions of frequency ν, external cavity distance d_{gap}, and angle of incidence Φ_a. Data for $\Delta M_{13,31} = M_{13,31}(+B)$ - $M_{13,31}(-B)$ are shown as example. Values within the range of -0.02 to 0.02 are omitted for clarity. The green horizontal plane at $\Phi_a = 45^\circ$ indicates the instrumental settings for the angle of incidence in this work. Model parameters given in text. Note that the model calculated plot for $\Delta M_{23,32}$ is similar in appearance to $\Delta M_{13,31}$ and is excluded here for brevity.

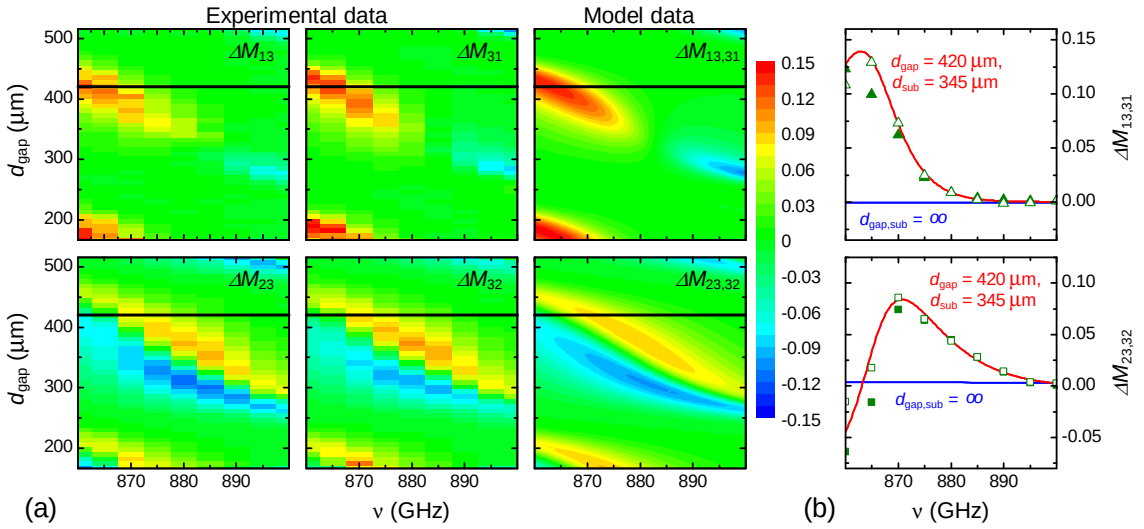

Figure 7.6: (a) False-color two-dimensional surface rendering of experimental (left two columns) and model-calculated (right column) cavity-enhanced field-reversal THz-OHE data for an AlInN/AlN/GaN HEMT structure grown on a sapphire substrate as functions of frequency ν and external cavity distance $d_{\rm gap}$. The angle of incidence is Φ_a = 45°. Data for $\Delta M_{13,31} = M_{13,31}(+B)$ - $M_{13,31}(-B)$ are shown as example. Parameter details given in text. (b) Same as in (a) for fixed cavity thickness $d_{\rm gap}$ = 420 μm. The solid blue line indicates model calculated data when $d_{\rm sub}$=∞ and $d_{\rm gap}$=∞. Solid green symbols indicate ΔM_{13} and ΔM_{23}, and open symbols indicate ΔM_{31} and ΔM_{32}. The blue solid lines are model-calculated data for the case of no cavity-enhancement ($d_{\rm gap}$=∞, $d_{\rm sub}$=∞). All data taken at room temperature.

thickness. An excellent agreement between both experiment and model calculation is obtained. Fig. 7.6(b) shows data at a fixed cavity thickness. Data are similar to those in Figs. 7.4(a,b), except now the frequency is tuned. Figs. 7.6(a,b) identify frequency and gap regions where the OHE data is very small. The blue solid lines are identical to those in Figs. 7.4(a,b) for the case of no cavity-enhancement. All experimental data in Fig. 7.6 is analyzed simultaneously and the resulting best-model sheet density, mobility, and effective mass parameters for the 2DEG are $N_{\rm s} = (1.22 \pm 0.12) \times 10^{13}$ cm^{-2}, $\mu = (1262 \pm 59)$ cm^2/Vs, $m^* = (0.268 \pm 0.012) m_0$. The results are identical within the error bars to those

obtained from the single frequency gap thickness scans as well as to our previous OHE investigation reports.[5,11]

The central results obtained from this section are (i) the demonstration of the strong enhancement obtained by use of multiple interference through substrate and external cavities, and (ii) the obvious appearance from Fig. 7.5 and the support from our experiments that OHE measurements can be performed both as a function of frequency and gap thickness.

7.6.2 Environmental gas doping characterization in epitaxial graphene

In this section we demonstrate the use of the cavity-enhanced OHE method for detecting changes in the properties of a 2DEG upon exposure to various external gas compositions. The purpose of this section is to demonstrate the use of this method when transient physical changes to a sample limit the time durations during which spectroscopic scanning measurements can be performed.

7.6.2.1 Sample structure

Growth: The sample studied here is graphene epitaxially grown on Si-face (0001) 4H-SiC by high-T sublimation in Ar atmosphere.[13] Reflectivity and low-energy electron microscopy mapping, and scan lines verify the primarily one monolayer coverage across the 10×10 mm sample surface.

Optical sample structure: The sample is optically modeled by considering the graphene monolayer as a 1 nm highly conductive thin film on top of the SiC substrate as described in Ref. 13. All sample constituents have plane parallel interfaces. No free charge carriers are detected in the SiC substrate. Due to the ultrathin layer thickness of the graphene, ellipsometry data cannot differentiate

between the thickness and the dielectric function of the layer. Instead, a new parameter emerges, the sheet free charge carrier density, This parameter takes a constant ratio with the assumed layer thickness, and hence can be determined independently and accurately (Further details are discussed in Refs.[13,4]).

***In-situ* gas cell design:** The schematics of the *in-situ* gas flow cell used in this work is shown in Fig. 7.8(a). The THz ellipsometer instrument is schematically indicated by source, polarizer, analyzer, and detector at angle of incidence $\Phi_a = 45^\circ$.[117] The cell is equipped with a humidity and temperature sensor, gas inlets, and gas outlets. The side walls of the flow cell are made from Delrin, and the cover and base portions are made from acrylic. THz-transparent windows are produced from homopolymer polypropylene. The thickness of the transparent sheets is 0.27 mm. Normal ambient gas is pushed through the cell using a vacuum pump (Linicon). Nitrogen and helium flow was provided by additional purge lines. The background pressure in the cell was 1 atm throughout the experiment. The flow rate was 0.5 liters/minute.

Fixed cavity-enhancement settings: The sample consists of a 2DEG (graphene) at the surface of a THz-transparent substrate ($d_{\mathrm{sub}} = 355\ \mu$m). The substrate is placed with its backside using adhesive spacers onto the permanent magnet (Fig. 7.8(a)). The sample is mounted with the neodymium (N42) magnet into the gas cell. The gap thickness d_{gap} was thereby fixed at 100 μm. OHE data acquisition is identical to the procedure in Fig. 7.3 with fixed cavity thickness.

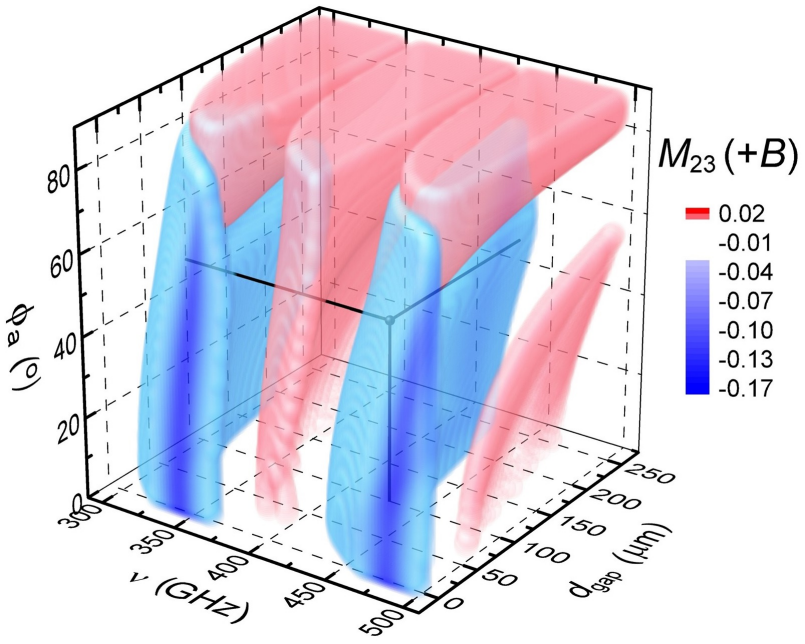

Figure 7.7: False-color three dimensional surface rendering of model-calculated cavity-enhanced single-field THz-OHE data for an epitaxial graphene layer on SiC as a function of frequency ν, external cavity distance d_{gap}, and angle of incidence Φ_a. Data for $M_{23}(+B)$ are shown only (0.02 to 0 (red) and -0.04 to -0.17 (blue)). Data with values between -0.04 and 0 are omitted for clarity. The black sphere at the intersection of the three black lines illustrates the point where *in-situ* gas cell data was taken for the gas flow experiments on the sample shown on this work. For model calculations the following parameters are used: $N_s = 8.69 \times 10^{11}$ cm^{-2} and $\mu = 2550$ cm^2/Vs. The effective mass parameter of $m^* = 0.019\ m_0$ is calculated as a function of N_s as in Ref. 194.

7.6.2.2 Cavity-enhanced optical Hall effect simulations

Figure 7.7 shows model-calculated THz-OHE data for M_{23} as function of ν, d_{gap}, and Φ_a for epitaxial graphene grown on SiC. Figure 7.7 can be used as a guide to find optimal values for ν, d_{gap}, and Φ_a to perform a THz-OHE measurement. The black sphere and three intersecting lines illustrates the point chosen to perform the *in-situ* THz-OHE measurement. Only a single set of measurement parameters is chosen to minimize time between measurements

in order to resolve sharp dynamic changes in the Mueller matrix data during the gas flow experiment. For practical reasons, $d_{\text{gap}} = 100$ μm and $\Phi_a = 45^\circ$ were chosen. Therefore, ν = 428 GHz was selected for the *in-situ* measurement. Unlike Fig. 7.5, Fig. 7.7 is not THz-OHE difference data since the gas flow experiment is only performed using the north pole-face of the permanent magnet.

7.6.2.3 *In-situ* tunable-frequency single-cavity measurements

Figures 7.8(c,d) depict experimental and best-match model data for single-field-orientation cavity-enhanced OHE data as a function of frequency for the graphene sample. These measurements were performed at two different points during the gas exposure experiment: the first spectral measurement was after three hours of exposure to helium, and the subsequent spectral measurement after two hours of exposure to ambient air (labeled 'T_1' and 'T_2' in Fig. 7.8(b), respectively). Indicated in Figs. 7.8(c,d) are also the THz-OHE data without cavity enhancement (blue lines: $d_{\text{gap,sub}} = \infty$). Comparing the cavity-enhanced data to the case of no cavity-enhancement indicates large changes in the Mueller matrix data are entirely due to interference enhancement in the substrate and external cavity. The off-block-diagonal element M_{23} is selected to show the OHE signature enhancement.

7.6.2.4 *In-situ* time-dependent single-frequency single-cavity measurements

Figure 7.8(b) shows the *in-situ* cavity-enhanced THz-OHE data taken at a single frequency, ν = 428 GHz, for M_{12} and M_{23}. Analyzing the data allows the extraction of the graphene's free charge carrier properties N_s, μ, and charge carrier type as a function of time. The carrier type is determined to be n-type during each gas phase. It is found that N_s increases with helium and nitrogen

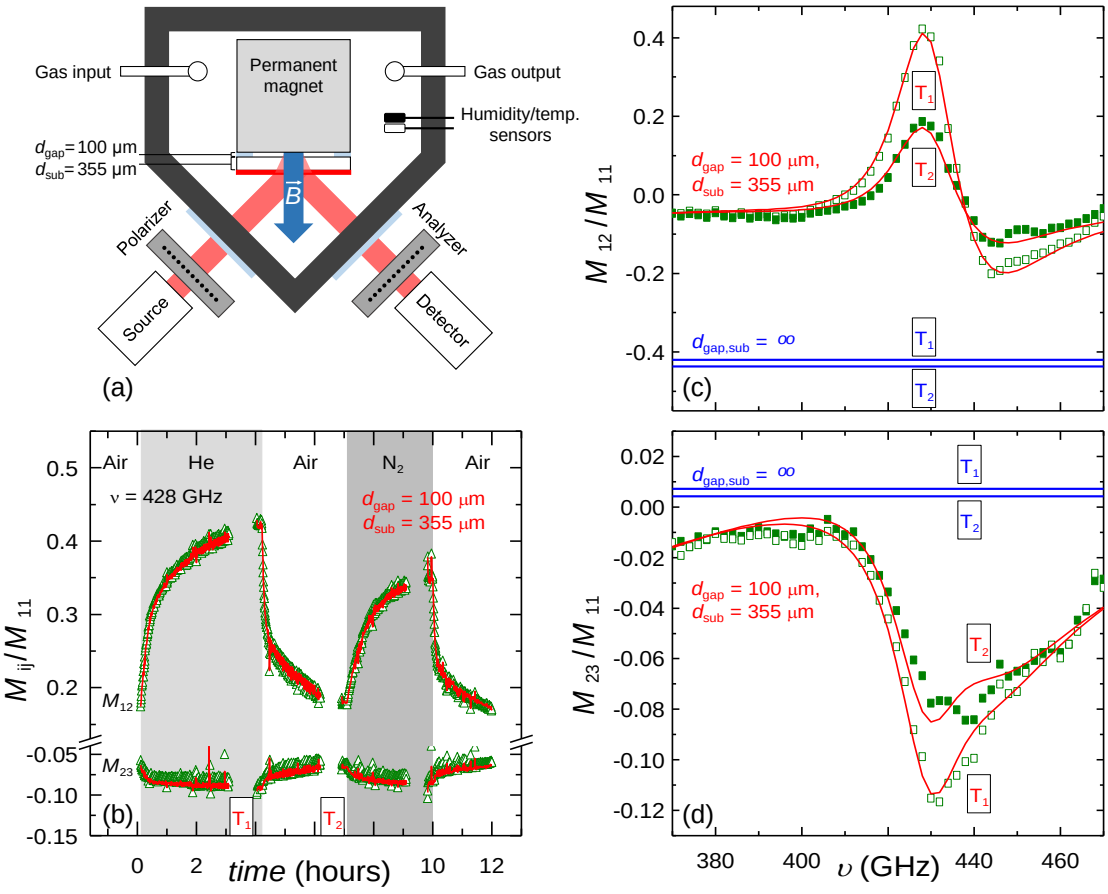

Figure 7.8: *In-situ* cavity-enhanced THz-OHE gas flow experiment and results. Contents of Figs. 7.8(a,b) are adapted from Ref. 13 which is licensed under a Creative Commons Attribution 4.0 International License[195]. Gas cell schematic (a) for gas exposure experiment on epitaxial graphene grown on SiC. In panel (b), *in-situ* experimental (open triangles) and best-match model data (solid red line) at single frequency (ν = 428 GHz) for two selected Mueller matrix elements are shown. Normalized M_{12} (c) and M_{23} (d) spectra are shown at two different times during the gas exposure experiment (labeled 'T_1' and 'T_2') for the cases with the cavity-enhancement effect (d_{gap} = 100 μm and d_{sub} = 355 μm) and without ($d_{gap,sub} = \infty$). In panels (c) and (d) experimental data is shown as open and closed squares, and model-calculated data are solid lines. Note, the experiment is performed only on one side of the permanent magnet (north pole-face) and thus Mueller matrix difference data is not obtained.

exposure, and decreases with air exposure. An inverse relationship is observed for μ and N_s throughout the gas flow experiment. The lowest N_s occurred at the end of the second air phase where $N_s = (8.40 \pm 0.72) \times 10^{11}$ cm^{-2} and $\mu = (2595 \pm 217)$ cm^2/Vs. The highest N_s occurred at the end of the helium phase where $N_s = (2.31 \pm 0.29) \times 10^{12}$ cm^{-2} and $\mu = (1961 \pm 250)$ cm^2/Vs. Further details on the *in-situ* THz-OHE gas exposure experiment can be found in our previous publication.[13] Sensitivity to the free charge carrier properties as a function of gas flow is entirely dependent on the cavity-enhancement effect, as demonstrated in Figs. 7.8(c,d). The variations in free charge carrier properties upon exposure with He and Air, indicated by the blue lines in Figs. 7.8(c,d), would not have been detectable with the same instrument without the external cavity stage since the changes in Mueller matrix elements are below the detection limit.

7.7 Conclusion

We demonstrated a tunable cavity-enhanced THz frequency-domain OHE technique to extract the free charge carrier properties of 2DEG layers situated on top of THz-transparent substrates. A HEMT structure grown on sapphire and epitaxial graphene grown on SiC are studied as examples. For the HEMT structure sample, the OHE signatures are enhanced by tuning an externally coupled Fabry-Pérot cavity via stepper motor. Data measured as a function of external cavity size and frequency are analyzed to obtain the carrier concentration, mobility, and effective mass parameters of the 2DEG located within the HEMT structure. For the epitaxial graphene on SiC sample, an external cavity of fixed size is used to enhance the OHE signal during a gas flow experiment.

This enhancement effect allows the extraction of the graphene's carrier concentration and mobility as a function of time throughout the experiment. In our experiments, the Fabry-Pérot cavity-enhancement is made possible by the THz-transparent substrates as well as the external cavity (air gap) between the sample's backside and the reflective metal surface. The magnetic field necessary for the OHE experiments is provided by a permanent magnet; for which the metallic coating also provides the reflective surface for the external cavity. Our enhancement technique can be expanded upon by using superconducting magnets to measure samples with much lower free charge carrier contributions. In general, our technique is a powerful method for materials characterization, and can be used to study even more complex sample structures.

7.8 Acknowledgments

We thank Dr. Craig M. Herzinger for helpful discussions. Prof. Nikolas Grandjean is gratefully acknowledged for providing the AlInN/GaN HEMT structure. We thank Dr. Chamseddine Bouhafs and Dr. Vallery Stanishev for growing the graphene sample, and Prof. Rositsa Yakimova for providing access to her sublimation facility for graphene growth. This work was supported in part by the National Science Foundation under award DMR 1808715, by Air Force Office of Scientific Research under award FA9550-18-1-0360, by the Knut and Alice Wallenbergs Foundation supported grant 'Wide-bandgap semiconductors for next generation quantum components', by the Swedish Agency for Innovation Systems under the Competence Center Program Grant No. 2016-05190 and 2014-04712, Swedish Foundation for Strategic Research (RFI14-055, EM16-0024), Swedish Research Council (2016-00889), Swedish Government Strategic

Research Area in Materials Science on Functional Materials at Linköping University (Faculty Grant SFO Mat LiU No. 2009 00971), and the J.A. Woollam Foundation.

Chapter 8

Conclusion

In summary, OHE measurements were used to determine the free charge carrier properties of important two-dimensional materials and monoclinic oxides. Bulk single-crystal β-Ga_2O_3, an AlInN/GaN-based HEMT structure, and epitaxial graphene were characterized as examples of such materials. OHE measurements were performed in two different spectral ranges: the MIR range for single-crystal β-Ga_2O_3, and the THz range for the HEMT structure and epitaxial graphene. For the THz-OHE measurements, Fabry-Pérot interferences inside the substrates and external cavity were exploited to increase the OHE signal-to-noise ratio. Results for free charge carrier properties extracted using OHE were compared with previous results from electrical Hall effect measurements, as well as DFT calculations. Since no OHE measurements were performed for the ThO_2, UO_2, and CuO samples, these investigations serve as introductions to infrared ellipsometry and Fabry-Pérot enhanced THz ellipsometry. All results and important concepts throughout dissertation are summarized as follows:

- **MIR/FIR characterization of single-crystal ThO_2 and UO_2**

  Standard ellipsometry was used to characterize the infrared-active phonon modes of single-crystal samples of ThO_2 and UO_2.[8] Both crystals were

found to have one main infrared-active mode pair, in addition to a broad low-amplitude impurity-like mode pair within the reststrahlen band. Further elevated temperature measurements were performed only on the ThO_2 sample. All infrared-active phonon mode center frequency parameters were found to decrease with increasing temperature. Trends in the temperature evolution of the TO center frequency match previous DFT calculations which only consider volume change effects. All results are comparable to previous reflectance spectroscopy charaterizations and DFT predictions. No significant Drude contribution was detected, therefore, no OHE measurements were performed.

- **Free charge carrier properties of Sn-doped single-crystal β-Ga_2O_3**

  Volume carrier concentration, mobility, and effective mass of Sn-doped monoclinic single-crystal β-Ga_2O_3 were determined by MIR-OHE in a combined analysis of (010) and (-201) surface cut crystals.[9] The extracted carrier type (n-type), carrier concentration ($N = (4.2 \pm 0.1) \times 10^{18}$ cm^{-3}) and mobility ($\mu = (44 \pm 2)$ cm^2/Vs) are in excellent agreement with previous electrical Hall effect measurements. The electron effective mass is found to be $m^* = (0.284 \pm 0.013) m_0$ which falls within the range of values predicted by various DFT calculations. No anisotropy in the mobility or effective mass is detected within our uncertainty limits.

- **THz characterization of single-crystal CuO**

  Generalized THz ellipsometry was employed to characterize a single-crystal sample of CuO as function of frequency and temperature to measure an electromagnon excitation.[10] This excitation manifests as an optical absorption near 0.705 THz and 215 K. The complex-valued dielectric func-

tion which corresponds to the electrmagnon excitation was modeled using the Lorentz oscillator approach. Fabry-Pérot interferences inside the CuO significantly enhance the measured signal-to-noise ratio, allowing this subtle excitation to be characterized.

- **Free charge carrier properties of an AlInN/GaN-based HEMT structure**

  THz-OHE measurements were employed to determine the free charge carrier properties of a 2DEG within an AlInN/GaN-based HEMT structure.[11] The carrier type (n-type), sheet density ($N_s = (1.02 \pm 0.15) \times 10^{13}$ cm^{-2}), and mobility ($\mu = (1417 \pm 97)$ cm^2/Vs) are comparable with previous electrical Hall effect results from similar samples. The effective electron mass is found to be $m^* = (0.244 \pm 0.020)m_0$. The necessary magnet field was provided by a low-field (B = 0.55 T) permanent magnet. To enhance the THz-OHE signal, the external cavity (i.e. sample-magnet air gap) was exploited as a Fabry-Pérot cavity to provide additional constructive interference. All results obtained with this cavity-enhanced technique are excellent agreement with a previous characterization using a high-field superconducting magnet (B = 7 T) and no external cavity-enhancement.

- **Free charge carrier properties of epitaxial graphene as a function of gas exposure**

  In-situ THz-OHE measurements were used to determine the free charge carrier properties of epitaxial graphene grown on SiC as a function of gas exposure.[13] The same cavity-enhancement effect described for the HEMT structure was implemented for these experiments. Sheet density (N_s) and mobility (μ) experience large changes when exposed to cycles of ambient air and dry helium. For example, at the end of the second ambient air

cycle: $N_s = (8.40 \pm 0.72) \times 10^{11}$ cm^{-2} and $\mu = (2595 \pm 217)$ cm^2/Vs. At the end of the first cycle of dry helium: $N_s = (2.31 \pm 0.29) \times 10^{12}$ cm^{-2} and $\mu = (1961 \pm 250)$ cm^2/Vs. Since the measured THz-OHE data provided limited sensitivity to the effective mass parameter, it was written as a function of N_s, and was not varied during the analysis.[194]

- **Fabry-Pérot cavity tuning techniques for obtaining 2DEG free charge carrier properties**

  Techniques for precisely tuning an external Fabry-Pérot cavity in order to enhance THz-OHE signatures in certain samples was shown experimentally and discussed.[14] The previously mentioned HEMT structure and epitaxial graphene sample were used as examples to demonstrate the ability of this technique to determine the free charge carrier properties of 2DEGs situated on top of THz-transparent substrates. To accurately vary the external cavity (i.e. sample-magnet air gap), a stage containing a stepper motor and micrometer screw was constructed which provides a change in d_{gap} of only 1.6 μm. Variation of d_{gap} was used as an another measurement dimension, in addition to frequency and angle of incidence, to facilitate the extraction of 2DEG carrier properties. Results for N_s, μ, and m^* obtained using these more advanced cavity-tuning techniques are in excellent agreement with all other THz-OHE characterizations. [1]

The studies reported here provide crucial information necessary for future electronic device design. The experimentally determined room temperature effective mass in β-Ga_2O_3 and the HEMT structure may be used in subsequent

[1]Note, Chapters 2 through 7 are only first-authored publications or manuscripts. All other non-first-authored works are also included in the **List of own Publications** section (previously cited in dissertation:[83,119,86,115,154,45], and not previously cited in dissertation:[13,14,15,16,17,18,19,20,21,22]).

investigations to help identify their limiting factors. The *in-situ* gas exposure experiments for epitaxial graphene demonstrate its sensitivity to changes in humidity and gas composition, which must be considered during device fabrication. Additional OHE measurements could be performed on these materials as a function of temperature to determine the carrier scattering mechanisms which limit mobility. As more complex material systems are integrated into devices, it is important to continue exploring the OHE technique which is sensitive to all constituents in multilayered semiconductor structures. Emerging β-Ga_2O_3 epitaxal layer structures could be a candidate for characterization by MIR-OHE or THz-OHE, for example.

Bibliography

[1] M. Gonschorek, J.-F. Carlin, E. Feltin, M. Py, and N. Grandjean, Appl. Phys. Lett. **89**, 062106(2006).

[2] W. Choi, I. Lahiri, R. Seelaboyina, and Y. S. Kang, Crit. Rev. Solid State Mater. Sci. **35**, 52 (2010).

[3] S. Stepanov, V. Nikolaev, V. Bougrov, and A. Romanov, Rev. Adv. Mater. Sci **44**, 63(2016).

[4] M. Schubert, P. Kühne, V. Darakchieva, and T. Hofmann, J. Opt. Soc. Am. A **33**, 1553(2016).

[5] P. Kühne, C. M. Herzinger, M. Schubert, J. A. Woollam, and T. Hofmann, Rev. Sci. Instrum. **85**, 071301(2014).

[6] H. Fujiwara, *Spectroscopic Ellipsometry: Principles and Applications*, (John Wiley & Sons, 2007).

[7] R. M. Azzam and N. M. Bashara, *Ellipsometry and Polarized Light*, (North-Holland Publ. Co., Amsterdam, 1984).

[8] S. Knight, R. Korlacki, C. Dugan, J. C. Petrosky, A. Mock, P. A. Dowben, J. Matthew Mann, M. M. Kimani, and M. Schubert, J. Appl. Phys. **127**, 125103(2020).

[9] S. Knight, A. Mock, R. Korlacki, V. Darakchieva, B. Monemar, Y. Kumagai, K. Goto, M. Higashiwaki, and M. Schubert, Appl. Phys. Lett. **112**, 012103(2018).

[10] S. Knight, D. Prabhakaran, C. Binek, and M. Schubert, Sci. Rep. **9**, 1353(2019).

[11] S. Knight, S. Schöche, V. Darakchieva, P. Kühne, J.-F. Carlin, N. Grandjean, C. Herzinger, and M. Schubert, Opt. Lett. **40**, 2688(2015).

[12] S. Schöche, *Phonon and free-charge carrier properties in group-III nitride heterostructures investigated by spectroscopic ellipsometry and optical Hall effect*, PhD thesis, (2014).

[13] S. Knight, T. Hofmann, C. Bouhafs, N. Armakavicius, P. Kühne, V. Stanishev, I. G. Ivanov, R. Yakimova, S. Wimer, M. Schubert, *et al.*, Sci. Rep. **7**, 5151(2017).

[14] S. Knight *et al.*, Rev. Sci. Instrum. (In submission) **XXX**, XXX (2020).

[15] M. Lyons, R. Boyle, J. Davies, V. Hazel, and T. Rowland, Nucl. Eng. Des. **21**, 167 (1972).

[16] B. Frost, R. Inst. Chem., Rev. **2**, 163 (1969).

[17] J. W. Pang, W. J. Buyers, A. Chernatynskiy, M. D. Lumsden, B. C. Larson, and S. R. Phillpot, Phys. Rev. Lett. **110**, 157401 (2013).

[18] Q. Yin and S. Y. Savrasov, Phys. Rev. Lett. **100**, 225504 (2008).

[19] Y. Lu, Y. Yang, and P. Zhang, J. Phys. Condens. Matter **24**, 225801 (2012).

[20] M. Schubert, *Infrared Ellipsometry on semiconductor layer structures: Phonons, Plasmons, and Polaritons*, 209 (Springer Science & Business Media, 2004).

[21] J. Axe and G. Pettit, Phys. Rev. **151**, 676 (1966).

[22] Z. Chernia, Phys. Chem. Chem. Phys. **11**, 1729 (2009).

[23] J. Schoenes, Phys. Rep. **63**, 301 (1980).

[24] B. M. DeVetter, T. L. Myers, B. D. Cannon, N. K. Scharko, M. R. K. Kelly-Gorham, J. F. Corbey, A. L. Schemer-Kohrn, C. T. Resch, D. D. Reilly, and T. J. Johnson, J. Phys. Chem. A **122**, 7062 (2018).

[25] F. Gervais and B. Piriou, J. Phys. C: Solid State Phys. **7**, 2374 (1974).

[26] F. Gervais, Solid State Commun. **13**, 1211 (1973).

[27] F. Gervais and B. Piriou, Phys. Rev. B **10**, 1642 (1974).

[28] F. Gervais and B. Piriou, Phys. Rev. B **11**, 3944 (1975).

[29] P. Klemens, Phys. Rev. **148**, 845 (1966).

[30] P. Giannozzi, S. Baroni, N. Bonini, M. Calandra, R. Car, C. Cavazzoni, D. Ceresoli, G. L. Chiarotti, M. Cococcioni, I. Dabo, A. D. Corso, S. de Gironcoli, *et al.*, J. Phys.: Cond. Mat. **21**, 395502 (2009), quantum ESPRESSO is available from http://www.quantum-espresso.org. See also:.

[31] J. P. Perdew, K. Burke, and M. Ernzerhof, Phys. Rev. Lett. **77**, 3865(1996).

[32] A. D. Corso, Comput. Mater. Sci. **95**, 337 (2014), pSLibrary available from https://dalcorso.github.io/pslibrary/.

[33] H. J. Monkhorst and J. D. Pack, Phys. Rev. B **13**, 5188 (1976).

[34] S. Baroni, S. de Gironcoli, A. D. Corso, S. Baroni, S. de Gironcoli, and P. Giannozzi, Rev. Mod. Phys. **73**, 515 (2001).

[35] W. Setyawan and S. Curtarolo, Comput. Mat. Sci. **49**, 299(2010).

[36] M. Born, *Huang K Dynamical Theory of Crystal Lattices*, (Oxford: Clarendon Press, 1954).

[37] G. Venkataraman, L. A. Feldkamp, and V. C. Sahni, *Dynamics of Perfect Crystals*, (The MIT Press, 1975).

[38] X. Gonze and C. Lee, Phys. Rev. B **55**, 10355 (1997).

[39] A. Kokalj, Comp. Mater. Sci. **28**, 155 (2003), code available from http://www.xcrysden.org.

[40] M. Lazzeri and S. de Gironcoli, Phys. Rev. Lett. **81**, 2096(1998).

[41] N. Bonini, M. Lazzeri, N. Marzari, and F. Mauri, Phys. Rev. Lett. **99**, 176802(2007).

[42] L. Paulatto, F. Mauri, and M. Lazzeri, Phys. Rev. B **87**, 214303(2013).

[43] D. Vanderbilt, Phys. Rev. B **32**, 8412(1985).

[44] J. P. Perdew and A. Zunger, Phys. Rev. B **23**, 5048 (1981).

[45] A. Mock, C. Dugan, S. Knight, R. Korlacki, J. M. Mann, M. M. Kimani, J. C. Petrosky, P. A. Dowben, and M. Schubert, Appl. Phys. Lett. **114**, 211901 (2019).

[46] C. L. Dugan, G. G. Peterson, A. Mock, C. Young, J. M. Mann, M. Nastasi, M. Schubert, L. Wang, W.-N. Mei, I. Tanabe, *et al.*, Eur. Phys. J. B **91**, 67 (2018).

[47] A. Kasic, M. Schubert, S. Einfeldt, D. Hommel, and T. Tiwald, Phys. Rev. B **62**, 7365 (2000).

[48] M. Schubert, T. Tiwald, and C. Herzinger, Phys. Rev. B **61**, 8187 (2000).

[49] R. H. Lyddane, R. G. Sachs, and E. Teller, Phys. Rev. **59**, 673 (1941).

[50] G. Dolling, R. Cowley, and A. Woods, Can. J. Phys. **43**, 1397 (1965).

[51] A. S. Mikheykin, E. S. Zhukova, V. I. Torgashev, A. G. Razumnaya, Y. I. Yuzyuk, B. P. Gorshunov, A. S. Prokhorov, A. E. Sashin, A. A. Bush, and M. Dressel, Eur. Phys. J. B **87**, 232 (2014).

[52] P. Kumar, S. Saha, C. Serrao, A. Sood, and C. Rao, Pramana **74**, 281 (2010).

[53] T. Yamashita, N. Nitani, T. Tsuji, and H. Inagaki, J. Nucl. Mater. **245**, 72 (1997).

[54] P. Giura, L. Paulatto, F. He, R. P. Lobo, A. Bosak, E. Calandrini, L. Paolasini, and D. Antonangeli, Phys. Rev. B **99**, 220304 (2019).

[55] U. Betz, M. K. Olsson, J. Marthy, M. Escola, and F. Atamny, Surf. Coat. Technol. **200**, 5751 (2006).

[56] C. G. Granqvist, *Handbook of Inorganic Electrochromic Materials*, (Elsevier, 1995).

[57] D. Gogova, A. Iossifova, T. Ivanova, Z. Dimitrova, and K. Gesheva, J. Cryst. Growth **198/199**, 1230 (1999).

[58] F. Réti, M. Fleischer, H. Meixner, and J. Giber, Sens. Actuators, B Chem. **19**, 573 (1994).

[59] M. Higashiwaki, K. Sasaki, H. Murakami, Y. Kumagai, A. Koukitu, A. Kuramata, T. Masui, and S. Yamakoshi, Semicond. Sci. Technol. **31**, 034001(2016).

[60] J. F. Wager, Science **300**, 1245(2003).

[61] C. Sturm, R. Schmidt-Grund, C. Kranert, J. Furthmüller, F. Bechstedt, and M. Grundmann, Phys. Rev. B **94**, 035148(2016).

[62] C. Sturm, J. Furthmüller, F. Bechstedt, R. Schmidt-Grund, and M. Grundmann, APL Mater. **3**, 106106(2015).

[63] J. Furthmüller and F. Bechstedt, Phys. Rev. B **93**, 115204(2016).

[64] R. Roy, V. G. Hill, and E. F. Osborn, J. Am. Chem. Soc. **74**, 719(1952).

[65] H. H. Tippins, Phys. Rev. **140**, A316(1965).

[66] H. He, M. A. Blanco, and R. Pandey, Appl. Phys. Lett. **88**, 261904(2006).

[67] K. Yamaguchi, Solid State Commun. **131**, 739(2004).

[68] A. Mock, R. Korlacki, C. Briley, V. Darakchieva, B. Monemar, Y. Kumagai, K. Goto, M. Higashiwaki, and M. Schubert, arXiv preprint arXiv:1704.06711 (2017).

[69] J. B. Varley, J. R. Weber, A. Janotti, and C. G. Van de Walle, Appl. Phys. Lett. **97**, 142106(2010).

[70] H. Peelaers and C. G. V. de Walle, Phys. Status Solidi B **252**, 828 (2015).

[71] H. He, R. Orlando, M. A. Blanco, R. Pandey, E. Amzallag, I. Baraille, and M. Rérat, Phys. Rev. B **74**, 195123(2006).

[72] M.-G. Ju, X. Wang, W. Liang, Y. Zhao, and C. Li, J. Mater. Chem. A **2**, 17005(2014).

[73] N. Ueda, H. Hosono, R. Waseda, and H. Kawazoe, Appl. Phys. Lett. **71**, 933(1997).

[74] N. Suzuki, S. Ohira, M. Tanaka, T. Sugawara, K. Nakajima, and T. Shishido, Phys. Status Solidi C **4**, 2310(2007).

[75] K. Irmscher, Z. Galazka, M. Pietsch, R. Uecker, and R. Fornari, J. Appl. Phys. **110**, 063720(2011).

[76] E. G. Víllora, K. Shimamura, Y. Yoshikawa, T. Ujiie, and K. Aoki, Appl. Phys. Lett. **92**, 202120(2008).

[77] M. Schubert, T. Hofmann, and C. M. Herzinger, J. Opt. Soc. Am. A **20**, 347(2003).

[78] T. Hofmann, T. Chavdarov, V. Darakchieva, H. Lu, W. J. Schaff, and M. Schubert, Phys. Status Solidi C **3**, 1854(2006).

[79] T. Hofmann, V. Darakchieva, B. Monemar, H. Lu, W. Schaff, and M. Schubert, J. Electron. Mater. **37**, 611(2008).

[80] H. Aida, K. Nishiguchi, H. Takeda, N. Aota, K. Sunakawa, and Y. Yaguchi, Jpn. J. Appl. Phys. **47**, 8506(2008).

[81] K. Sasaki, A. Kuramata, T. Masui, E. G. Vìllora, K. Shimamura, and S. Yamakoshi, Appl. Phys. Express **5**, 035502(2012).

[82] K. Shimamura and E. Villora, Acta Phys. Pol., A **124**, 265(2013).

[83] M. Schubert, R. Korlacki, S. Knight, T. Hofmann, S. Schöche, V. Darakchieva, E. Janzén, B. Monemar, D. Gogova, Q.-T. Thieu, R. Togashi, H. Murakami, Y. Kumagai, K. Goto, A. Kuramata, S. Yamakoshi, and M. Higashiwaki, Phys. Rev. B **93**, 125209(2016).

[84] S. Geller, J. Chem. Phys **33**, 676(1960).

[85] M. Schubert, Phys. Rev. B **53**, 4265(1996).

[86] A. Mock, R. Korlacki, S. Knight, and M. Schubert, Phys. Rev. B **95**, 165202(2017).

[87] S. Schöche, P. Kühne, T. Hofmann, M. Schubert, D. Nilsson, A. Kakanakova-Georgieva, E. Janzen, and V. Darakchieva, Appl. Phys. Lett. **103**, 212107(2013).

[88] A. Parisini and R. Fornari, Semicond. Sci. Technol. **31**, 035023(2016).

[89] Y. Kang, K. Krishnaswamy, H. Peelaers, and C. G. Van de Walle, J. Phys.: Condens. Matter **29**, 234001(2017).

[90] E. G. Víllora, K. Shimamura, Y. Yoshikawa, K. Aoki, and N. Ichinose, J. Cryst. Growth **270**, 420(2004).

[91] C. Golz, *Ga_2O_3 conductivity anisotropy analysed by van-der-pauw measurements* (2017), 2nd International Workshop on Gallium Oxide and Related Materials.

[92] M. H. Wong, K. Sasaki, A. Kuramata, S. Yamakoshi, and M. Higashiwaki, Jpn. J. Appl. Phys. **55**, 1202B9(2016).

[93] J. E. Medvedeva, E. N. Teasley, and M. D. Hoffman, Phys. Rev. B **76**, 155107(2007).

[94] T. Perevalov, A. Shaposhnikov, K. Nasyrov, D. Gritsenko, V. Gritsenko, and V. Tapilin, *Defects in High-k Gate Dielectric Stacks. NATO Science Series II: Mathematics, Physics and Chemistry*, vol. 220, (Springer, Dordrecht, 2006).

[95] W. Eerenstein, N. D. Mathur, and J. F. Scott, Nature **442**, 759(2006).

[96] R. Ramesh and N. A. Spaldin, Nat. Mater. **6**, 21(2007).

[97] S.-W. Cheong and M. Mostovoy, Nat. Mater. **6**, 13(2007).

[98] T. Kimura, Y. Sekio, H. Nakamura, T. Siegrist, and A. Ramirez, Nat. Mater. **7**, 291(2008).

[99] V. N. Krivoruchko, Low Temperature Physics **38**, 807(2012).

[100] S. Neusser and D. Grundler, Adv. Mater. **21**, 2927(2009).

[101] M. P. Kostylev, A. A. Serga, T. Schneider, B. Leven, and B. Hillebrands, Appl. Phys. Lett. **87**, 153501(2005).

[102] P. Rovillain, R. De Sousa, Y. t. Gallais, A. Sacuto, M. A. Méasson, D. Colson, A. Forget, M. Bibes, A. Barthélémy, and M. Cazayous, Nat. Mater. **9**, 975(2010).

[103] A. Khitun, D. E. Nikonov, and K. L. Wang, J. Appl. Phys **106**, 123909(2009).

[104] A. Pimenov, A. Mukhin, V. Y. Ivanov, V. Travkin, A. Balbashov, and A. Loidl, Nat. Phys. **2**, 97(2006).

[105] A. Pimenov, T. Rudolf, F. Mayr, A. Loidl, A. Mukhin, and A. Balbashov, Phys. Rev. B **74**, 100403(2006).

[106] A. Sushkov, R. V. Aguilar, S. Park, S. Cheong, and H. Drew, Phys. Rev. Lett. **98**, 027202(2007).

[107] N. Kida, Y. Takahashi, J. Lee, R. Shimano, Y. Yamasaki, Y. Kaneko, S. Miyahara, N. Furukawa, T. Arima, and Y. Tokura, J. Opt. Soc. Am. B **26**, A35(2009).

[108] T. N. Stanislavchuk, Y. Wang, S. W. Cheong, and A. A. Sirenko, Phys. Rev. B **95**, 054427(2017).

[109] S. P. P. Jones, S. M. Gaw, K. I. Doig, D. Prabhakaran, E. M. H. Wheeler, A. T. Boothroyd, and J. Lloyd-Hughes, Nat. Commun. **5**, 3787(2014).

[110] J. F. Scott, NPG Asia Mater. **5**, e72(2013).

[111] C. D. W. Mosley, M. Failla, D. Prabhakaran, and J. Lloyd-Hughes, Sci. Rep. **7**, 12337(2017).

[112] S. P. P. Jones, N. C. Wurz, M. Failla, D. Prabhakaran, C. F. McConville, and J. Lloyd-Hughes, Phys. Rev. B **90**, 064405(2014).

[113] C. D. W. Mosley, D. Prabhakaran, and J. Lloyd-Hughes, J. Phys. D (2018).

[114] T. Hofmann, D. Schmidt, A. Boosalis, P. Kühne, C. M. Herzinger, J. A. Woollam, E. Schubert, and M. Schubert, MRS Online Proc. Libr. Arch. **1409**(2012).

[115] T. Hofmann, S. Knight, D. Sekora, D. Schmidt, C. M. Herzinger, J. A. Woollam, E. Schubert, and M. Schubert, Appl. Surf. Sci. **421**, 513(2017).

[116] T. Hofmann, D. Schmidt, and M. Schubert, in *Ellipsometry at the Nanoscale* (Springer, Berlin, Heidelberg, 2013), pp. 411–428.

[117] P. Kühne, N. Armakavicius, V. Stanishev, C. M. Herzinger, M. Schubert, and V. Darakchieva, IEEE Trans. Terahertz Sci. Technol. **8**, 257(2018).

[118] T. Hofmann, P. Kühne, S. Schöche, J.-T. Chen, U. Forsberg, E. Janzén, N. B. Sedrine, C. M. Herzinger, J. A. Woollam, M. Schubert, and V. Darakchieva, Appl. Phys. Lett. **101**, 192102(2012).

[119] N. Armakavicius, J.-T. Chen, T. Hofmann, S. Knight, P. Kühne, D. Nilsson, U. Forsberg, E. Janzén, and V. Darakchieva, Phys. Status Solidi C **13**, 369(2016).

[120] T. N. Stanislavchuk, T. D. Kang, P. D. Rogers, E. C. Standard, R. Basistyy, A. M. Kotelyanskii, G. Nita, T. Zhou, G. L. Carr, M. Kotelyanskii, *et al.*, Rev. of Sci. Instrum. **84**, 023901(2013).

[121] C. Traum, P. Inácio, C. Felix, P. Segonds, A. Pena, J. Debray, B. Boulanger, Y. Petit, D. Rytz, G. Montemezzani, *et al.*, Opt. Mater. Express **4**, 57(2014).

[122] W. Lang and R. Claus, Phys. Rev. B **26**, 7119(1982).

[123] P. D. Rogers, T. D. Kang, T. Zhou, M. Kotelyanskii, and A. A. Sirenko, Thin Solid Films **519**, 2668(2011).

[124] D. Prabhakaran and A. T. Boothroyd, J. Cryst. Growth **250**, 77(2003).

[125] A. Rebello, Z. C. M. Winter, S. Viall, and J. J. Neumeier, Phys. Rev. B **88**, 094420(2013).

[126] M. Schubert, T. Hofmann, and C. M. Herzinger, J. Opt. Soc. Am. A **20**, 347(2003).

[127] P. Kühne, V. Darakchieva, R. Yakimova, J. D. Tedesco, R. L. Myers-Ward, C. R. Eddy, D. K. Gaskill, C. M. Herzinger, J. A. Woollam, M. Schubert, and T. Hofmann, Phys. Rev. Lett. **111**, 077402(2013).

[128] T. Hofmann, C. M. Herzinger, J. L. Tedesco, D. K. Gaskill, J. A. Woollam, and M. Schubert, Thin Solid Films **519**, 2593(2011).

[129] T. Hofmann, A. Boosalis, P. Kühne, C. M. Herzinger, J. A. Woollam, D. K. Gaskill, J. L. Tedesco, and M. Schubert, Appl. Phys. Lett. **98**, 041906(2011).

[130] S. Schöche, J. Shi, A. Boosalis, P. Kühne, C. M. Herzinger, J. A. Woollam, W. J. Schaff, L. F. Eastman, M. Schubert, and T. Hofmann, Appl. Phys. Lett. **98**, 092103(2011).

[131] T. Hofmann, C. Herzinger, and M. Schubert, phys. stat. sol. (a) **205**, 779 (2008).

[132] T. Hofmann, U. Schade, C. M. Herzinger, P. Esquinazi, and M. Schubert, Rev. Sci. Instrum. **77**, 063902(2006).

[133] M. Onoda, S. Murakami, and N. Nagaosa, Physical review letters **93**, 083901 (2004).

[134] P. Wang, W. Li, Q. Liu, and X. Jiang, Physical Review A **90**, 015801 (2014).

[135] Y. Ino, R. Shimano, Y. Svirko, and M. Kuwata-Gonokami, Physical Review B **70**, 155101 (2004).

[136] M. Schubert, *Infrared Ellipsometry on semiconductor layer structures: Phonons, plasmons and polaritons*, vol. 209 of *Springer Tracts in Modern Physics*, (Springer, Berlin, 2004).

[137] V. Darakchieva, M. Beckers, M.-Y. Xie, L. Hultman, B. Monemar, J.-F. Carlin, E. Feltin, M. Gonschorek, and N. Grandjean, J. Appl. Phys. **103**, 103513(2008).

[138] T. Hofmann, C. Herzinger, A. Boosalis, T. Tiwald, J. Woollam, and M. Schubert, Rev. Sci. Instrum. **81**, 023101 (2010).

[139] P. Yu and M. Cardona, *Fundamentals of Semiconductors*, (Springer, Berlin, 1999).

[140] C. Pidgeon, in *Handbook on Semiconductors*, edited by M. Balkanski (North-Holland, Amsterdam, 1980).

[141] L. S. Abdallah, S. Zollner, C. Lavoie, A. Ozcan, and M. Raymond, Thin Solid Films **571**, 484 (2014).

[142] S. Roberts, Physical Review **114**, 104 (1959).

[143] I. Vurgaftman, J. R. Meyer, and L. R. Ram-Mohan, J. Appl. Phys. **89**, 5815 (2001).

[144] H. Oughaddou, H. Enriquez, M. R. Tchalala, H. Yildirim, A. J. Mayne, A. Bendounan, G. Dujardin, M. A. Ali, and A. Kara, Prog. Surf. Sci. **90**, 46 (2015).

[145] X. Li and H. Zhu, J. Materiomics **1**, 33 (2015).

[146] J. Bao, K. Jeppson, M. Edwards, Y. Fu, L. Ye, X. Lu, and J. Liu, Electron. Mater. Lett. **12**, 1 (2016).

[147] A. N. Sidorov, K. Gaskill, M. B. Nardelli, J. L. Tedesco, R. L. Myers-Ward, C. R. E. Jr., T. Jayasekera, K. W. Kim, R. Jayasingha, A. Sherehiy, R. Stallard, and G. U. Sumanasekera, J. Appl. Phys. **111**, 113706 (2012).

[148] C. E. Giusca, V. Panchal, M. Munz, V. D. Wheeler, L. O. Nyakiti, R. L. Myers-Ward, D. K. Gaskill, and O. Kazakova, Adv. Mater. Interf. **2**, 1500252 (2015).

[149] M. W. Nomani, R. Shishir, M. Qazi, D. Diwan, V. Shields, M. Spencer, G. S. Tompa, N. M. Sbrockey, and G. Koley, Sens. Actuators B Chem. **150**, 301 (2010).

[150] Y. Yang and R. Murali, Appl. Phys. Lett. **98**, 093116 (2011).

[151] J. Chan, A. Venugopal, A. Pirkle, S. McDonnell, D. Hinojos, C. W. Magnuson, R. S. Ruoff, L. Colombo, R. M. Wallace, and E. M. Vogel, ACS Nano **6**, 3224 (2012).

[152] C. J. Docherty, C.-T. Lin, H. J. Joyce, R. J. Nicholas, L. M. Herz, L.-J. Li, and M. B. Johnston, Nat. Commun. **3**, 1228(2012).

[153] H. Pinto and A. Markevich, Beilstein J. Nanotechnol. **5**, 1842 (2014).

[154] N. Armakavicius, C. Bouhafs, V. Stanishev, P. Kühne, R. Yakimova, S. Knight, T. Hofmann, M. Schubert, and V. Darakchieva, Appl. Surf. Sci. **421**, 357(2017).

[155] R. Yakimova, T. Iakimov, G. Yazdi, C. Bouhafs, J. Eriksson, A. Zakharov, A. Boosalis, M. Schubert, and V. Darakchieva, Physica B **439**, 54 (2014).

[156] C. Riedl, C. Coletti, and U. Starke, J. Phys. D: Appl. Phys. **43**, 374009 (2010).

[157] O. Kazakova, V. Panchal, and T. L. Burnett, Crystals **3**, 191 (2013).

[158] R. Pearce, T. Iakimov, M. Andersson, L. Hultman, A. L. Spetz, and R. Yakimova, Sens. Actuators B Chem. **155**, 451 (2011).

[159] L. Kong, A. Enders, T. S. Rahman, and P. A. Dowben, J. Phys. Condens. Matter **26**, 443001 (2014).

[160] J. L. Tedesco, B. L. VanMil, R. L. Myers-Ward, J. M. McCrate, S. A. Kitt, P. M. Campbell, G. G. Jernigan, J. C. Culbertson, C. R. Eddy Jr, and D. K. Gaskill, Appl. Phys. Lett. **95**, 122102 (2009).

[161] V. Chakrapani, J. C. Angus, A. B. Anderson, S. D. Wolter, B. R. Stoner, and G. U. Sumanasekera, Science **318**, 1424 (2007).

[162] S. Adam, E. Hwang, V. Galitski, and S. D. Sarma, Proc. Natl. Acad. Sci. USA **104**, 18392 (2007).

[163] W. Zhu, V. Perebeinos, M. Freitag, and P. Avouris, Phys. Rev. B **80**, 235402 (2009).

[164] E. Hwang, S. Adam, and S. D. Sarma, Phys. Rev. Lett. **98**, 186806 (2007).

[165] S. Tanabe, Y. Sekine, H. Kageshima, M. Nagase, and H. Hibino, Phys. Rev. B **84**, 115458 (2011).

[166] J.-H. Chen, C. Jang, S. Adam, M. Fuhrer, E. Williams, and M. Ishigami, Nature Phys. **4**, 377 (2008).

[167] M. Hofmann, Y.-P. Hsieh, K.-W. Chang, H.-G. Tsai, and T.-T. Chen, Sci. Rep. **5**(2015).

[168] E. Hwang, S. Adam, and S. D. Sarma, Phys. Rev. B **76**, 195421 (2007).

[169] J. D. Buron, F. Pizzocchero, P. U. Jepsen, D. H. Petersen, J. M. Caridad, B. S. Jessen, T. J. Booth, and P. Bøggild, Sci. Rep. **5**, 12305(2015).

[170] T. Ando, J. Phys. Soc. Jpn. **75**, 074716 (2006).

[171] Y. Yang, K. Brenner, and R. Murali, Carbon **50**, 1727 (2012).

[172] E. Hwang and S. D. Sarma, Phys. Rev. B **77**, 115449 (2008).

[173] T. Yager, A. Lartsev, R. Yakimova, S. Lara-Avila, and S. Kubatkin, Carbon **87**, 409 (2015).

[174] C. Bouhafs, *Structural and Electronic Properties of Graphene on 4H- and 3C-SiC*, PhD thesis, Linköping University Electronic Press (2016).

[175] I. G. Ivanov, J. U. Hassan, T. Iakimov, A. A. Zakharov, R. Yakimova, and E. Janzén, Carbon **77**, 492 (2014).

[176] W. H. Press, *Numerical Recipes 3rd Edition: The Art of Scientific Computing*, (Cambridge university press, 2007).

[177] H. J. Liebe, G. A. Hufford, and T. Manabe, Int. J. Infrared Milli. **12**, 659 (1991).

[178] K. S. Novoselov, A. K. Geim, S. V. Morozov, D. Jiang, M. I. Katsnelson, I. V. Grigorieva, S. V. Dubonos, and A. A. Firsov, Nature **438**, 197(2005).

[179] T. Hofmann, C. M. Herzinger, C. Krahmer, K. Streubel, and M. Schubert, phys. stat. sol. (a) **205**, 779(2008).

[180] P. Drude, Ann. Phys. **319**, 677(1904).

[181] P. Drude, Ann. Phys. **306**, 566(1900).

[182] P. Drude, Ann. Phys. **282**, 353(1892).

[183] C. Bouhafs, V. Stanishev, A. A. Zakharov, T. Hofmann, P. Kühne, T. Iakimov, R. Yakimova, M. Schubert, and V. Darakchieva, Appl. Phys. Lett. **109**, 203102(2016).

[184] C. Bouhafs, A. Zakharov, I. G. Ivanov, F. Giannazzo, J. Eriksson, V. Stanishev, P. Kühne, T. Iakimov, T. Hofmann, M. Schubert, *et al.*, Carbon **116**, 722(2017).

[185] R. Azzam and N. Bashara, J. Opt. Soc. Am. **62**, 1521(1972).

[186] M. Schubert, B. Rheinländer, J. A. Woollam, B. Johs, and C. M. Herzinger, J. Opt. Soc. Am. A **13**, 875(1996).

[187] K. Järrendahl and B. Kahr, J. A. Woollam Co. Inc. Annual Newsletter **2011**, 8(2011).

[188] R. C. Jones, J. Opt. Soc. Am. **37**, 107(1947).

[189] , Note that for isotropic samples, or samples which do not cause conversion of polarization from parallel (p) to perpendicular (s) to the plane of incidence and vice versa, the off-block-diagonal elements of the Mueller matrix (M_{13}, M_{23}, M_{31}, M_{32}, M_{14}, M_{24}, M_{41}, M_{42}) are zero throughout. The optical Hall effect causes anisotropy and the off-block-diagonal elements differ from zero in strong external magnetic fields. Hence, these element are often of particular interest for displaying changes in the sample's optical

properties upon the occurrence of the optical Hall effect. Any changes in these elements with the application of an external magnetic field are then directly related to the existence, and to the properties of free charge carriers within the layer stack of a given multiple layer sample. See also Refs.[5,4] .

[190] M. Schubert, T. E. Tiwald, and C. M. Herzinger, Phys. Rev. B **61**, 8187(2000).

[191] A. Kasic, M. Schubert, J. Off, B. Kuhn, F. Scholz, S. Einfeldt, T. Bottcher, D. Hommel, D. As, U. Kohler, A. Dadgar, A. Krost, *et al.*, Phys. Status Solidi C **0**, 1750(2003).

[192] Y.-C. Tsai and C. Bayram, Sci. Rep. **9**, 1(2019).

[193] M. Gonschorek, J.-F. Carlin, E. Feltin, M. Py, N. Grandjean, V. Darakchieva, B. Monemar, M. Lorenz, and G. Ramm, J. Appl. Phys. **103**, 093714(2008).

[194] K. S. Novoselov, A. K. Geim, S. V. Morozov, D. Jiang, M. I. Katsnelson, I. V. Grigorieva, S. V. Dubonos, and A. A. Firsov, Nature **438**, 197(2005).

[195] Http://creativecommons.org/licenses/by/4.0/.

List of Abbreviations

HEMT	High-electron-mobility transistor
2DEG	Two-dimensional electron gas
OHE	Optical Hall effect
FIR	Far-infrared
MIR	Mid-infrared
DFT	Density function theory
THz	Terahertz
TO	Transverse optic
LO	Longitudinal optic
IRSE	Infrared spectroscopic ellipsometry
FPSQ	Four-parameter semi-quantum
GGA	Generalized gradient approximation
PBE	Perdew, Burke, and Ernzerhof
HSCV	Hamann-Schlüter-Chiang-Vanderbilt
PZ	Perdew-Zunger
LPP	Longitudinal phonon plasmon
THz-TDS	Terahertz time-domain spectroscopy
AF	Antiferromagnetic
BWO	Backwards wave oscillator
SKPM	Scanning Kelvin Probe Microscopy

ML Monolayer

BL Bilayer

RH Relative humidity

STP Sample tip-tilt plate

SA Sample

SM Stepper motor

MHP Mirror housing plate

AS Adjustment screw

PM Permanent magnet

List of Symbols

ρ	Change in the polarization of light
r_{p}	Fresnel reflection coefficient for *p*-polarized light
r_{s}	Fresnel reflection coefficient for *s*-polarized light
$\boldsymbol{E}$	Electrical field vector
$\boldsymbol{k}$	Electromagnetic wavevector
Ψ	Polarization rotation of light
Δ	Relative phase shift between *p*- and *s*-light components
Φ_{a}	Angle of incidence
$\mathbf{x}$, $\mathbf{y}$, $\mathbf{z}$	Cartesian coordinate axes
ϵ	Dielectric function
ϵ_{ij}	Element of dielectric tensor in row i and column j
ϵ_{o}	Vacuum permittivity
ϵ_{∞}	High-frequency dielectric constant
ϵ_{DC}	Low-frequency (static) dielectric constant
ω	Angular frequency
$\mathrm{Re}\{\mathrm{X}\}$	Real part of X
$\mathrm{Im}\{\mathrm{X}\}$	Imaginary part of X
X	Scalar-valued quantity X
$\mathbf{X}$	Vector or tensor $\mathbf{X}$

ω_{TO}	Transverse optic phonon resonant frequency
ω_{LO}	Longitudinal optic phonon resonant frequency
γ_{TO}	Transverse optic phonon broadening parameter
γ_{LO}	Longitudinal optic phonon broadening parameter
$\mathbf{D}$	Displacement field vector
g_j	the j^{th} Grüneisen parameter
α_{L}	Linear expansion coefficient
α_{V}	Volume expansion coefficient
$\hbar$	Reduced Planck constant
h	Planck constant
k_{B}	Boltzmann constant
$\mathbf{a}$, $\mathbf{b}$, $\mathbf{c}$	Crystal unit cell coordinate axes
m_{o}	free electron mass
$\boldsymbol{\omega_{\mathrm{p}}}$	Scteened plasma frequency tensor
$\boldsymbol{B}$	Magnetic field vector
$\boldsymbol{m^{\star}}$	Effective mass tensor
$\boldsymbol{\mu}$	Mobility tensor
N	Free charge carrier volume density
N_{s}	Free charge carrier sheet density
q	Elementary electric charge
$\boldsymbol{I}$	Identity matrix
M_{ij}	Mueller matrix element in row i and column j
ΔM_{ij}	Difference data Mueller matrix element in row i and column j
ϕ	Azimuth angle orientation

α	Optical absorption coefficient
$\tilde{n}$	Complex-valued index of refraction
λ	Wavelength
c	Speed of light
v_{f}	Fermi velocity
d_{gap}	External Fabry-Pérot cavity thickness
d_{sub}	Substrate thickness

List of own Publications

[1] S. Knight, R. Korlacki, C. Dugan, J. C. Petrosky, A. Mock, P. A. Dowben, J. Matthew Mann, M. M. Kimani, and M. Schubert, J. Appl. Phys. **127**, 125103(2020).

[2] S. Knight, A. Mock, R. Korlacki, V. Darakchieva, B. Monemar, Y. Kumagai, K. Goto, M. Higashiwaki, and M. Schubert, Appl. Phys. Lett. **112**, 012103(2018).

[3] S. Knight, D. Prabhakaran, C. Binek, and M. Schubert, Sci. Rep. **9**, 1353(2019).

[4] S. Knight, S. Schöche, V. Darakchieva, P. Kühne, J.-F. Carlin, N. Grandjean, C. Herzinger, and M. Schubert, Opt. Lett. **40**, 2688(2015).

[5] S. Knight, T. Hofmann, C. Bouhafs, N. Armakavicius, P. Kühne, V. Stanishev, I. G. Ivanov, R. Yakimova, S. Wimer, M. Schubert, *et al.*, Sci. Rep. **7**, 5151(2017).

[6] S. Knight *et al.*, Rev. Sci. Instrum. (In submission) **XXX**, XXX (2020).

[7] M. Schubert, R. Korlacki, S. Knight, T. Hofmann, S. Schöche, V. Darakchieva, E. Janzén, B. Monemar, D. Gogova, Q.-T. Thieu, R. Togashi, H. Murakami, Y. Kumagai, K. Goto, A. Kuramata, S. Yamakoshi, and M. Higashiwaki, Phys. Rev. B **93**, 125209(2016).

[8] N. Armakavicius, J.-T. Chen, T. Hofmann, S. Knight, P. Kühne, D. Nilsson, U. Forsberg, E. Janzén, and V. Darakchieva, Phys. Status Solidi C **13**, 369(2016).

[9] A. Mock, R. Korlacki, S. Knight, and M. Schubert, Phys. Rev. B **95**, 165202(2017).

[10] T. Hofmann, S. Knight, D. Sekora, D. Schmidt, C. M. Herzinger, J. A. Woollam, E. Schubert, and M. Schubert, Appl. Surf. Sci. **421**, 513(2017).

[11] N. Armakavicius, C. Bouhafs, V. Stanishev, P. Kühne, R. Yakimova, S. Knight, T. Hofmann, M. Schubert, and V. Darakchieva, Appl. Surf. Sci. **421**, 357(2017).

[12] A. Mock, C. Dugan, S. Knight, R. Korlacki, J. M. Mann, M. M. Kimani, J. C. Petrosky, P. A. Dowben, and M. Schubert, Appl. Phys. Lett. **114**, 211901 (2019).

[13] E. Echeverria, B. Dong, G. Peterson, J. P. Silva, E. R. Wilson, M. S. Driver, Y.-S. Jun, G. D. Stucky, S. Knight, T. Hofmann, *et al.*, Journal of Physics D: Applied Physics **49**, 355302 (2016).

[14] A. Oyelade, A. J. Yost, N. Benker, B. Dong, S. Knight, M. Schubert, P. A. Dowben, and J. A. Kelber, Langmuir **34**, 12007 (2018).

[15] A. Mock, R. Korlacki, S. Knight, and M. Schubert, Physical Review B **97**, 165203 (2018).

[16] N. Armakavicius, V. Stanishev, S. Knight, P. Kühne, M. Schubert, and V. Darakchieva, Applied Physics Letters **112**, 082103 (2018).

[17] M. Schubert, A. Mock, R. Korlacki, S. Knight, Z. Galazka, G. Wagner, V. Wheeler, M. Tadjer, K. Goto, and V. Darakchieva, Applied Physics Letters **114**, 102102 (2019).

[18] A. Mock, R. Korlacki, S. Knight, M. Stokey, A. Fritz, V. Darakchieva, and M. Schubert, Physical Review B **99**, 184302 (2019).

[19] M. Hilfiker, U. Kilic, A. Mock, V. Darakchieva, S. Knight, R. Korlacki, A. Mauze, Y. Zhang, J. Speck, and M. Schubert, Applied Physics Letters **114**, 231901 (2019).

[20] M. Stokey, A. Mock, R. Korlacki, S. Knight, V. Darakchieva, S. Schöche, and M. Schubert, Journal of Applied Physics **127**, 115702 (2020).

[21] M. Stokey, R. Korlacki, S. Knight, Z. Galazka, K. Irmscher, V. Darakchieva, and M. Schubert, Appl. Phys. Lett. (In submission) **XX**, XXX (2020).

[22] M. Schubert, P. Kühne, V. Darakchieva, S. Schöche, S. Knight, and C. M. Herzinger, J. Opt. Soc. Am. A (In submission) **XX**, XXX (2020).